UTSTUNOMIYA UNIVERSITY

In-system optimization of computer-generated hologram for femtosecond laser processing with high-throughput and high-stability

by

Honghao Zhang

A thesis submitted in partial fulfillment

for the degree of Doctor of Philosophy

in the

Center for Optical Research and Education

Mar 2022

Contents

Chapter 1: Introduction

1.1 Background

Historical review

Holographic femtosecond laser processing is a method that a computer-generated hologram (CGH) displayed on a spatial light modulator (SLM), can be used for parallel laser processing with high throughput and high light-use efficiency [1]. Use of an SLM offers reconfigurability of beam shaping, which enables arbitrary, and variable novel laser processing schemes. In order to improve the throughput of laser processing, the holographic method has been applied to shaped-beam processing using arbitrary beam profiles [2,3] and to the fabrication of three-dimensional (3D) structures inside transparent materials using parallel laser beams [4-8]. This technology, based on high precision modulation of spatial light, is a cutting-edge laser manufacturing technology gradually developed under the historical background of laser processing. So, in this section, the development history of holographic femtosecond laser processing will be mentioned briefly as below.

Laser, successfully developed by T. H. Maiman in 1960s, is one of the major inventions of the 20th century and has great technological development potential. Laser have the characteristics of excellent beam quality, superior reliability, and high efficiency, high brightness, good monochromatism and high energy density. Based on this, laser processing technology arises at the historical moment. Laser processing is the technique that uses a beam of laser-generated by the thermal effect to complete the processing such as laser welding, surface modification, laser cutting, laser marking, laser drilling, and micro-processing, and it is widely used in the fields of electronics & semiconductor industry, medical industry, telecommunications, automotive, architecture, machine tools, aerospace, defense, and others, has become an indispensable part of the advanced manufacturing

technology. Compared with the conventional processing means, such as machine tools, plasma technology, flame, and water jet, the advantages of laser processing are that it has good time and space control, small deformation of the workpiece surface, fast processing speed, and many types of materials can be processed, which is very suitable for automatic processing. Therefore, laser processing makes a high precision, high efficiency and low cost of processing technology become possible.

From the perspective of the size of the global laser processing market, according to the latest Optech Consulting survey report, as shown in fig. 1.1, the global market for laser materials processing accounted for USD 17.4 billion in 2020 [9]. Although it decreased by 20% from the peak in 2018, which was due to the adjustment of the laser processing industry started from the second half of 2018 and the impact of COVID-19, but as the recovery of the world economy, it is expected to grow by 12% in 2021 compared with 2020. In addition, from the perspective of the global Laser application market structure, according to the statistical data released in 2020 by Laser Focus World, an authoritative publication of the international Laser industry, Laser processing accounts for more than 40.6 percent, becoming the most important application market, as shown in fig. 1.2 [10]. Except for communications and optical storage, which accounted for 27.3 percent, and scientific research and military applications, which accounted for 12 percent, all the other fields accounted for less than 10 percent. It represents the laser processing industry, in the world, showing a rapid rise in the development trend, and will attract more attention from the world.

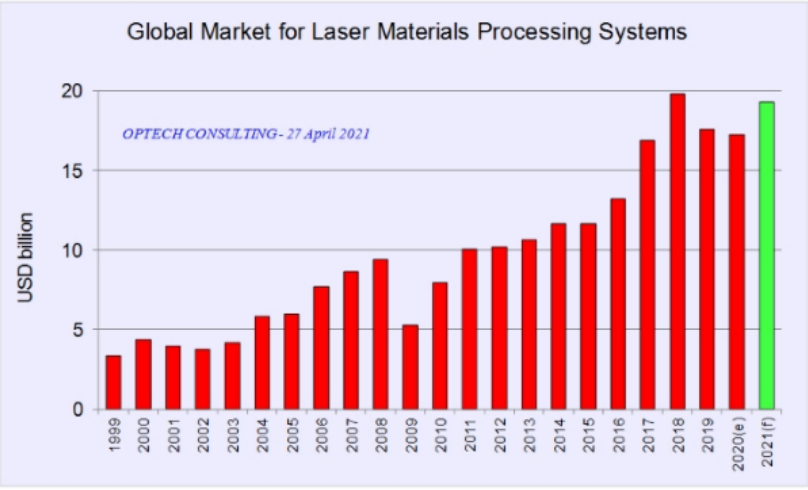

Figure 1.1 Global market for laser materials processing systems.

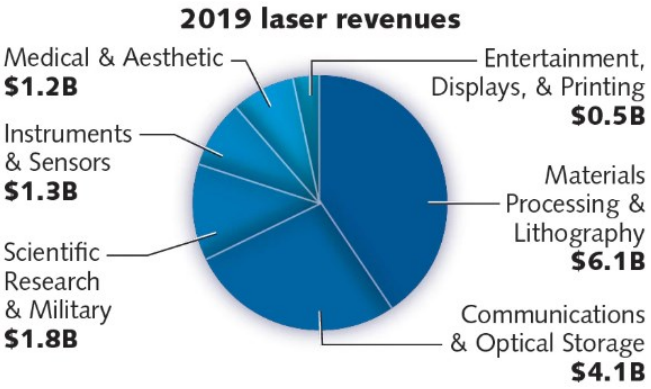

Figure 1.2. Global market for laser materials processing systems.

However, with the advancement of laser processing industrialization, as well as the increasing dependence and demand of all walks of life on laser processing technology, high precision, high utilization, high throughput laser processing has been put on the agenda.

In order to achieve these goals, the laser source used for laser processing has been developed from the ruby laser at the beginning (1960), after the development of nanosecond laser (1961) and picosecond laser (1966), to the femtosecond laser (1991). The development of laser source is manifested in the improvement of spatial resolution, the shortening of pulse duration and the improvement of power density [11].

Femtosecond laser processing is an effective tool to achieve high precision modification on the surface and inside structures, which depends on its high-power density, ultra-short pulse duration and no thermal effects contrast to the others [12].

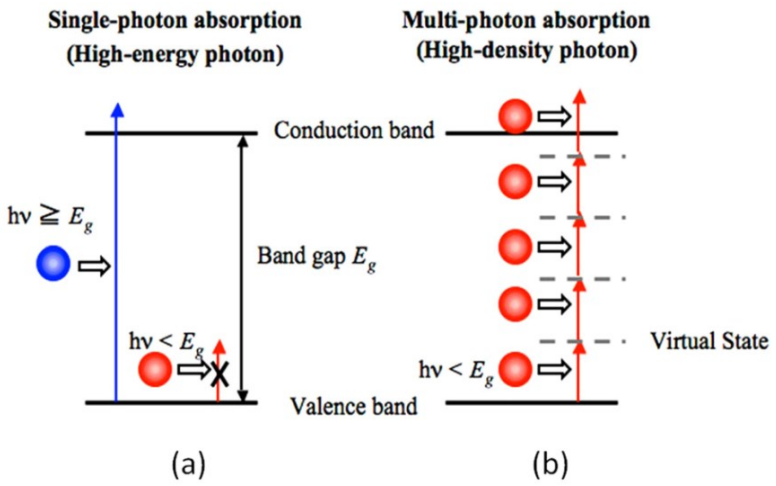

Figure 1.3. High photon density can be easily obtained using fs laser due to the ultrashort pulse width.

As a laser source, femtosecond laser emits ultra-short pulse duration well below 1 picosecond in the domain of femtoseconds (1 fs = 10^{-15} s). Due to the properties of high-peak power, for example, as a Ti: sapphire laser can provide the pulse peak power greater than 5 MW [13], and high pulse repetition rates in the megahertz or gigahertz, tightly focused femtosecond laser pulse can deposit enough energy in the localized focal area of the processing materials to cause permanent structural changes and property changes.

From the point of view of microscopic particles, as shown in fig. 1.3, the material that cannot absorb a linear single-photon process, can be easily modified by a femtosecond laser pulse, which is based on a nonlinear multi-photon absorption process. Compared with longer pulses, femtosecond lasers can transfer a large amount of energy to electrons through the multi-photon absorption and avalanche ionization in an ultra-short timescale, much less time than it takes for coupling to the surrounding lattice to occur [14,15].

Therefore, femtosecond laser processing, also known as "cold processing", allows energy deposition to be formed only in a localized focal area of the material, with no damage in the surrounding structure, which is why it can achieve high-precision and high-resolution processing.

Due to the high resolution of femtosecond laser processing, the microstructure of λ/10~λ/2 can be obtained during the processing of materials. Therefore, a large numbers of pulse irradiation points are needed in the actual two-dimensional and three-dimensional processing of millimeter to centimeter scales. For example, in a 1 cm^3 of material, if one processing point needs to be processed every 1μm, the total number of points to be processed is 10^{12}. Even with the use of a 1GHz repetition rate laser, the laser processing still takes about 16.67 minutes.

In order to meet the needs of high-throughput laser processing, reduce production costs and improve technical competitiveness, it is necessary to improve the throughput of femtosecond laser processing.

Holographic laser processing

In recent years, a number of laser processing methods have been proposed to improve throughput, they are the high-speed mechanical motion laser processing method and a multi-beam shaping optical assembly method, as shown in fig. 1.4. The former is achieved by scanners or a high-speed moving platform, often called scanning laser processing [16], which can achieve large area pattern processing, but requires a laser source with a high repetition rate, high-speed optical switching devices and high-speed scanning devices. The latter is achieved through specific optical components, such as optical mask [17-20], beam splitters [21-24], lens arrays [25,26], diffractive optical elements (DOE) [27-30], and liquid crystal on silicon spatial light modulator (LCOS-SLM) [31,32]. This parallel laser processing method based on SLM to modulate spatial light is our main research topic, namely holographic femtosecond laser processing.

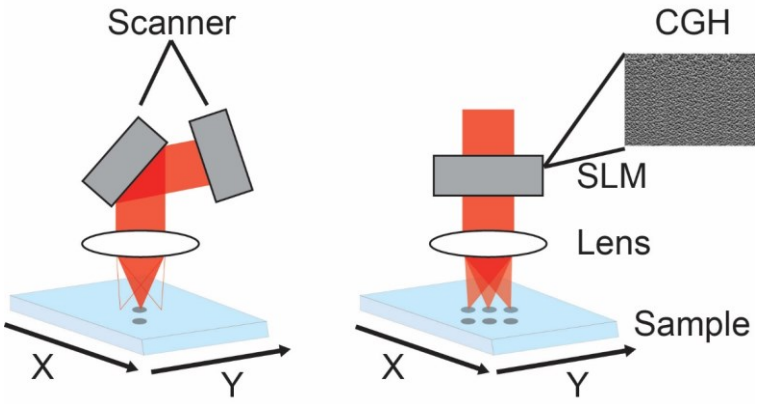

Figure 1.4. Concept of scanning (left) and holographic (right) laser processing.

Since the principle of spatial light modulation is based on CGH, it can realize high throughput processing without the need of mechanical moving equipment. For other parallel processing methods, high precision scanning equipment and other complex optical modulation components are required. In addition, for example, optical mask will lead to some loss of light energy, and the beam splitter will lead to the increase of the cost of the component and the decline of system stability. Furthermore, the uniformity of parallel beam cannot be adjusted for lens arrays.

Features of holographic laser processing

There are many features and advantages of the holographic femtosecond laser processing, such as the improvement on the throughput, the light use efficiency, and the ability for variable patterning processing.

First, its mechanism of spatial light modulation determines that it can effectively improve the throughput of laser processing. After the beam is shaped and split by SLM, the throughput will be calculated according to the number of points designed under the same processing pattern. For example, after splitting a beam of incident light into 10 beams, then in the same time, the throughput of the latter will be 10 times than that of the former. In addition, when the processing pattern CGH is constantly updated and changed, the throughput can be calculated according to the response time characteristics of the SLM. Usually, it only takes tens of milliseconds to update once, which greatly reduces the processing delay gap, which is guaranteed the maximum increase in processing throughput per unit time.

On the other hand, the utilization of femtosecond laser energy is also a crucial consideration in the laser processing industry. The parallel processing method of holographic femtosecond laser processing can effectively improve the utilization efficiency of laser energy, and more fully convert laser energy into material modification effects.
For example, the typical pulse energy of femtosecond laser processing is about 10 μJ to 10 mJ, and the pulse energy required for glass ablation is 10 nJ to 10 μJ. When the material is irradiated with a 1 kHz pulse, the pulse energy consumed is 100 nJ of the original energy 1 mJ, and a very low energy use efficiency of 0.01% is obtained. If 1000 parallel pulses are applied, the energy use efficiency can be increased to 10%, which is 1000 times that of the former. Therefore, within the pulse energy range, and considering the corresponding laser repetition frequency, designing a reasonable number of parallel processing points can achieve a variable ratio of energy efficiency improvement.

Another feature of holographic femtosecond laser processing is its variable pattern processing capability. This technology can meet the laser processing needs of different customers by designing different holographic patterns, including the variability of the number of pattern points, 2D and 3D patterns, cooperating with SLM to achieve high-speed

update of the pattern, and cooperating with scanning equipment to achieve large-scale pattern changes. As shown in the fig. 1.5, 3D patterns processed at different plane inside glass, four spots in rectangle shape and three spots in triangle shape, we can obtain the uniform micro-holes as the uniformity of the 7 spots optimized from 1st to 30th iteration.

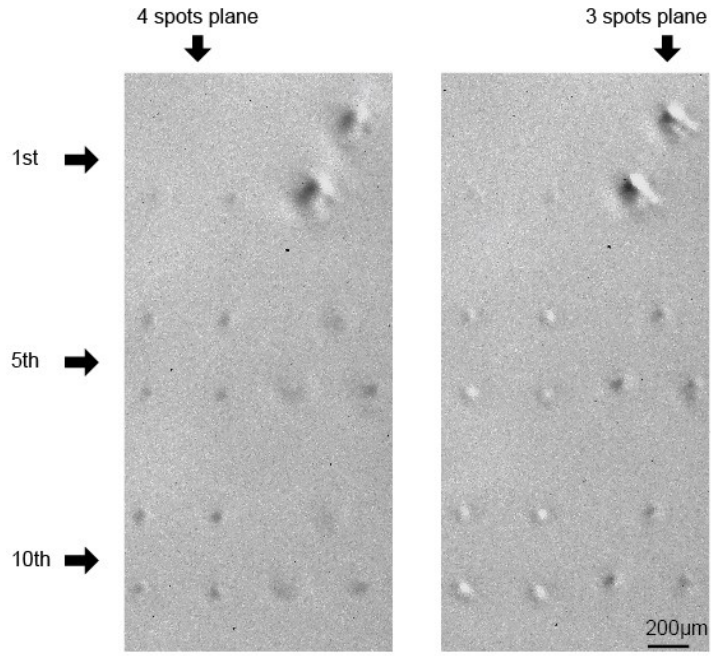

Figure 1.5. 3D patterns processed at different plane inside the glass. 4 spots were processed at the first plane in a rectangle shape, and 3 spots were processed at the second plane in a triangle shape. The 1st, 15th, and 30th represent the iteration orders in the optimization process.

Setup for holographic laser processing

We divide the optical setups used for holographic femtosecond laser processing into three types, which are determined according to the positional relationship between the processing target and the CGH used for spatial pulse modulation, as shown in fig. 1.6.

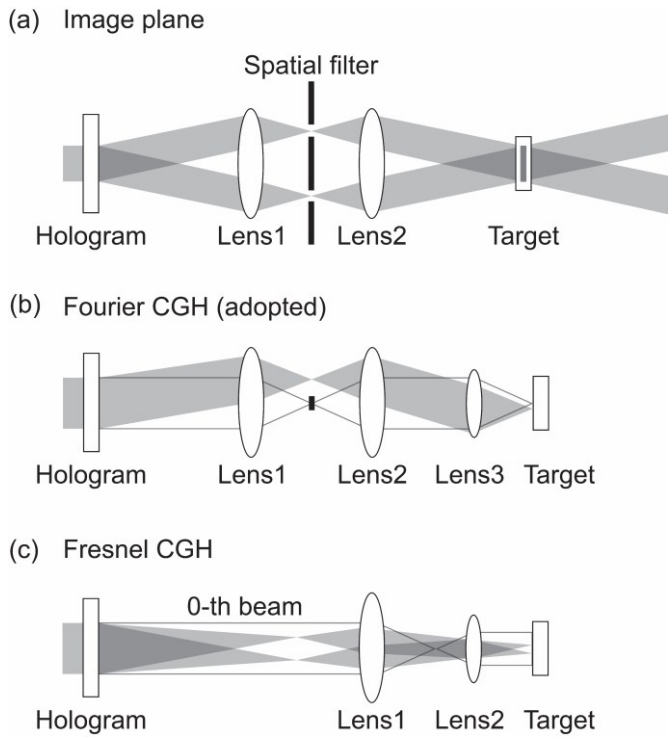

Figure 1.6. Three optical setups for holographic laser processing, with a target placed at (a) the image plane, (b) the Fourier plane, and (c) the Fresnel plane of the hologram.

(a) Image plane

As shown in fig. 1.6 (a), the irradiated beam is divided into multiple beams by a holographic diffraction beam splitter, which passes through the 4f system in the form of interference patterns and finally irradiates the processing target placed on the image plane [33].

In addition, it is necessary to select the corresponding spatial frequency filter and place it on the Fourier plane, which makes the interference mode variability of the diffracted beam possible [34-38].

The advantage of this method is that it can be used to deal with large area periodic structures, in which the spatial frequency filter is spatially invariant, and the modulation of incident light will not change with the change of incident position. Furthermore, if appropriate period and direction factors are added to the ideal position of the diffraction beam splitter, the processing of the variable spatial structure can be realized.

(b) Fourier plane

As shown in fig. 1.6 (b), the irradiated beam is modulated by a Fourier hologram and

passes through the 4f system in the form of a diffractive beam, which is introduced by the object lens and finally irradiated on the processing target located at the Fourier plane.

The advantage of this method is that high quality holograms can be obtained at lower computational cost by using the theoretical basis of diffraction calculation and combining with optimization calculation techniques.

However, in general, the modulated diffracted light contains a zero-order light component, which is generally not needed. Therefore, a spatial filter placed on the Fourier plane can be used to block it, so as to ensure that the zero-order optical components will not enter the subsequent processing system and have an impact on the processing results.

In recent years, some researches on holographic femtosecond parallel laser processing using this optical system have been demonstrated, such as processing with fixed and variable holograms [1,39].

This optical setup is used in our research of holographic femtosecond laser processing. As shown in fig. 1.7, the distance between the focal position of the diffraction spot and the optical axis is defined as the diffraction position r, and the relationship between it and the spatial frequency component ν of the CGH is:

$$r = Ftan[sin^{-1}(\nu\lambda_c)] = F\left[\nu\lambda_c + \frac{(\nu\lambda_c)^3}{2} + \cdots\right] \quad (1)$$

where, F is the focal length of the Fourier plane of the lens, and λ_c is the central wavelength of the light source. Here, when light with central wavelength λ_c is diffracted by fringes with spatial frequency ν on the LCOS-SLM, the diffraction angle θ is given by $\theta = sin^{-1}(\nu\lambda_c)$ [40].

If $\nu\lambda_c$ is sufficiently smaller than 1 (~2×10^{-2} in a real system), then r is approximated as：

$$r = F\nu\lambda_c M \quad (2)$$

where M is a newly introduced magnification given by the reduction optics to match the size of the imaged CGH to the pupil of the objective lens. The Fourier CGH has spatial spectral dispersion, so that the focal spot has spatial broadening Δr given by:

$$\Delta r = F\nu\Delta\lambda M = \frac{r\Delta\lambda}{\lambda_c} \quad (3)$$

where $\Delta\lambda$ is the spectral width. Δr depends on only r if the light source is fixed (λ_c and $\Delta\lambda$

are fixed) [41].

The maximum frequency of CGH is defined as $\nu_{max} = A/(2B)$, when an A*A pixels CGH is displayed on an area of the LCOS-SLM with dimensions B*B. Then the CGH is imaged on the pupil plane with an objective lens with magnification of M, wherein the objective lens is the lens3 in fig. 5b, M is defined as $M = F_2/F_1$, where F_2 and F_1 are the focal lengths of lens1 and lens2, respectively. The side length of the objective lens' pupil plane is $L_{pupil} = BM$. Therefore, the minimum step size in the spatial frequency domain is $1/L_{pupil} = 1/(BM)$. By this, using Eq.(2), the equivalent pixel size p_s on the sample plane can be calculated geometrically as:

$$p_s = \frac{\lambda_c F_{OL}}{L_{pupil}} = \frac{\lambda_c F_{OL} F_1}{B F_2} \tag{4}$$

where F_{OL} is the focal length of the objective lens.

The focal spot diameter d_{Airy} at the sample plane can be calculated from the full width at half maximum (FWHM) of the Airy disk pattern:

$$d_{Airy} = 1.03 \frac{\lambda_c}{AA_{eff}} \tag{5}$$

where $AA_{eff} = R_{pupil}/F_{OL}$ is the effective numerical aperture in the experimental system with the effective beam radius $R_{pupil} = L_{pupil}/2$ at the pupil of the objective lens. Then substituting these operators into Eq.(5) leads to the conclusion that the focal spot diameter d_{Airy} is approximately twice the pixel size p_s, $d_{Airy} \approx 2p_s$. Therefore, magnification M is crucial to adjust the size of the CGH to match the pupil diameter of the objective lens, i.e. $L_{OL} = 2AA_{OL}F_{OL}$. Then AA_{eff} is nearly equal to AA_{OL}, and therefore, the focal spot diameter is minimized.

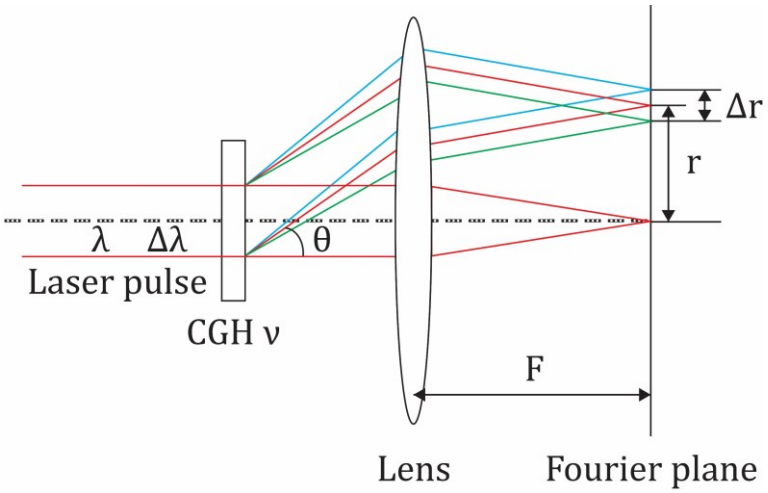

Figure 1.7. Spatial spectral dispersion of the Fourier CGH for a femtosecond laser pulse.

(c) Fresnel plane

As shown in fig. 1.6 (c), the irradiated beam is modulated by a Fresnel hologram and passes through the 4F system in the form of a Fresnel diffraction beam, finally irradiated on the processing target located at the Fresnel plane [2].

In this optical system, due to the separation of zero-order and diffraction beams along the optical axis, the zero-order beam is the background light of the diffraction peak, while the Fresnel diffraction beams are normally used to irradiate to the target.

In particularly, when holographic femtosecond laser processing is used for the processing of transparent materials, it is a multi-photon absorption process based on femtosecond laser, so that the background light does not contribute to the processing.

Using the Fresnel holographic optical system, a single irradiation of 3D parallel processing can be achieved without relying on any mechanical movement to change the axial depth [4]. The focus diameter of holographic lens can be calculated by formula Eq. (4). The maximum numerical aperture of the hologram lens is determined by the pixel size p, namely, $NA_{max} = \lambda_c/2p$. The minimum focus diameter is almost the same as the pixel size p. In fig. 1.6 (c), the focal spot is reduced to the diffraction limit with a set of reduction optics.

Imperfections statement

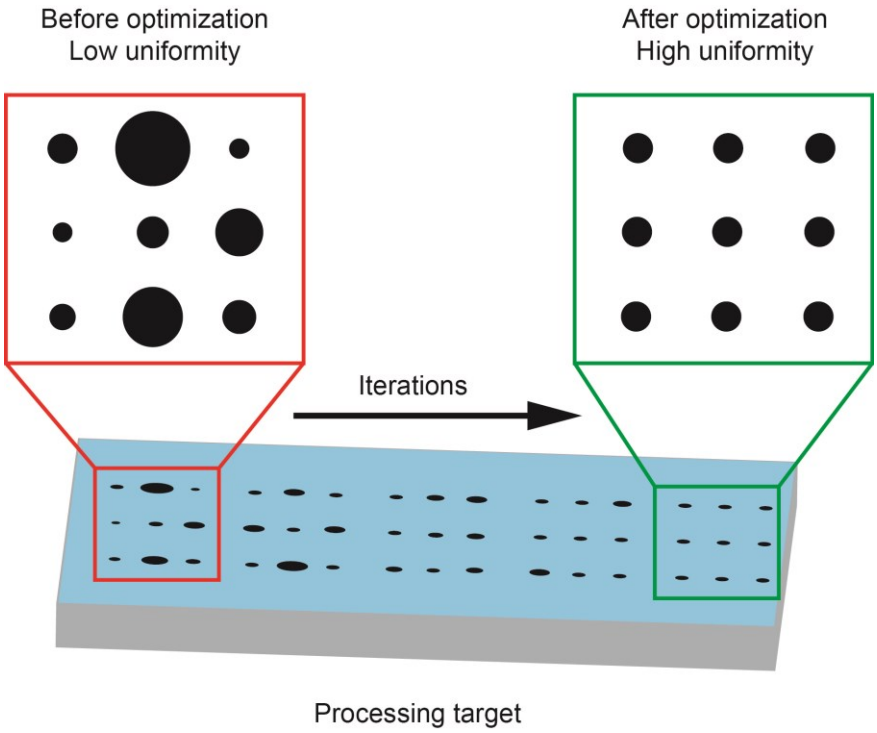

Figure 1.8. Uniformity problem in holographic parallel femtosecond laser processing.

Although the method of holographic laser processing can achieve high throughput parallel processing, however, a key point is the control of the uniformity between parallel beams by the CGH displayed on the SLM. So how to optimize the CGH and obtain the parallel beams with high uniformity has become a technical topic of holographic femtosecond processing, as shown in fig. 1.8.

Due to the imperfections in the laser processing system, the diffraction peaks energy distribution and profile of the reconstructions of the CGH are attenuated. These imperfections in the actual system consist of the static imperfections and the dynamic imperfections. The static imperfections include non-uniform Gaussian or flat beam profiles; non-linearity from the equipment, such as the phase modulation properties of the SLM [42,43]; optical system aberrations from the impurities and the misalignment from the optics, such as the spherical aberration originating from a refractive index mismatch [44]. Another important factor is dynamic imperfections. It includes beam energy and directivity fluctuations originating from the laser source stability, perturbations such as external mechanical movements, air flow, and temperature changes. Especially in the complex

industrial production environment, the stability performance of the laser processing system directly determines the competitiveness of the production technology. Therefore, the imperfections mentioned above will have a great impact on the uniformity of the parallel beams and consequently lead to the inconsistency of the processing results.

1.2 Purpose and orientation of the thesis

The purpose of this paper is to obtain a high uniform light intensity distribution dynamically and improve the stability and flexibility of the holographic femtosecond laser processing system while applying a novel optimization method which called in-system optimization of the CGH. Therefore, how to optimize a CGH by compensating the static and dynamic imperfections simultaneously in the holographic femtosecond laser processing system is a key point in this paper.

As shown in fig. 1.8, after several iterations of optimization, the uniformity of the intensity distribution of the parallel beams will be greatly improved, so when these parallel beams are introduced by the objective lens and irradiated to the processing target, the processed patterns will show a high degree of consistency compared with that before optimization.

1.3 Organization of thesis

Aiming for achieving high-throughput, high-precision holographic femtosecond parallel laser processing, the method of the in-system optimization of the CGH was developed for the compensation of the static and dynamic imperfections exist in the laser processing system which have impacts on the quality of the holographic reconstructed parallel beams and the consistency of the processed structures. The method realized the monitoring and operating system imperfections in real-time due to its feature that it can continuously

optimize the CGH while applying holographic femtosecond laser processing. And the feasibility and practicability of the method are verified through the experimental results. In addition, on the aspects of 2D and 3D CGH design, estimation, implementation, and analysis. Some necessary system components, such as the femtosecond laser source, the LCOS-SLM, the CCD image sensor, and the linear stage, are also explained for their available features. It can be used for many high-precision applications with high-stability in the future. And the thesis has been divided into 6 chapters for the clarification of the gist, as shown in fig. 1.9.

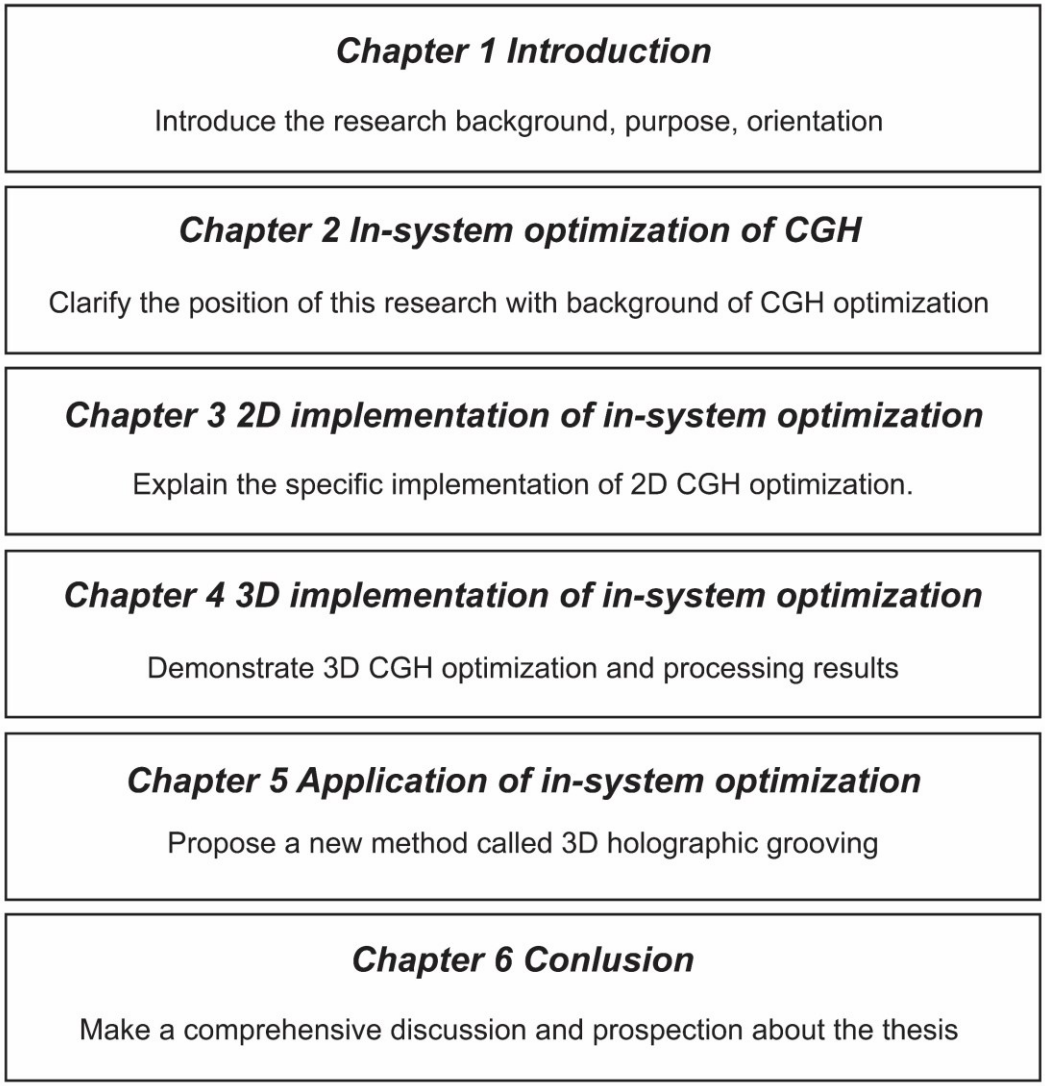

Figure 1.9. Organization of the thesis.

In chapter 1, the background of holographic femtosecond laser processing is introduced in detail, as well as its existing problems, also the purpose, the significance,

and the orientation of this research is clarified, and the organization of the thesis is given.

In chapter 2, the historical view, the features, the classification, and the existing problems of the CGH are firstly introduced. And the optical implementation methods of the CGH are listed and discussed. Most importantly, the classification, significance, and the advantages of the in-system optimization of the CGH are described to clarify the position of this research.

In chapter 3, the 2D implementation of in-system optimization in our research is explained for the first time on the aspects of the optimization concept, CGH design, and uniformity estimation. In addition, some necessary system components, such as the femtosecond laser source, the LCOS-SLM, the CCD image sensor, and the linear stage, are also explained for their available features. Also, the 2D experimental results including optical reconstruction optimization and the corresponding processing are shown. And the advantages and effectiveness of the method in 2D case are verified and substantiated by kinds of environmental experiments, such as vibrations, energy variation, and entrance pupil changes.

In chapter 4, the 3D implementation of in-system optimization for CGH is demonstrated. The key points in this method are the realization of the 3D focusing detection and the recalculation of the corresponding CGH from the detection. The principle, optical setup, observation method, 3D CGH calculation and optimization algorithm, and the experimental results are included. The improvement verification of the 3D focusing uniformity and processing consistency are explored.

In chapter 5, a new application of 3D holographic glass grooving is proposed for the first time. Based on the method mentioned in chapter 4, we successfully designed different kinds of 3D patterns to make a comparison with traditional single-point grooving case. Including the concept, 3D pattern design, practical operations, and the experimental results. The grooving depth and width are investigated in detail to verify the obvious advantages of this method than the single-point one. And the side view results of grooving make the variation of the grooving depth to be possible by adjusting the 3D focusing distribution.

In chapter 6, a comprehensive conclusion of the thesis is made. Mainly consists of the discussion of the research results and the prospection of these works. The results show

that the method in this paper has great application potential. In the future, some remaining topics also need to be further studied, such as the optimization from the workpiece, the compensation for the aberration, the reduction of the time consumption of the iteration, and the novel method for 3D focusing detection, etc.

Chapter 2: In-system optimization of CGH

2.1 Introduction

In chapter 2, the CGH is analyzed and summarized comprehensively under the background of the optimization requirements of high throughput and high precision holographic femtosecond laser processing. First, in the section 2.2, the concept, historical background, characteristics, and classification of the CGH are described. This leads to the type of the CGH we used in this research is the Kinoform, namely a phase-only hologram. In section 2.3, characteristics and disadvantages of the Kinoform are analyzed and sorted out, highlighting the necessity of the optimization. In section 2.4, the optical implementation methods for the CGH optimization are classified, and the position of this research is clarified. It leads to section 2.5, that is, the two refined classifications of the in-system optimization, highlighting the advantages of this research in this classification. Finally, in section 2.6, a general summary of the content of this chapter is made.

2.2 Background of the CGH

For a long time before the holographic technology was developed, how to record the light intensity information and phase information of object wave has become a subject of great concern.

Therefore, in 1942, in order to solve the problem of optical microscopic imaging of weak phase objects, F. Zernike proposed for the first time the phase-contrast filtering microscopy principle, which used the diffraction properties of light to transform invisible phase information in object waves into visible intensity information, and pioneered the optical wave-front transformation [45].

In 1948, in order to eliminate aberration and improve the resolution of electron microscope, D. Gabor proposed the principle of recording and reproducing object wave front by using the interferometric technique and diffraction characteristics of wavefront, namely holography principle, which was called electron holography at that time [46]. Then, in 1960, the advent of laser technology that developed by T. H. Maiman promoted the rapid development of holography [47].

So, in 1963, E. N. Leith and J. Upatnieks obtained the first high-quality holographic reconstruction using laser interferometry, which was called optical holography at the time [48]. Two years later, in 1965, A. Kozma and D. L. Kelly of the University of Michigan constructed a one-dimensional spatial frequency filter for phase-only information processing by calculating the Fourier transform of the signal and drawing a one-dimensional grating consisting only of black and white, which was called computer-generated filter [49]. It was the precursor of computer-generated hologram. Moreover, the first real CGH was developed by Lohmann in 1967, which realized the mathematical calculation of the hologram [50].

Compared with the classical hologram, CGH makes up for its shortcomings and has unique advantages. In order to obtain high-quality classical holograms, strict environmental conditions need to be met, such as air disturbance, the existence of impurities, small vibration, and temperature changes, which will have a serious impact on the quality of classical holograms [51,52]. Moreover, the solution of these problems depends on some sophisticated and expensive equipment. Therefore, these disadvantages of classical holograms limit their usefulness. But for CGH, these problems are easily solved, due to it is actual a kind of interference fringe which replaces the process of optical holographic recording and reconstruction with the computer, as shown in fig. 2.1. The practical features of CGH are as follows:

(i) holograms can be made without the existence of real object wavefront;

(ii) arbitrary wavefronts can be generated according to mathematical models;

(iii) combine with the spatial light modulators, holograms with variable patterns can be realized;

(iv) in addition, if phase-only holograms are used, the theoretical diffraction efficiency

can be close to highly of 100%.

The part replaced by computer is actual a simulation of the interference and the diffraction propagation process of light. This simulation based on computer technology caters to the trend of digitization and artificial simulation of the research object. Because the realization of the digital research object means that the research object can be quantitatively analyzed, and if it can also be simulated manually, it can be more flexible to change any parameters to observe the effect of simulation changes. More importantly, as a combination of holographic technology and computer technology, CGH for the first time introduced the computer into the field of optical processing, making it a strong link between optical information and digital information.

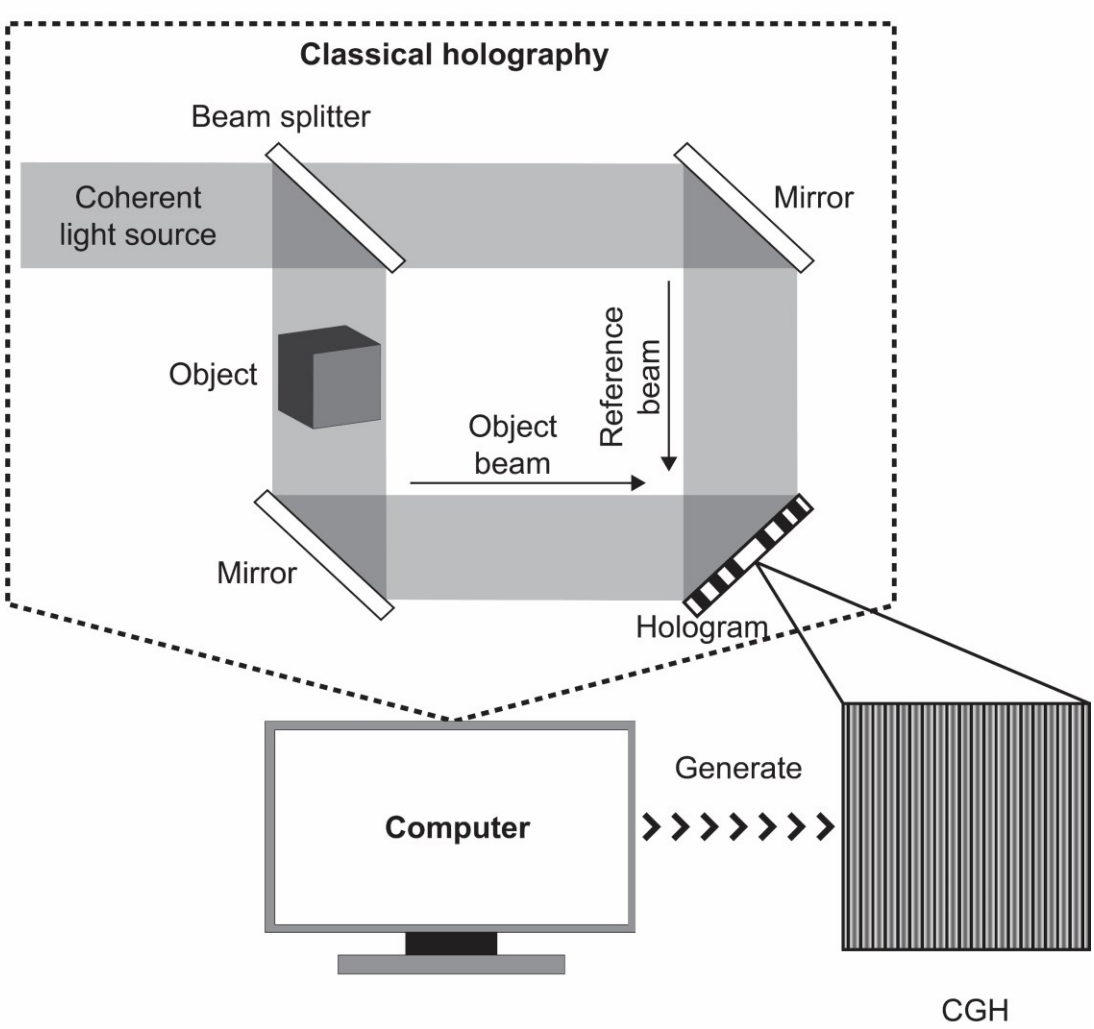

Figure 2.1. Concept of the CGH is actual a kind of interference fringe which replaces the process of optical holographic recording and reconstruction with the computer.

According to the mechanism of the wavefront modulation, the CGH is divided into two major types, namely amplitude type and phase type, as listed in fig. 2.2.

Types			Transmittance	Features	References
Amplitude type	Cell-type	Lohmann	Binary	Amplitude & phase modulated separately	A. W. Lohmann, D.P.Paris,. Appl. Opt. 6, 1739 (1967).
	Cell-type	Lee	Multi-value	Real & imaginary parts modulated separately	W. H. Lee, Appl. Opt. 9, 639 (1970).
	Point-type	Interference fringes	Binary	Isophase description of the wave	W. G. Lee, Appl. Opt. 13, 1677 (1974).
	Point-type	Fresnel zone plate	Binary	Light transmitted transparent zones constructively interferes at desire focus	J. P. Waters,. Appl. Phys. Lett. 9, 405 (1966).
Phase type	Point-type	Kinoform	Constant	Only modulate phase with surface relief, high diffraction efficiency	L. B. Lesem et al,. IBM J. Res. Develop. 13, 150 (1969).
	Point-type	Dammann	Constant	In-line multiple imaging	H. Dammamm, K.Gortler,. Opt. Commun. 3, 312 (1971).

Figure 2.2. Classification of the CGH is sorted into two types, one is the amplitude type and another is the phase type.

Wherein, the amplitude type CGH includes cell-type (such as the Lohmann type [50], Lee type [52]), and point-type (interference fringes [53], Fresnel zone plate [54]). The phase type CGH is mainly point-type, such as the Kinoform type [55] and the Dammann type [56].

As the birth of the first CGH in history, Lohmann type CGH, as shown in fig. 2.3, is of great significance.

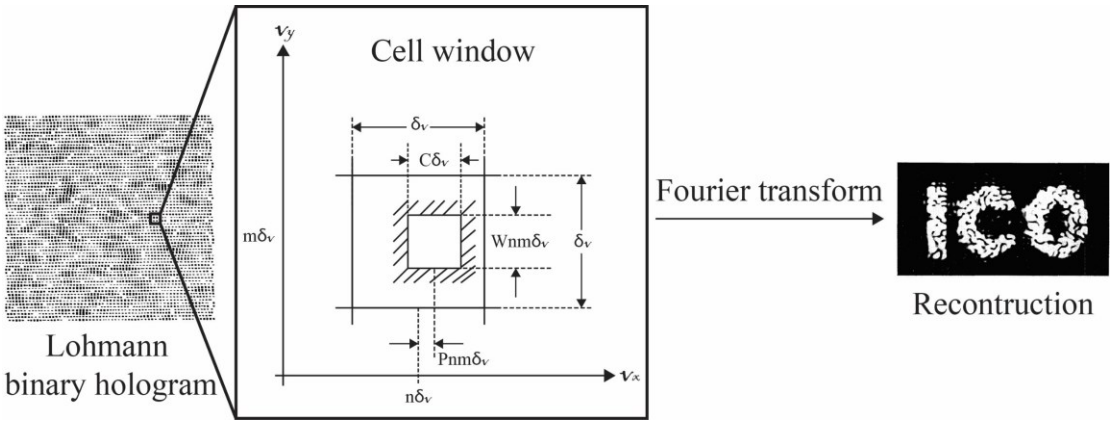

Figure 2.3. Lohmann type CGH and its calculation principle.

The calculation principle is to describe the amplitude and phase information of reconstructed image from the hologram in the form of Fourier transform:

$$u(x,y) = \iint_{-\infty}^{\infty} U(v_x, v_y)\, exp\left[-j2\pi\left(v_x x + v_y y\right)\right] dxdy \qquad (6)$$

where $u(x,y)$ is the complex amplitude of the image plane, and $U(v_x, v_y)$ is the complex amplitude of the hologram plane.

The transmittance of this CGH, has values of zero or unity, namely binary, therefore the transform plane was divided into equal cell windows which contains the opaque and transparent apertures, was defined as the following formula:

$$H(v_x, v_y) = \sum_n \sum_m rectrect\left[\frac{v_x - (n+P_{nm})\delta_v}{c\delta_v}\right] rect\left[\frac{v_y - m\delta_v}{W_{nm}\delta_v}\right] \qquad (7)$$

where v_x and v_y are the spatial frequency coordinates of the hologram. In addition, n and m are the numbers of the cell windows in the v_x and v_y directions, respectively. The size of the cell windows was represented as δ_v, and the W_{nm} and P_{nm} indicate the width of the aperture and the lateral displacement position from the cell window center, respectively. When this CGH is illuminated by a plane wave $E(xv_x)$, and calculated by approximation process, it can obtain $(\delta_v)^2 W_{nm} E[x\delta_v(n + P_{nm})] \approx c(\delta_v)^2 A_{nm} E(\varphi_{nm}/2\pi)$, therefore, the width $W_{nm} \approx A_{nm}$, and $P_{nm} \approx \varphi_{nm}/2\pi$. Consequently, they control the transform's amplitude and phase distribution, respectively. This principle lays a foundation for the subsequent research and development of CGH. Although approximate process may lead to the deterioration of the quality of the reconstructed images, it provides us with a more practical connection between holograms and reconstructed images [57], and a discrete description method for making holograms.

In addition, the phase type CGH called Kinoform will be introduced here, because the wavefront modulation method adopted in this research is based on phase-only hologram.

Kinoform is like a kind of blazed dielectric transmission grating, which proposed a concept that only phase information in the scattered wavefront was necessary in the holographic reconstruction process, so it was called phase-only modulation type of the CGH [55]. The reason for choosing Kinoform rather than other types of holograms is that it has the features of high diffraction efficiency compared with other methods, only real image construction according to the proper phase matching and assumption that the

amplitude set to constant, and on-axis diffraction occurs rather than inclined types without necessary of the separation of the real and conjugate images such as the sampled holograms [57]. For holograms, diffraction efficiency is particularly important, because it determines the practicability and economical use of the reconstructions. Therefore, the discussion on the diffraction efficiency of Kinoform is given in the following contents.

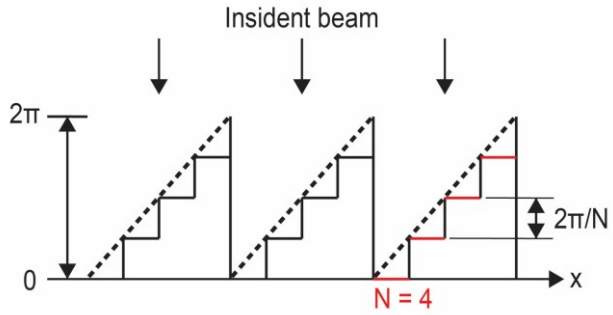

Figure 2.4. Phase-only modulation by Kinoform surface relief transmission grating, where $0\sim2\pi$ rad is the range that the phase can be retarded by the relief, N is the steps in one period of the relief, and $2\pi/N$ is the phase retardance between adjacent steps.

As shown in fig. 2.4, when the incident beam irradiated on the Kinoform surface relief, the phase of that will be retarded by 2π rad. Where N represents the number of steps in one period, and $2\pi/N$ represents the phase retardance between adjacent steps. Therefore, the diffraction efficiency of Kinoform can be calculated according to the following formula:

$$\eta = \frac{I}{I_0} = \left[\frac{sinm\pi/N}{m\pi} \cdot \frac{sin\pi(m-1)}{sin\pi(m-1)/N}\right]^2 \qquad (8)$$

Where η indicates the diffraction efficiency, I denotes the intensity of the diffraction beam, I_0 is the intensity of the incident beam, and m represents the diffraction series. It can be seen from the formula that the more the number of phase steps, the higher the +1-order diffraction efficiency, and the more concentrated light energy, as shown in the following fig. 2.5. For example, if the number of diffraction steps in each period is 256 steps, the theoretical diffraction efficiency can reach approximately 100%.

N \ m	+1	-1
2	$\eta = 40.53\%$	$\eta = 40.5\%$
4	$\eta = 81.06\%$	0
8	$\eta = 94.96\%$	0
16	$\eta = 98.72\%$	0
256	$\eta = 99.99\%$	0

Figure 2.5. Diffraction efficiency variation according to different steps and series.

Although it can obtain a high diffraction efficiency hologram when taking use of Kinoform, the assumption that amplitude equals constant is imperfect in general process of calculating the Kinoform surface relief that increase the intensity distribution at a certain diffraction position, because Kinoform only modulates the phase information in the hologram and preset the amplitude as constant in theory.

The amplitude at the Kinoform is not constant means that the uniformity of the multiple reconstruction peaks will be degraded. Therefore, some methods should be used for improving the uniformity of the peaks, in other words, the optimization of the Kinoform is essentially necessary for future practical application. It will be illustrated in the next section about the optimization methods of Kinoform.

CGH not only inherits the benefits of Kinoform, but also makes a big leap forward in practicality and flexibility due to the combination of computer technology, which can generate arbitrary wavefront distributions without real physical objects.

2.3 Optimization methods of Kinoform

The uniformity optimization of Kinoform has attracted a lot of attention from researchers, and in recent years, many optimization methods has been reported as shown in the fig. 2.7.

(a) demonstrated the Fourier iterative optimization method developed by R. W. Gerchberg and W. O. Saxton, also known as Gerchberg-Saxton (GS) algorithm, it depends on adjusting the amplitude and phase distribution according to the proportion of the

intensities of the target image and the measured image based on the Fast Fourier Transform (FFT) algorithm, gradually approaching the ideal CGH [58]; This method is adopted in our optimization consideration, just as shown in the fig. 2.6. It realizes the cyclic calculation between time domain $U_T = A_T \exp(i\varphi_T)$ and frequency domain $U_R = A_R \exp(i\varphi_R)$, for calculating the phase term, the calculated amplitude A_R after FFT will be replaced by target amplitude A_T after inverse FFT (IFFT) in each iteration. Consequently, make the iteratively calculated phase distribution φ_R approximate to the ideal value that corresponding to the target amplitude distribution.

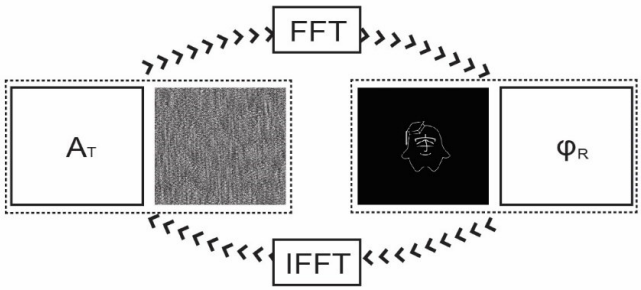

Figure 2.6. Principle of Fourier iterative (GS) algorithm.

(b) explored the direct binary search optimization method that operating the hologram transmittance function to minimize the mean squared error between the reconstructions and original object to produce the best reconstruction based on the Direct Binary Search (DBS) algorithm [59];

(c) illustrated the annealing optimization method that changing a temperature parameter and randomly perturbing the variables to get an optimal binary phase-only matched hologram with simulated annealing (SA) algorithm [60];

(d) reported the shape relative intensity optimization method that to choose an appropriate phase to maximum diffraction efficiency and shape the relative intensity distribution [61];

(e) shown the intermodulation reduce optimization method that to minimize the intermodulation effects between the waves associated with points at the focal plane to get high diffraction efficiency and change the amplitude slightly to obtain uniform array

of spots [62];

(f) explained the optimal rotation angle (ORA) optimization method that calculating diffraction plane amplitude by Fourier transform and maximum desired amplitude by searching optimal rotation angle of the light propagation vector from all the pixels of the diffraction plane to a certain coordinate position in the image plane [63];

(g) elucidated the genetic optimization method that to take use the periodicity of the discrete Fourier transform to quantize the two-dimensional Fourier kinoform with genetic algorithm [64];

(h) stated the lens and grating optimization method that adding lens term to the blazed grating to obtain uniform focus according to the phase shifted along the optical axis [65];

(i) probed the multiplexed phase Fresnel lenses (MPFL) optimization method that searching a set of phase to make the diffraction peaks of the MPFL uniform by reducing the mutual effect [4].

Methods		Principle
(a)	Fourier iterative method	Iterative adjust amplitude and phase CGH with Fast Fourier Transform algorithm.
(b)	Direct binary search	Operate transmittance directly to minize mean squared error of reconstructions.
(c)	Annealing algorithm	Change temperature parameter and perturb variables with simulated algorithm.
(d)	Shape relative intensity method	Choose appropriate phase and shape relative intensity distribution.
(e)	Intermodulation reduce method	Minimize intermodulation effects between focal spots and slightly change amplitude.
(f)	Optimal rotation angle method	Search optimal rotation angle of amplitude direction vector.
(g)	Genetic algorithm	Take use periodicity of discrete Fourier transform to quantize the kinoform.
(h)	Lens & grating method	Add lens term to the blazed grating to obtain uniform forcus.
(i)	Multiplexed phase Fresnel lenses	Search a set of phase that has minimum mutual effect of MPFL.

Figure 2.7. Optimization methods of Kinoform. (a) Fourier iterative optimization method using Gerchberg-Saxton (GS) algorithm; (b) direct binary search optimization method for operating the hologram transmittance function; (c) annealing optimization method that changing a temperature

parameter and randomly perturbing the variables; (d) shape relative intensity optimization method that to choose an appropriate phase to maximum diffraction efficiency and shape the relative intensity distribution; (e) intermodulation reduce optimization method by minimizing the intermodulation effects; (f) optimal rotation angle (ORA) optimization method by searching the optimal light propagation vector; (g) genetic optimization method by quantize the Kinoform; (h) lens and grating optimization method that adding lens term to the blazed grating; (i) multiplexed phase Fresnel lenses (MPFL) optimization method by searching a set of phase to make the diffraction peaks uniform.

2.4 Optical implementation methods of the CGH optimization

The optical implementation methods of the CGH optimization are sorted into three types, as shown in fig. 2.8, (a) is the type that the CGH optimized only in the computer, and then displayed on the SLM and induced into optics for application output; (b) is the type that the properties from the SLM and Optics will be taken into consideration of the optimization of the CGH for a higher uniformity and diffraction efficiency according to the compensation for the properties; (c) is the in-system optimization type that we adopted in this research, the optimization of the CGH will take terminal feedback information, for example, the intensities from the focal spots or the processing scales from the workpiece, into account for a global compensation of the imperfections that exist in the optical systems.

From the point of view of optimization results, mainly the uniformity and diffraction efficiency, the a, b, c three optical implementation methods are compared and discussed.

Firstly, if we take use the (a) type method, a high-quality reconstruction with uniform diffraction peaks can be achieved in the computer, however, the reconstruction in the actual optical system is not ideal like that in the computer when the CGH displayed on the SLM and focused by the optics. For example, the paper demonstrated by Y. Hayasaki, that the CGH was calculated with iterative Fourier transform algorithm (Gershberg-Saxion

algorithm), shown the results that the uniformity of 9 spots' intensities differed from 91% calculated in the computer to 58% measured in the optical system, and the diffraction efficiency was 86.2% when the total irradiation energy was 7.91 μJ, and the 9 micro-holes processed on the sample was vary from 1.29 μm to 1.40 μm, the uniformity of the 9 micro-holes was 92.1% [1].

Secondly, if some properties of the SLM or the optics, such as spatial frequency response, unidentified slight misalignments and impurities, and target material, were taken into the calculation of the CGH for the optimization, just like that shown with fig. 2.8 (b) type method, a higher uniformity of the optical reconstruction can be obtained than that of (a) type. For instance, the method of compensating or the spatial frequency response of the SLM with ORA algorithm was reported by H. Takahashi. The uniformity of the optical reconstruction of 10 spots was differed from 74% that without compensation to 91% that with compensation, and the diffraction efficiency was vary from 60% to 61%. In addition, the uniformity of the 10 micro-holes' scale was 76% due to the diameters differed from 0.94 μm to 1.24 μm in the case with compensation, on the contrast, in the case with compensation, the uniformity was 84% since the diameter range from 0.87 μm to 1.03 μm when the irradiation energy was 1.9 μJ [42]. From the comparison results of whether the spatial frequency characteristics of SLM were compensated, it is obvious that it is necessary to take the properties of optical elements feedback to the optimization of CGH.

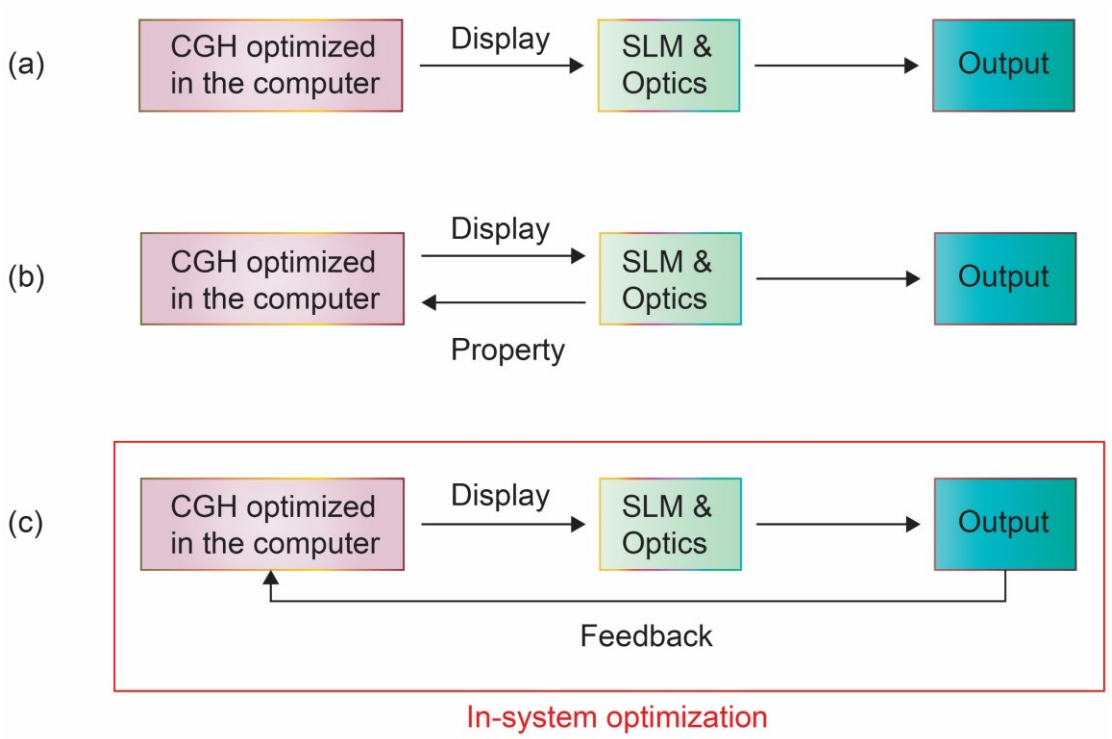

Figure 2.8. Optical implementation methods of the CGH optimization. (a) is the type that the CGH optimized only in the computer, and then displayed on the SLM and induced into optics for application output; (b) is the type that the properties from the SLM and Optics will be taken into consideration of the optimization of the CGH for a higher uniformity and diffraction efficiency according to the compensation for the properties; (c) is the in-system optimization type that we adopted in this research, the optimization of the CGH will take terminal feedback information.

Finally, if the terminal feedback of the optical system can be obtained directly and iteratively, high quality holographic reconstruction could be realized without calculating the specific system imperfections. Optimization methods based on this principle, as shown in the fig. 2.8 (c), is called in-system optimization. A case in point is the method proposed by S. Hasegawa that optimize the CGH based on the uniformity improvement of the measured peak intensity. It is of great significance because the method can realize the compensation for the imperfections of the optical system automatically, no matter the specific imperfections originate from what aspects. The uniformity variation was from 97% that calculated in the computer to 95% that measured in the optical system, the deviation of the two cases was only 2% which is extremely smaller than that of the above two optimization types. And the uniformity of the 10 micro-holes' diameter was 84% when a 1.5 μJ pulse

energy irradiated on the glass sample, although the diffraction efficiency reduced from theoretical of 98% to experimental of 58% due to the spatial frequency performance of the SLM [66]. This method is very useful, especially for industrial applications which strongly depend on the performance of the system and high-efficient production requirement because it can reduce the time consumption by collecting the global information from the optical system used for the CGH optimization rather than searching for a specific problem even people don't know where it is. And the details about in-system optimization will be introduced in the next section.

2.5 Classification in-system optimization

The classification of the in-system optimization is described in fig. 2.9. It is sorted into two types, (a) type is the time-sequential type in-system optimization, and (b) is in-process type in-system optimization which we adopted in this research. The former is characterized by the sequence of optimization and processing, while the latter is characterized by simultaneous optimization and processing.

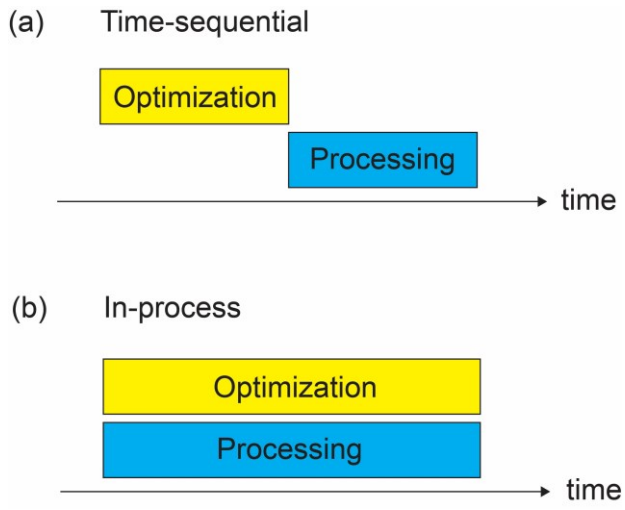

Figure 2.9. Classification of in-system optimization. (a) the time-sequential type in-system optimization, which the optimization and processing are characterized by the sequency; (b) the in-process type in-system optimization, which the optimization and processing are conducted

simultaneously.

As the fig. 2.9 (a) shows, the time-sequential type in-system optimization methods are that the optimization and laser processing are carried out in a chronological sequence, namely after taking the terminal feedback information mentioned above into consideration of the optimization, conducting the laser processing with the optimal CGH. It also can give a high-quality CGH and a satisfactory result in the laser processing system. For example, the typical optimization method based on parallel second harmonic generation detection has been reported by S. Hasegawa [67]. This demonstration taken use of the measured second harmonic as the terminal feedback information generated by irradiating a non-linear crystal with diffraction pulse to estimate the uniformity of the peak pulse intensity which depends on the pulse width and spatial pulse profile, and then optimized the CGH with ORA method until the optimal CGH was obtained, after that the laser processing was applied with the optimal CGH. The uniformities of the 18 parallel peak intensities and the processed structures were 95% and 88%, respectively. And minimum average diameter of 271 nm also has been fabricated on the glass surface due to the improvement on the uniformity.

Therefore, the high uniformity reconstruction and high accuracy laser processing can be realized by using this time-sequential type in-system optimization method.

However, the parallel laser processing was performed after the CGH optimization process with the time-sequential methods, namely the optimization of the CGH was conducted in a static state of the processing system, so it was unable to respond to temporal changes of the optical system in real-time. Therefore, a dynamic optimization method is needed for confronting the complex application environments, such as beam pointing and shape fluctuations originating from the laser stability, external mechanical movements, air disturbance, temperature changes, and temporal fluctuations of the SLM.

To overcome the problem mentioned above, the in-process type in-system optimization method, as shown in fig. 2.9 (b), was proposed in this paper [68]. It can continuously optimize the CGH while applying holographic femtosecond laser processing, provide the advantages of monitoring and operating system imperfections in real time, consequently,

obtain a more stable high-throughput and high-precision femtosecond laser processing system.

2.6 Summary

In this chapter, with the background of improving the uniformity of CGH reproduced images, the historical background, advantages, and optimization methods of CGH are explained and classified, and the purpose and significance of this research are clarified.

In section 2.2, the history, features, significance, types of CGH are mainly narrated from the point of view that what is CGH, what advantages does the CGH has, why a CGH is necessary to compare with a conventional hologram, and what kinds of CGH are developed by researchers.

In section 2.3, the optimization methods of Kinoform, namely the phase-only type CGH which is adopted in this research, are sorted and discussed according to different principles for improving the quality and uniformity.

In section 2.4, the classification of optical implementation methods for CGH optimization are described, namely three types that optimizing CGH only in the computer, considering the characteristics of the components in the optical system into CGH optimization, and optimizing the terminal output of the optical system. In addition, the position of this study in all the methods is clarified.

In section 2.5, the classification of the in-system optimization was given, which is sorted into two types that one is the time-sequential type and another is the in-process type, the later type is the mainly method we used in this research for the attempt of optimizing the CGH continuously while applying laser processing simultaneously in real-time.

Chapter 3: 2D implementation of in-system optimization

3.1 Introduction

In this chapter, the implementation methods of the in-system optimization of 2D CGH used in our research are described. In section 3.2, the concept of 2D CGH in-system optimization for holographic femtosecond laser processing will be explained, including the introduction of the components of the implementation methods and the operation process. In section 3.3, the optical setup will be illustrated, including the performance parameters of each optical element and the modulation characteristics of the laser beam. In section 3.4, the calculation method of CGH is clearly described, and the operation principle of the iterative algorithm will also be described. In section 3.5, it will focus on how to optimize a 2D CGH in the actual optical system and form a closed-loop operation with the computer. In section 3.6, experimental results of the in-system optimization for 2D CGH will be described, including the light intensity uniformity, processing scale consistency, and the environmental perturbation influences. In section 3.7, the general summary about this chapter will be given.

3.2 Concept

The fig. 3.1 shows the concept of the 2D CGH in-system optimization for holographic femtosecond laser processing [68]. The optimization process was performed iteratively by adjusting the light amplitude and phase distribution to approach a target uniformity. The completion of the iterative optimization was based on the orderly information processing

and transmission of the overall system. And the one iteration process mainly consists of the works from a computer, an SLM, optics, and a CCD image sensor. The computer was mainly responsible for the works that the design of the CGH, uniformity optimization, result estimation, the extraction of the light intensity from the captured image, and orderly operation of various components of the overall system. The SLM was used to spatially modulate the incident light. According to the different CGH displayed on the SLM, the modulated spatially shaped beam will present different diffraction patterns, which are the patterns that desired. The optics were used to complete the Fourier transform of the diffraction beams, the formation of the spatial optical reconstructions, and the holographic femtosecond laser processing. The CCD image sensor was a key component of the optimization process because it carried the mission of obtaining the information from the spatial optical reconstructions. This information not only reflects the desired pattern, but also reflects the low uniformity caused by the unknown imperfections from the entire system.

The optical reconstructions of the CGH, detection of the reconstructions, and recalculation of the CGH were iteratively performed based on the rewritable capability of the LCOS-SLM while the laser processing was being performed in the holographic femtosecond laser processing.

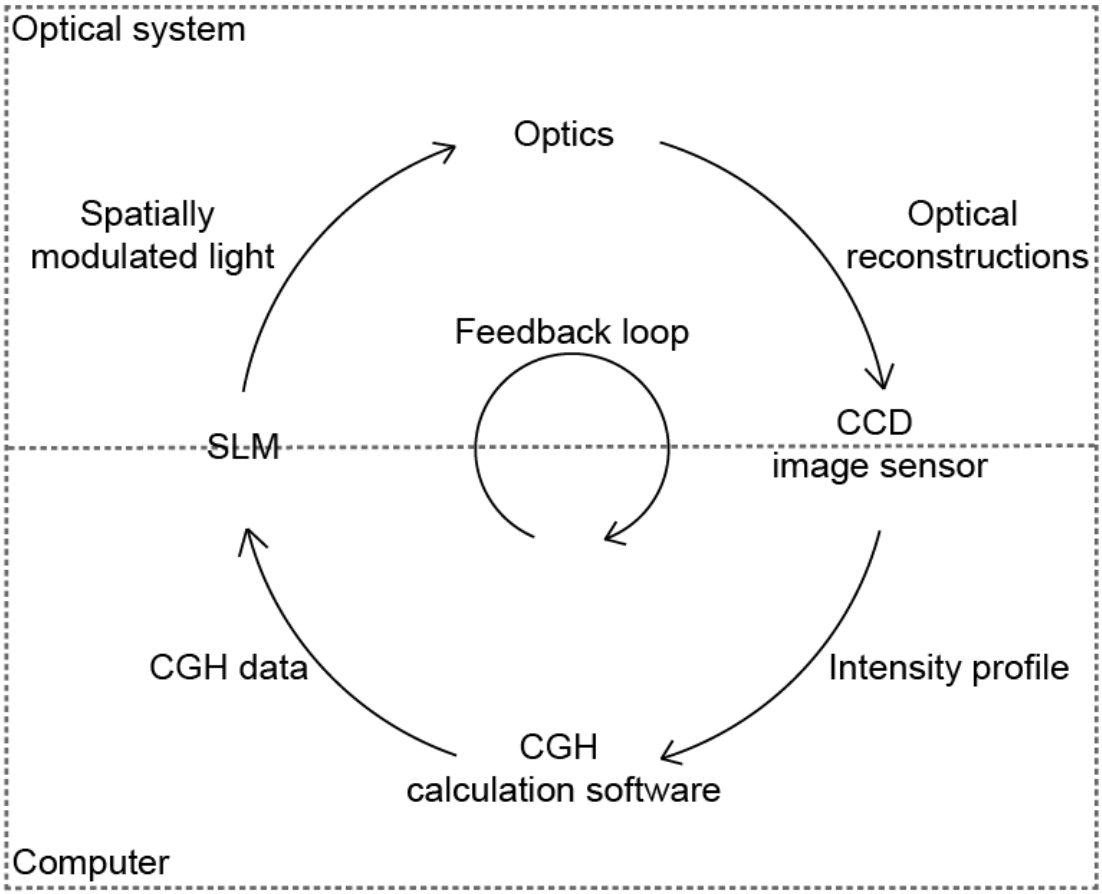

Figure 3.1. Concept of the 2D CGH in-system optimization for holographic femtosecond laser processing.

3.3 Optical setup

Figure 3.2 shows the holographic femtosecond laser processing setup with in-system optimization of the CGH.

A femtosecond fiber laser (IMRA, FCPA μJewel D1000) generated the femtosecond laser pulse with a center wavelength of 1041 nm, a maximum power of 1 W, a repetition frequency of 100 kHz, and a pulse width of ~550 fs.

The pulse energy was firstly adjusted with a set of half-wave plate (HWP) and a polarized beam splitter (PBS), and the light pulse was then collimated by a 2× beam expander (Thorlabs, GBE02-B), which was corresponding to the liquid crystal panel size of the SLM.

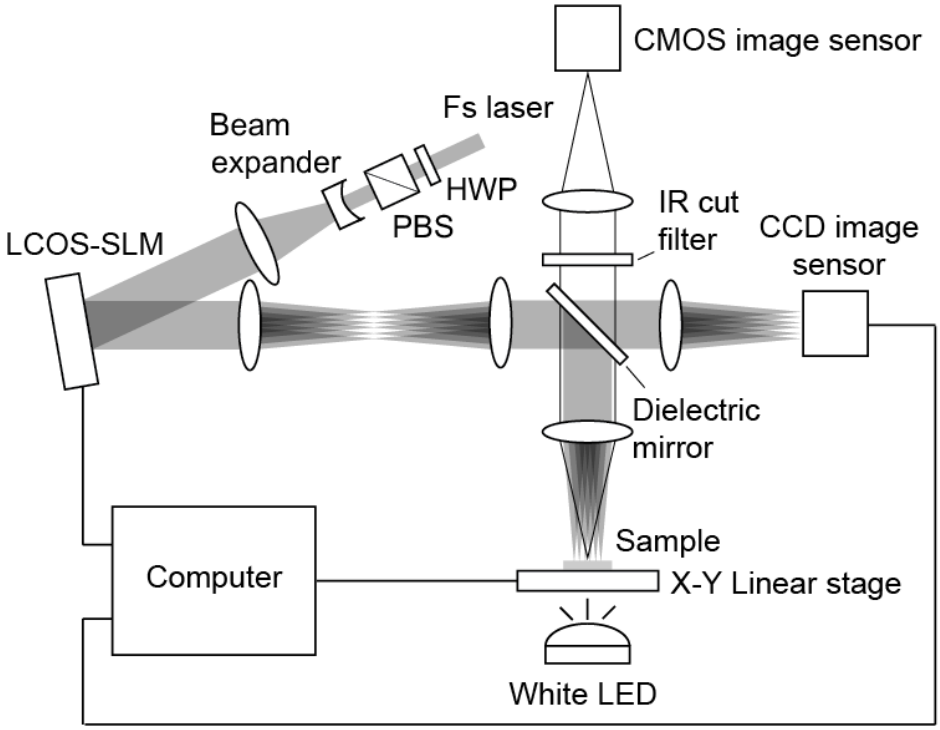

Figure 3.2. Setup of the system for in-system optimization of a 2D CGH for holographic femtosecond laser processing.

The pulse was diffracted by a designed CGH displayed on a reflective liquid-crystal-on-silicon spatial light modulator (LCOS-SLM; Hamamatsu Photonics, X10468), with an operating wavelength range of 1050 $\pm$ 50 nm, a panel size of 15.8 × 12 mm, a pixel resolution of 792 × 600 pixels, a pixel pitch of 20 μm, an aperture ratio of 98%, a gray level of 8 bit (256), a maximum phase depth of 2.359π rad, a 2π rad phase delay was obtained at a gray value of 210 for the wavelength of 1041 nm, a max spatial resolution of 25 lp/mm, a rise response time of 20 ms, and a fall response time of 80 ms.

The fig. 3.3 shows the internal structure of the SLM, and the principle of the phase modulation. The most important part of this structure for phase modulation is the parallel aligned nematic liquid crystal layer. The controller will assign different voltage values to different liquid crystal units according to the different CGH displayed on the SLM, and this voltage value determines the rotation angle of the liquid crystal molecules. After the incident wavefront is modulated by the liquid crystal layer rotated at a certain angle, the

phase delay of the reflected wavefront is determined by the formula $\sigma = (2\pi d/\lambda_0)|\Delta n|$, where d is the liquid crystal thickness, λ_0 is the incident wavelength. And Δn, namely the refraction index, is given by the formula $\Delta n = n_e(\theta_d) - n_0$, where the n_e is the extraordinary refraction index, θ_d is the rotation angle, and n_0 is the refraction index along the optical axis, respectively. In addition, the change of the optical pathlength L can be calculated by the formula $L = sn$, where s is the geometric pathlength, and n is the refraction index mentioned above.

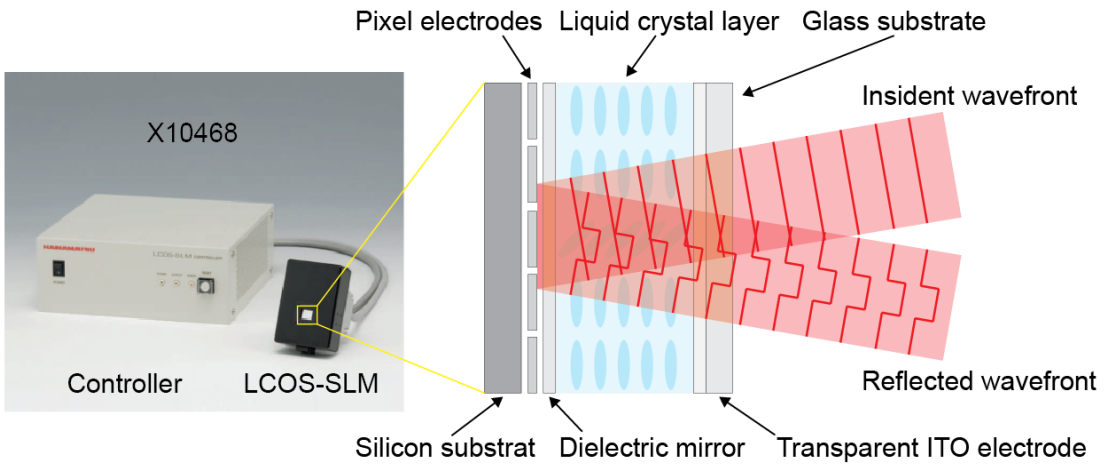

Figure 3.3. Phase modulation concept of the SLM that the incident wavefront can be modulated by the liquid crystal rotation according to the CGH displayed on the SLM.

The phase modulation depth characteristics of the SLM according to the input gray value was shown in fig. 3.4. For the case of the femtosecond laser source with center wavelength of 1041 nm, the capability of the phase modulation is quite adequate, as the test results show that the modulation range has exceeded 2π rad.

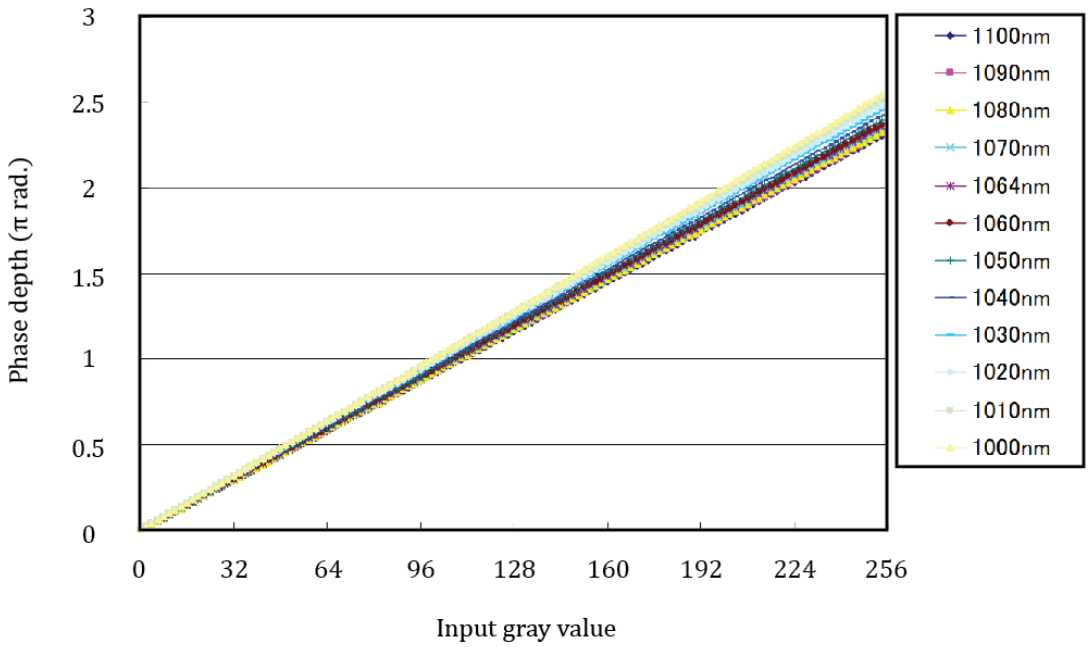

Figure 3.4. Phase modulation characteristics of X10468-03 SLM response to different wavelength. A 2π rad phase delay was obtained at a gray value of 210 for the wavelength of 1041 nm in this setup.

The resulting spatially shaped optical pattern was then reduced with a 50× microscope objective (Mitutoyo, Apo NIR HR), with a numerical aperture (NA) of 0.65, and was made incident on a sample fixed on a linear stage (Aerotech, ANT95-50-XY-MP).

A complementary metal–oxide–semiconductor (CMOS) image sensor (Imaging Source, DMK33UP1300), a white LED, a lens, and an IR-cut filter were used to monitor the laser processing.

Partial light intensity of the spatially shaped pattern was incident on a charge-coupled device (CCD) image sensor (Imaging Source, DMK23U274) with 1600 × 1200 pixels having a pixel size of 4.4 μm × 4.4 μm, 8-bit A/D conversion, and a frame rate of 20 frames per second through a dielectric mirror (Thorlabs, BB1-E03P) for in-system optimization of the CGH, and captured images data were transferred to a personal computer.

3.4 CGH calculation

The 2D CGH calculation was completed with a modified version of the weighted iterative Fourier transform (WIFT) method [69]. As shown in fig. 3.5, the flow char of the 2D CGH calculation, a uniform initial amplitude and an initial phase distribution were input into the iteration for the calculation, where the initial phase can be a random one or an approaching one to the target CGH, and i represented the iteration time. And the diffraction calculation of the complex amplitude was performed by the Fast Fourier transform (FFT) and the inverse Fast Fourier transform (IFFT) [70]. The target was desired pattern with uniform parallel beams, and the weighting was the process that assigned different weight values to different diffraction peaks by using the WIFT method for adjusting the differences between the intensities. The calculation of the CGH was conducted in finite times iterations until a satisfactory uniformity result was obtained, and according to our experimental experiences, we preset $i = 30$ times for the calculation and optimization.

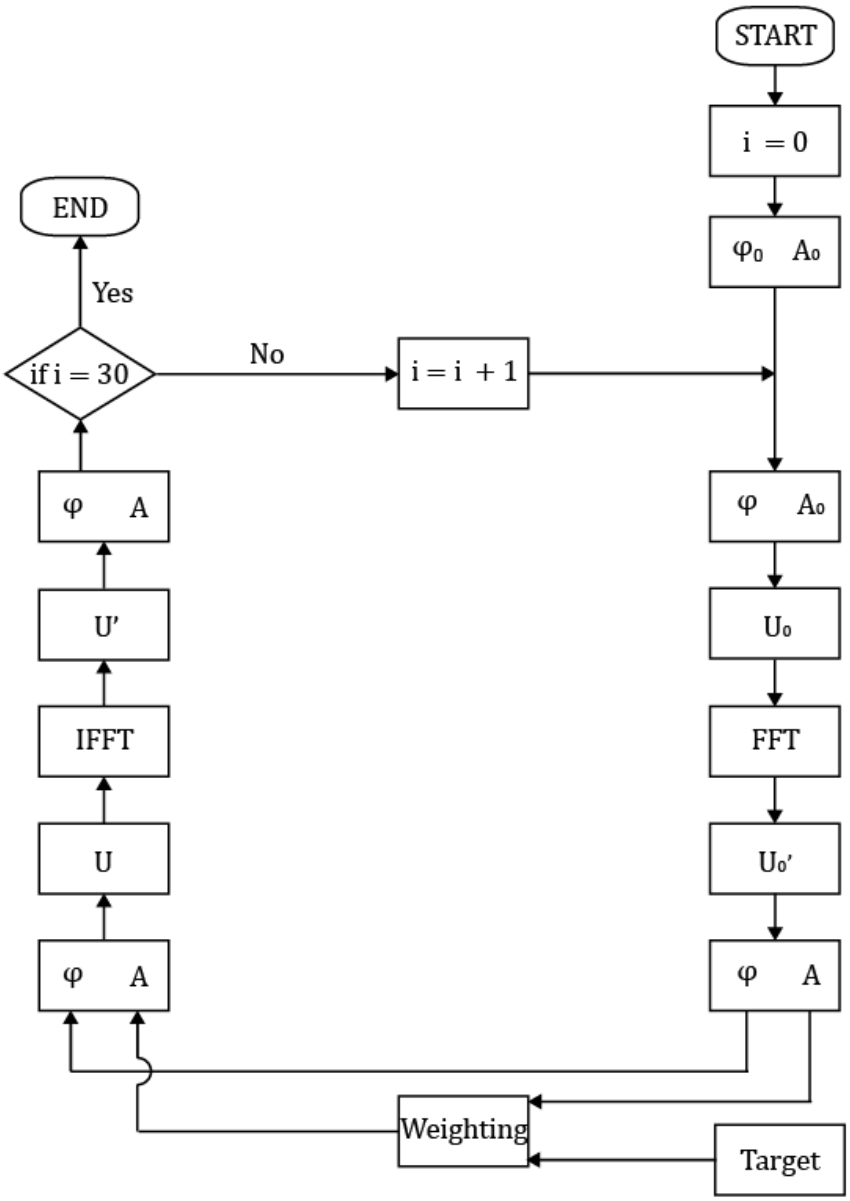

Figure 3.5. Calculation flow chart of 2D CGH principle.

3.5 CGH optimization

The optimization method was completed by the observation method of the intensities of the diffraction spots at the Fourier plane in the actual optical system and the CGH recalculation in the computer, as the schematic shown in fig. 3.6. The green circle indicates the region of one diffraction spot captured by the image sensor. And the red square represents the intercepted part in the diffraction spot region. The gray values of all the

pixels in the red square will be summed up as the measured intensity for the estimation calculation. The measured intensity I_m of each diffraction spot was calculated by summing the pixel values within the red square region. If the target light intensity I_t is set to a constant 1, then a normalization process of the measured one I_m is needed. The intensity adjustment was performed with the equation $w(n) = [I_t(n)/I_m(n)]^{\alpha}$, where $w(n)$ is the weighting value of the nth diffraction spot, and $I_t(n)$ and $I_m(n)$ are the target uniform intensity preset before the optimization and the measured intensity by the CCD image sensor in each iteration, respectively.

The estimation of the uniformity was calculated according to the criterion $U = I_{min}/I_{max}$, where I_{min} and I_{max} are the minimum and maximum intensity in all the diffraction spots, respectively.

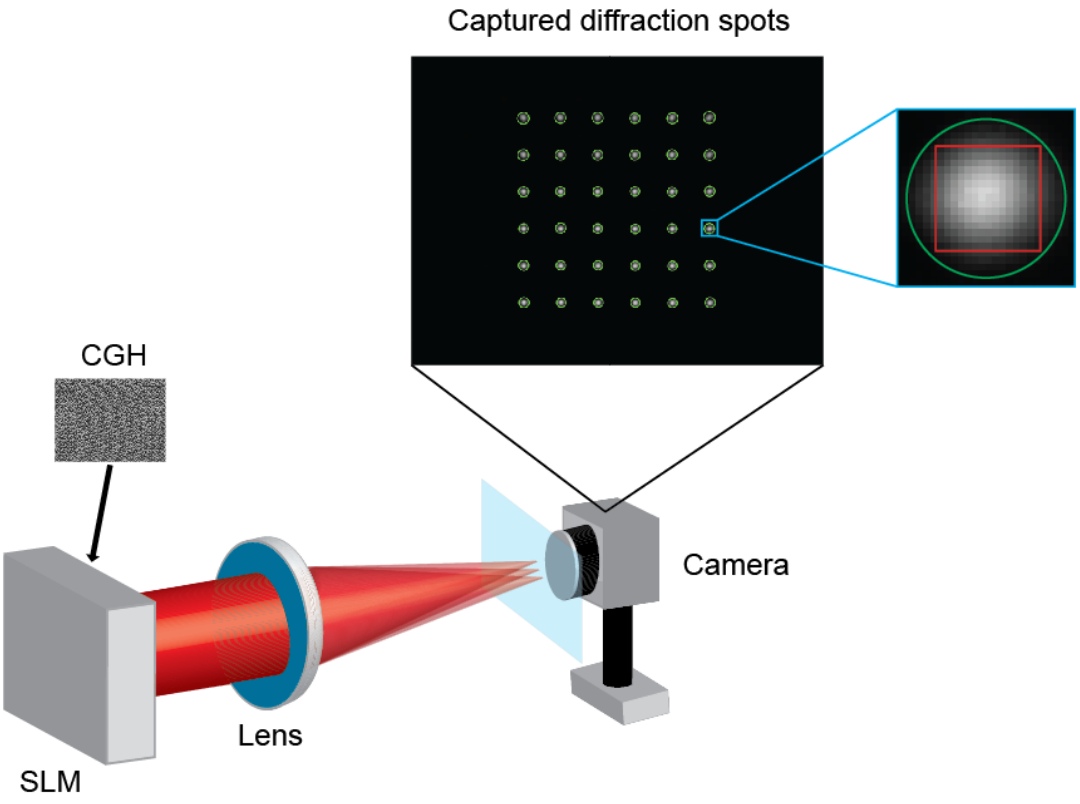

Figure 3.6. Observation method of intensities of the diffraction spots at the Fourier plane in the actual optical system for the CGH optimization. The green circle and the red square indicate the diffraction spot region and the value summation region in pixels, respectively. The sum of all pixel values within the red square represents the intensity of the diffraction spot.

3.6 Experimental results

The 2D in-system optimization results were obtained by using the optical setup in the fig. 3.2.

Figure 3.7 shows the process of in-system optimization for 36 diffraction spots. Figure 3.7 (a) shows the initially optimized CGH. The CGH shown here is, actually, the grayscale image displayed on the SLM, and the grayscale value is used to represent different phase information. Figure 3.7 (b) shows the initially reconstructed pattern. Figure 3.7 (c) shows the optimized CGH. Figure 3.7 (d) shows the optimized reconstruction detected by the CCD image sensor. The spacing between the diffraction spots was 391.6 μm on the image sensor plane, and the corresponding spacing on the sample plane was 7.9 μm. The diffraction efficacy was 86.61%. Figure 3.7 (e) shows temporal traces of the 36 diffraction spot intensities. Three U curves are shown, a red dotted line, a black dotted line and a blue dotted line, which represent the changes in uniformity when a parameter in the WIFT method α was equal to 1/4, 1/6, and 1/8, respectively, as calculated with the weight $w(n) = [I_t(n)/I_m(n)]^{\alpha}$ for the nth diffraction spot mentioned in this chapter. It can be seen from the trend of the three uniformity curves that the larger α is, the faster the optimization speed and the more uneven the curve, whereas the smaller α is, the slower the optimization speed and the smoother the curve. The 36 diffraction spots gradually became uniform, and U reached a maximum value of 0.98 from the initial value of 0.27 after 100 iterations based on the criterion $U = I_{min}/I_{max}$. The amount of time for the 100 iterations was 110 seconds, depending on the response time of the LCOS-SLM, the image capturing time of the CCD image sensor, and the calculation times of the FFT, image processing operations, and some other signal processing operations in the computer.

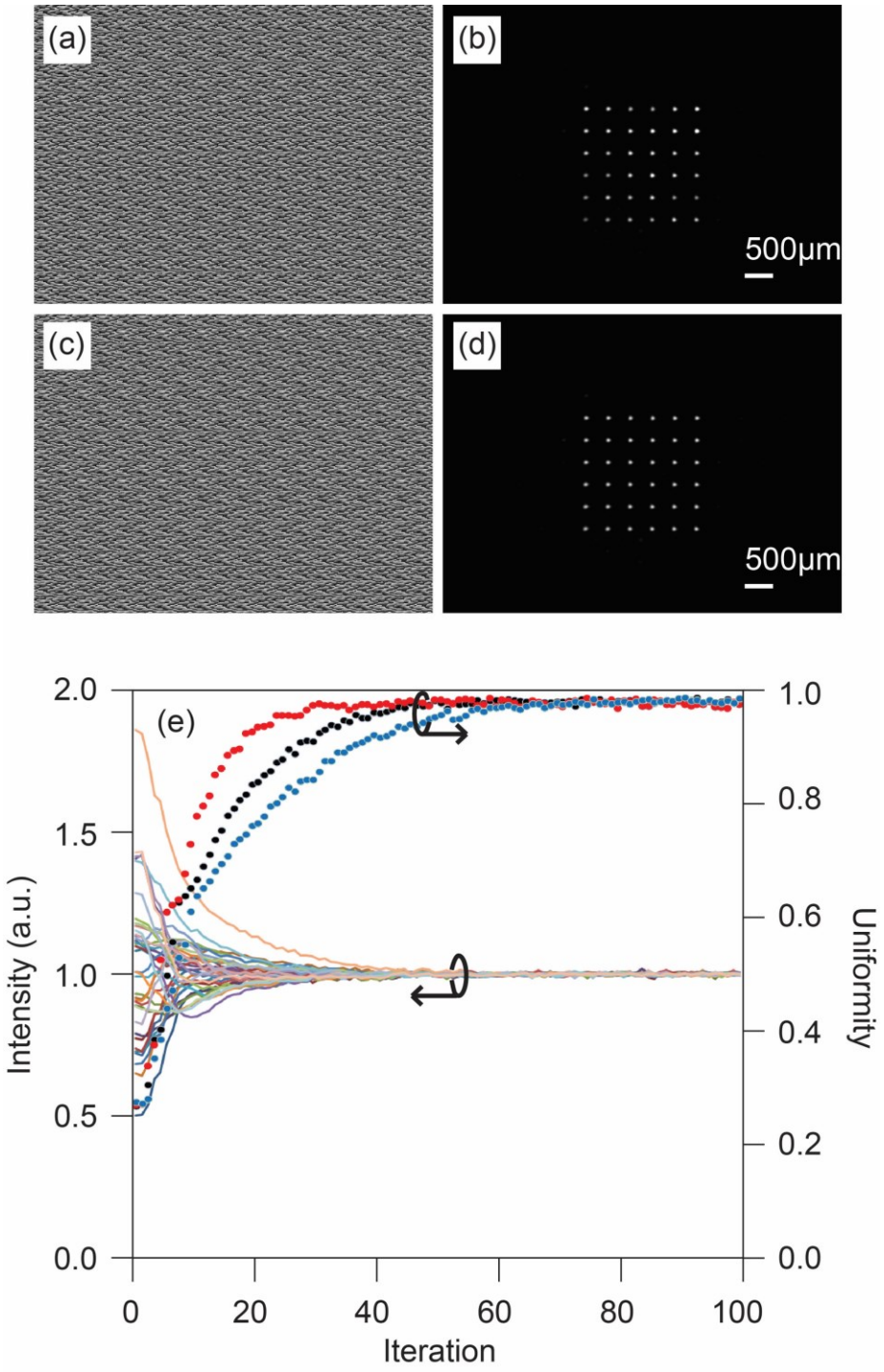

Figure 3.7. The variation of the spot intensity and the uniformity of in-system optimization for 36 diffraction spots: (a) the initially optimized CGH; (b) the initially reconstructed pattern; (c) the optimized reconstruction of the CGH; (d) the optimized reconstructed pattern; (e) the temporal traces of the 36 diffraction spots and three U curves, where the red dotted line, the black dotted line, and the blue dotted line represent the trend of uniformity changes when α was equal to 1/4, 1/6, and 1/8, respectively.

Figure 3.8 shows the investigation of different α values for the 200 times uniformity optimization of 36 diffraction spots. As α variated from the value of 0.02 to 0.8, it can be seen from the trend of the uniformity curves that the larger α is, the faster the optimization speed and the more uneven the curve, whereas the smaller α is, the slower the optimization speed and the smoother the curve. When the α comes to 0.8, although the speed of optimization was very fast, it showed obvious fluctuations, and the uniformity began to decline sharply after about 190th iteration. Therefore, the value of 0.8 was a limit in this experiment.

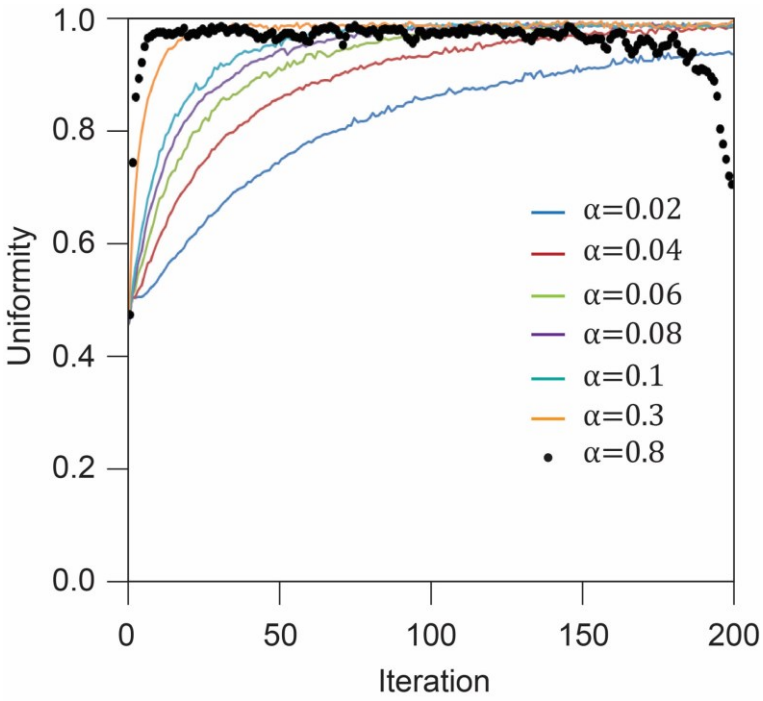

Figure 3.8. Investigation of different α values for the uniformity optimization. As the α variated from 0.02 to 0.8, and the curves were smoothing.

Figure 3.9 shows holographic parallel laser fabrication while applying in-system optimization of the CGH. The energy of the incident laser pulse to LCOS-SLM was 3.75 μJ. The total pulse energy of the seven focal spots was 2.40 μJ on the sample, and thus the average energy of the seven focal spots was 0.34μJ, which was a little higher than the ablation threshold of 0.30 μJ. Seven parallel focus beams were radiated onto a glass surface (super-white crown glass, thickness 0.8 ~ 1 mm) (Schott, B270) with one-

directional lateral translation. The parallel focus beams gradually became uniform. Figure 3.9 (a) shows the temporal traces of intensities of the seven parallel spots and the U curve. Figures 3.9 (b) – (d) show the fabrication areas around at the 5th, 50th, and 100th iterations of the CGH optimization, respectively. The images were obtained by a field-emission scanning electron microscope (FE-SEM) (Hitachi, S-4500). At the 5th iteration, the line structure had width variations of 0.80 to 1.19 μm, and the uniformity of the width reached only 0.67. At the 50th iteration, the width variations were 1.15 to 1.19 μm, and the uniformity was improved from 0.67 to 0.97. Finally, at the 100th iteration, the width variations had become uniform at 0.98 to 0.99 μm, showing that the uniformity of the width reached the optimal value of 0.99.

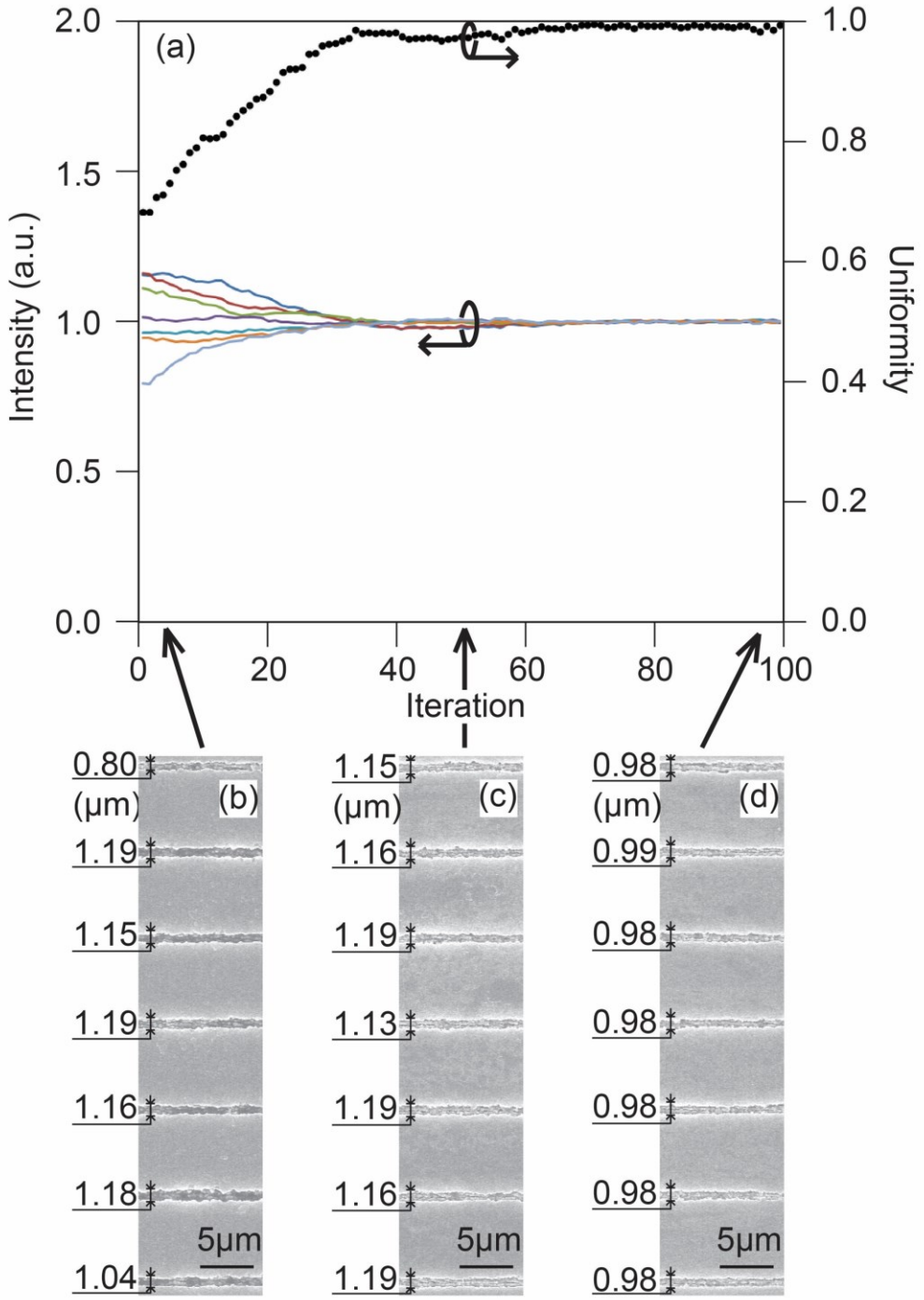

Figure 3.9. Seven holographic parallel lines laser fabricated while applying in-system optimization of CGH showing (a) the temporal traces of the seven parallel spots and U. The ablation results of the 7 lines at (b) the 5th iteration, (c) the 50th iteration, and (d) the 100th iteration of the optimization.

We also conducted environmental experiments concerned about the vibration, the

intensity variation and the entrance pupil variation in the procedure of in-system optimization.

Figure 3.10 shows the process of in-system optimization for 36 diffraction spots. The difference from the results shown in fig. 3.7 is that external vibrations were intentionally applied to the laser processing system. The external vibrations were given by applying an impact to the breadboard on which the LCOS-SLM module was fixed. At around the 40th and 80th iterations, the intensities fluctuated and, as a result, the uniformity decreased suddenly. However, after several iterations of in-system optimization, the spot intensity reached the uniform value again, and of course, the uniformity returned to the optimal result again. Therefore, we consider that, although vibration factors in the actual laser processing environment have a significant impact on the optical system, we can re-optimize the uniformity in real time by using in-system optimization, and can achieve satisfactory results.

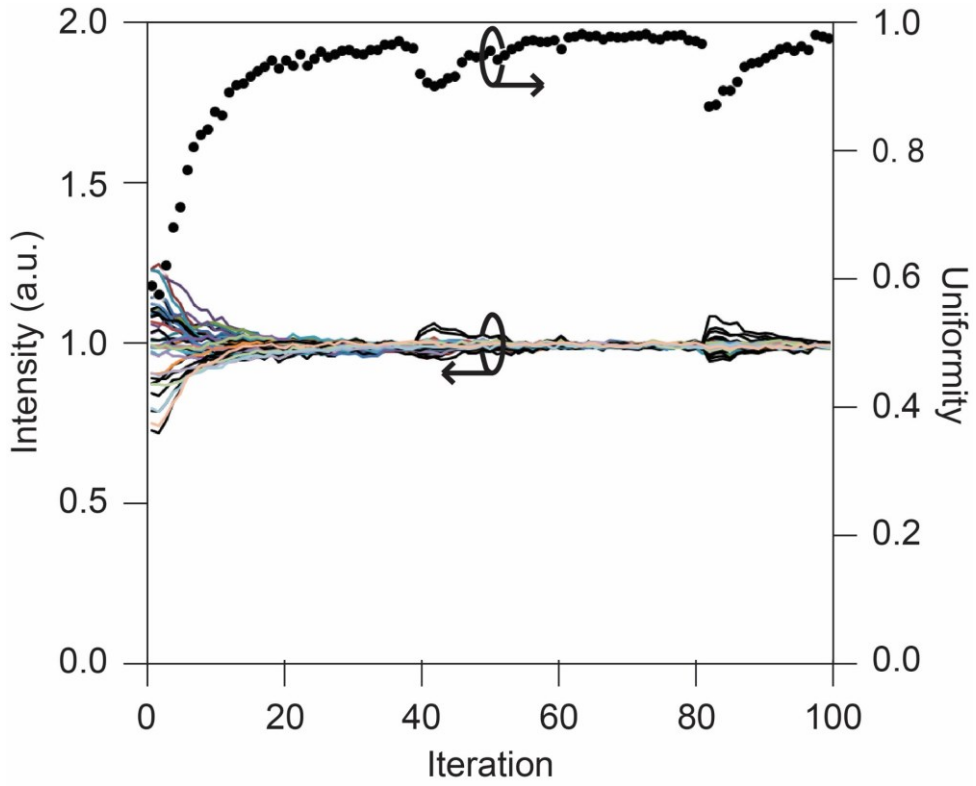

Figure 3.10. The variation of the spot intensity and the uniformity by applying vibrations two times during the processing of the in-system optimization for 36 diffraction spots.

In order to make a clear contrast with the system without optimization performance,

we summarized the results of the two systems after one-time vibration as shown in fig. 3.11. According to the discussion of the results in fig. 3.10, the vibration resulted in the fluctuation of the spot intensities and the uniformity decreased in the same time. In terms of the system with optimization, the spot intensities can be unified and the uniformity also can be re-optimized to the optimal value of 0.98. On the contrast, the other system that without optimization, kept on the decreased uniformity until the end of the procedure. Therefore, although the environmental factors such as vibration are inevitable in the procedure of practical laser processing, but in our work, we successfully maintained the uniformity of the diffraction spots in a high degree.

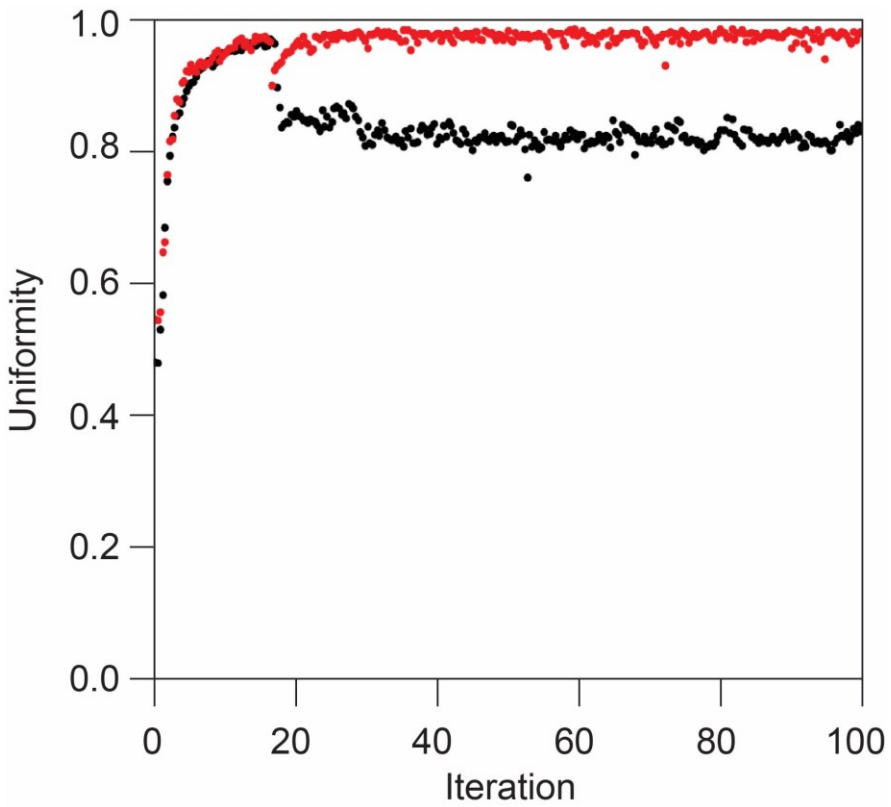

Figure 3.11. Schematic of the comparison between the system with optimization performance and the system without optimization performance by conducting one-time vibration in the procedure of the in-system optimization for 36 diffraction spots.

Figure 3.12 schematic of the results of the variation of the spot intensity and the uniformity by changing the energy pulse of in-system optimization for 36 diffraction spots.

As be seen from the graph which indicates spot intensity versus iteration in fig. 3.12, the lines in different colors represents the spot intensities of 36 diffraction peaks, even the pulse energy increased by 50% at about 50th time of iteration by adjusting HWP, resulted in all the intensities of diffraction spots raised to a high level simultaneously, but the uniformity was still highly consistent. And a comparison between two energy states was shown in the graph which indicates uniformity versus iteration, they illustrated an extremely similar curve in the whole procedure of in-system optimization, where the black dot and the red dot in the graph represent the stable energy state and the unstable energy state, respectively. Thus, in our opinion, this experiment simulated the actual case that even the laser pulse conducted unstable state, for instance, pulse energy increases suddenly or decrease suddenly, there were almost no influence on the optical system by taking advantage of our in-system optimization method.

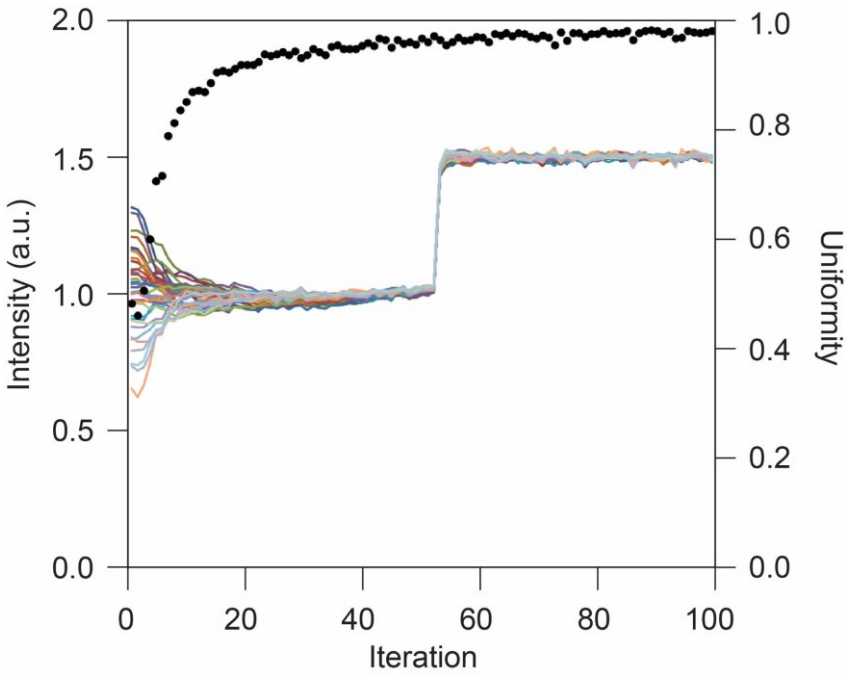

Figure 3.12. Schematic of the results of the variation of the spot intensity and the uniformity by changing the energy pulse in the procedure of the in-system optimization for 36 diffraction spots.

Figure 3.13 illustrates the results of the variation of the spot intensity and the uniformity by changing the diameter of the entrance pupil in the procedure of the in-system

optimization for 36 diffraction spots. We expanded the diameter of the entrance pupil at about 50th of the iteration, it resulted in an increase in the amount and the diameter of the incident light, consequently, it led to the spot intensities differ from each other again and the decrease in uniformity due to the transformation of nonlinear irradiance. However, with the spot intensities have been unified by times of optimization the uniformity also returned to the optimal value in finally.

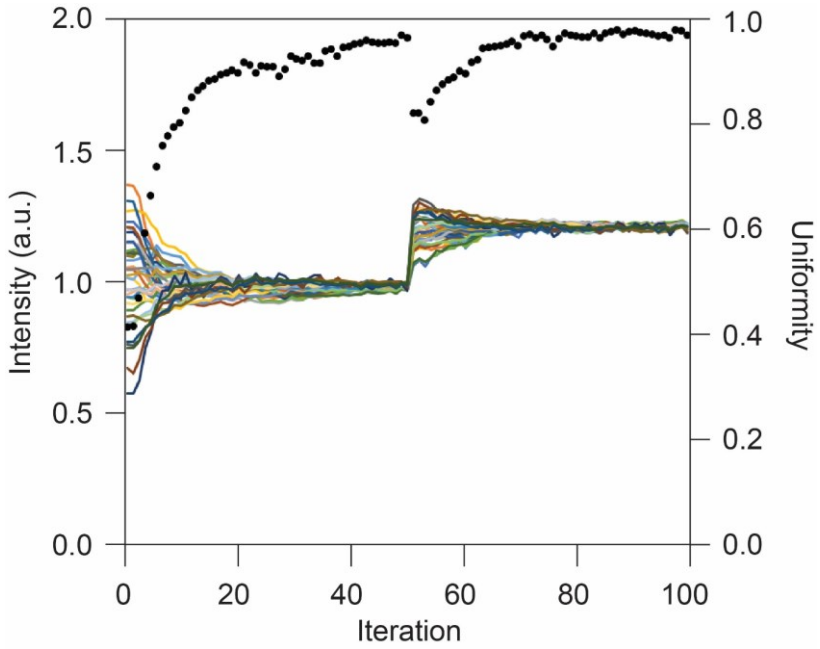

Figure 3.13. Schematic of the results of the variation of the spot intensity and the uniformity by changing the diameter of the entrance pupil in the procedure of the in-system optimization for 36 diffraction spots.

3.7 Summary

In this chapter, the implementation is given from the perspective of the specific method and principle of realizing the in-system optimization for 2D CGH. In section 3.2, it is the first time to propose the concept that can realize the holographic laser processing while applying optimization by combining optics and computer systems. As for section 3.3, the

successful construction of the optical system realizes the effective combination of computer and optical elements and makes the processing process of optical information visual and in real-time. In section 3.4, the iterative calculation method based on WIFT is described in detail, and through this method, the object information contained in CGH can gradually approach the target value, so as to calculate the optimal CGH for laser processing. In section 3.5, the necessity of CGH in-system optimization in the practical optical systems is emphasized, that is, there are static and dynamic imperfections in the system. The method in this paper can carry out specific optimization methods for different setups to ensure optimal performance. In section 3.6, the experimental results verify the feasibility and effectiveness of the method. These results include the optimized 2D CGH, the uniform optical reconstructions, and the ability to withstand external interference in real-time operations. Not only the static imperfection is effectively compensated to make the spot uniformity reach the ideal value, but also the experimental results of a series of dynamic disturbances such as vibration can further prove that this method can provide high stability performance in practical industrial production. The feasibility, necessity, and effectiveness of the in-system optimization are proved by the experimental results, and the stability and precision of the holographic femtosecond laser processing system can be improved.

Chapter 4: 3D implementation of in-system optimization

4.1 Introduction

In this chapter, the implementation methods of in-system optimization of three-dimensional (3D) CGH for holographic laser processing will be demonstrated, especially the observation way of 3D focusing and the corresponding CGH recalculation from the observation. In section 4.2, mainly introduces the concept of the feedback control for 3D focusing and processing. The functions and operation mechanism of the four components in the system are outlined, especially the detection module for 3D focusing is proposed for the first time. In section 4.3, the optical setup based on the above principle is explained in detail. And among the optics, the automatic control of some components is introduced to realize the iterative capturing and optimization of 3D focusing. In section 4.4, introduces how the cooperation between the imager and the linear stage under the control of the computer realizes the observation of 3D focusing information step by step. In section 4.5, the specific method of calculating CGH containing 3D information based on angular spectrum (AS) method is described. In section 4.6, the optimization calculation and evaluation method of 3D CGH are explained, which is based on the combination of WIFT algorithm and AS method mentioned above. In section 4.7, shows the experimental results about the feedback control of the 3D focusing, the optimized CGH, and the improvement of 3D laser processing. And in section 4.8, we will give a summary about this chapter.

4.2 Concept

Figure 4.1 shows the concept of three-dimensional holographic parallel focusing with feedback control for femtosecond laser processing [71]. The feedback system mainly consists of an optical system and a computer, and has four components including a CGH calculation software, an SLM, an optics, and a 3D focus detection module (3D-FDM). The CGH calculation software is used for optimizing the CGH. The SLM modulates the incident wavefront with CGH data calculated in the computer. The optics are customized for an application, in this research for femtosecond laser processing. The 3D-FDM obtains the 3D optical reconstructions of the CGH and transfers the data to the computer. The key points of this feedback system are the implementation of the 3D-FDM and the corresponding CGH recalculation for 3D parallel focusing. They were details in the next paragraphs in this section.

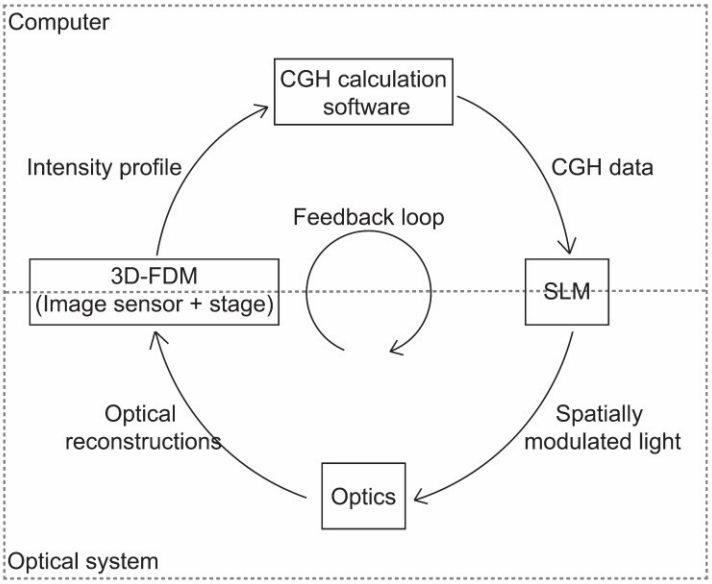

Figure 4.1. Concept of the feedback control for 3D parallel focusing.

4.3 Optical setup

Figure 4.2 (a) illustrates the schematic of 3D holographic laser processing system with feedback control of 3D parallel focusing. Figure 4.2 (b) and (c) show the laser machining head and the details of the 3D-FDM. Figure 4.2 (d) shows a photograph of the actual

experimental setup. The generation of the femtosecond laser pulse was from a femtosecond fiber laser (Light conversion, PHAROS), with a center wavelength of 1030 nm, a repetition frequency of 10 kHz, and a pulse width of ~150 fs. A set of a half-wave plate (HWP) and a polarized beam splitter (PBS) was used to adjust the pulse energy, and a 2× beam expander (Thorlabs, GBE02-B) was used for the collimation of the laser pulse. The 3D pattern was optically reconstructed after the pulse diffraction that occurred on a liquid-crystal-on-silicon spatial light modulator (LCOS-SLM; Hamamatsu Photonics, X10468-03) which a pre-designed CGH displayed on it.

Then the 3D pattern was separated into two light arms by a dielectric mirror (Thorlabs, BB1-E03P), one was detected by the 3D-FDM detailed shown in the fig. 4.2 (c), mainly completed with the imager 2, a charge-coupled device (CCD) image sensor (Imaging Source, DMK23U274) with 1600 × 1200 pixels having a pixel size of 4.4 μm × 4.4 μm, 12-bit A/D conversion, and a frame rate of 20 frames per second (fps), a lens with a focal length of 200 mm, and a programmable linear stage 3 (SIGMA, SGSP-25ACT) to carry the imager to different focal positions iteratively for the feedback control of the 3D parallel focusing. In addition, the imager 2 output was transferred to a personal computer for the estimation and calculation of the CGH.

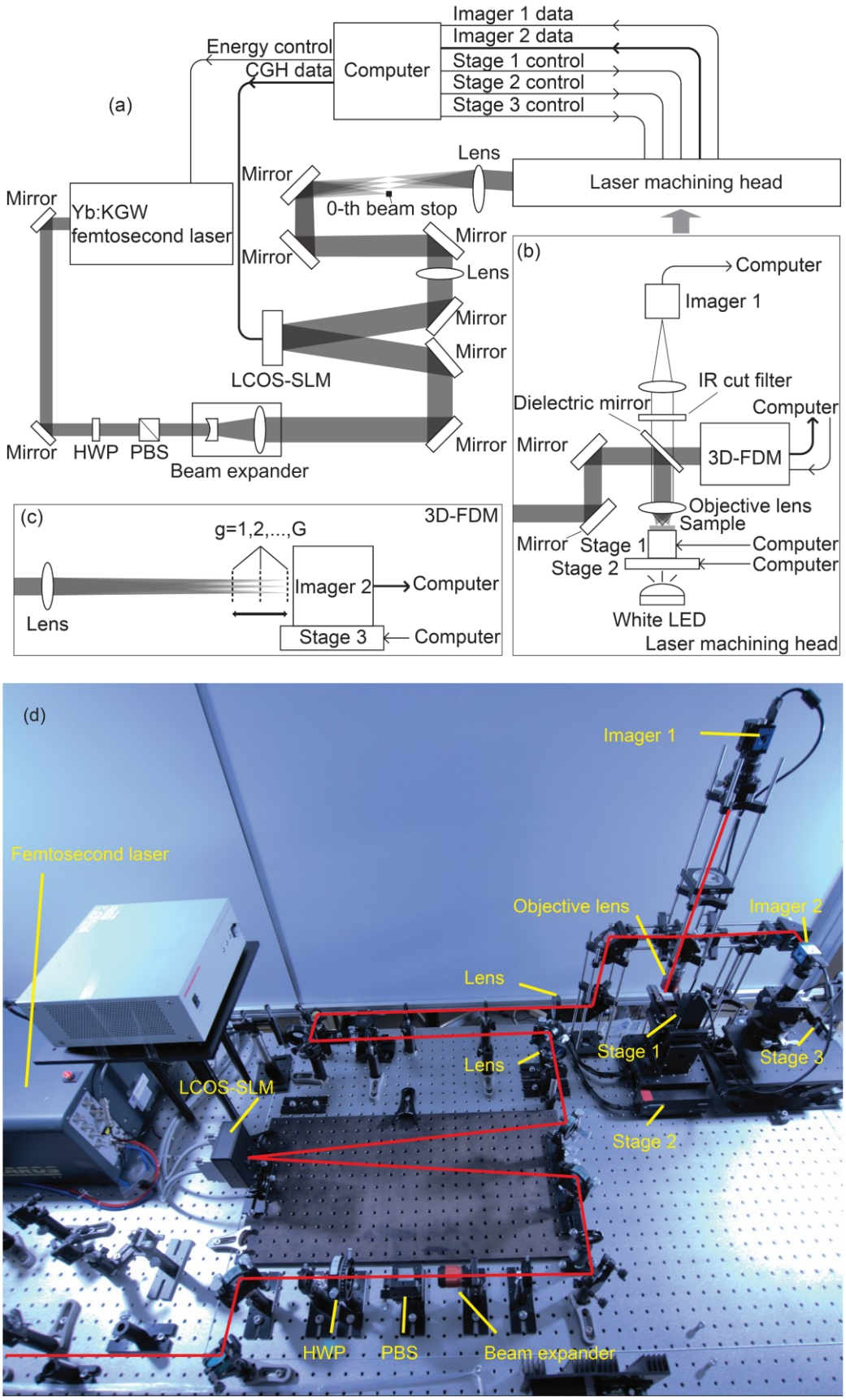

Figure 4.2. (a) Holographic laser processing system with feedback control of 3D parallel focusing, (b) the laser machining head, and (c) 3D-FDM. (d) Appearance of the laser processing system.

Another light arm was then reduced and incident inside a glass sample (MATSUNAMI, microscope slide glass, thickness 0.8~1 mm) by a 50× microscope objective (Mitutoyo, Apo NIR HR) with a numerical aperture of 0.65. In addition, the stage 3, a X-Y linear (Aerotech, ANT95-50-XY-MP) was used to translating the glass sample perpendicular to the axis of the laser pulses. Furthermore, the imager 1 (Imaging Source, DMK33UP1300, CMOS image sensor), a white LED, a z-direction linear stage (THORLABS, MTS25/M-Z8), a lens, and an IR-cut filter were used to monitor the holographic laser processing.

4.4 Observation method of 3D focusing

The most important key points of the implementation in this optimization method are the observation method of the 3D focusing intensities and the recalculation of the CGH from the observation. Here, the observation process will be introduced. Since the optimization is based on the method of moving the CCD image sensor to different focal planes, the capture of the CCD image sensor and the movement of the linear stage should be uniformly scheduled through the computer programming. As the CCD image sensor and the linear stage are programmable, so we can obtain the status information and trace the moving position in real-time. Therefore, as shown in fig. 4.3, the observation process of the 3D focusing intensities can be scheduled in following steps:

(i) firstly, move the linear stage to the specified position, and then return the position information and the signal that the motion has stopped;

(ii) according to the received signals, the computer judges that it is ready for capture at this time, and transmits the capturing command to the CCD image sensor;

(iii) after completing the capturing action, the computer transmits a command to the linear stage to move to the next specified position.

These actions were iterative controlled by the computer to realize an automated, efficient, and high-precision optimization process.

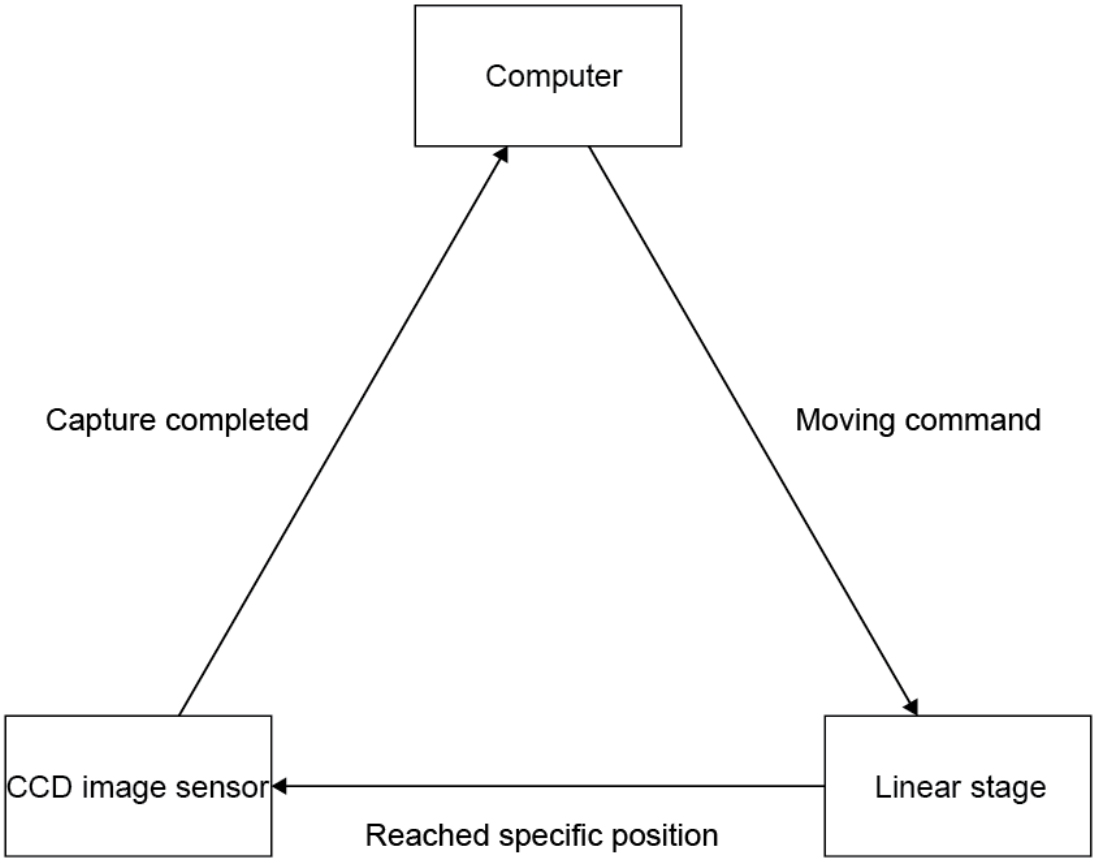

Figure 4.3. Observation method of 3D focusing by controlling the linear stage and the CCD image sensor with computer programming.

4.5 CGH calculation

Figure 4.4 shows a flow chart of the CGH calculation and the uniformity estimation for the 3D parallel focusing. Its completion is mainly based on two algorithm blocks, one is the diffraction calculation (DC) based on the angular spectrum (AS) method [72,73], and the other is the modified version of the weighted iterative Fourier transform (WIFT) algorithm [74,75].

By using the AS method, based on the principle of plane wave superposition transmission, the propagation solution of a three-dimensional spectrum is obtained. The key point in this method is the angular spectrum propagator $H(f_x, f_y)$ as $H(f_x, f_y) =$

$exp\ [\ jkz\sqrt{1-(\lambda f_x)^2-(\lambda f_y)^2}\ ]$. Because this formula includes the z factor along the optical axis, we can control the propagation distance of the angular spectrum by changing the value. Therefore, using the convolution of the spectrum of the object plane and the angular spectrum propagator, the spectrum of the image plane at arbitrary axial position can be calculated. And then the spectrum propagation is completed by the combining the fast Fourier transform (FFT). Also, the discrete diffraction plane with the number of G should be considered. Here, the axial position z was given by the equation $z = z_0 + (g-1) \times \Delta z$, where z_0 is the first plane of the diffraction calculation, Δz is the interval between the diffraction planes, and g ={1, 2, ..., G} is an index of the diffraction planes. In addition, the flow chart here specifies that G is 4 and i is 30.

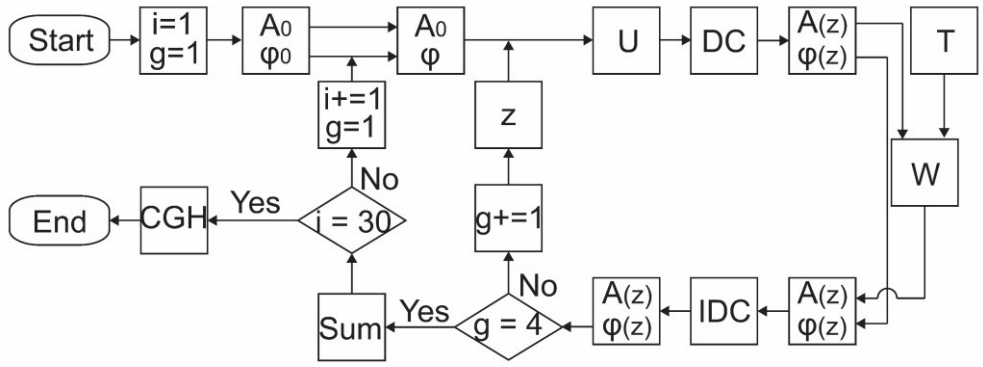

Figure 4.4. Principle of the estimation of the 3D reconstructions and the calculation of the corresponding CGH using AS method and WIFT algorithm. U: complex amplitude; DC: diffraction calculation; A(z): amplitude of z th plane; φ (z): phase of z th plane; T: target intensity; W: weighting operation; IDC: inverse diffraction calculation; g: an index of the diffraction planes; Sum: summation operation of the CGHs in different planes; i: iteration number.

4.6 CGH optimization

The optimization of the CGH is based on the estimation of the corresponding 3D focusing intensity distribution. And it is iteratively performed by using the WIFT algorithm. This process is mainly including the DC, the inverse DC, a weighting operation, and the

synthesis for the CGHs that contained 3D focusing information on different focal planes. The differences between the former WIFT algorithm used in the previous work and the modified version here were the replacement of the simple FFT to the DC and the summation operation of the phase distribution. In addition, the DC was actually performed in the optical system and the IDC and summation were completed in the computer. The weighting operation, represented by the letter 'W' in fig. 4.4, was used to assign different weight values to each spot intensity for the optimization according to the proportion of the target and the measured intensities, for example, the weighting function for the n-th diffraction peak of the g-th diffraction plane was $w(g,n) = [I_t(g,n)/I_m(g,n)]^{\alpha}$, where $I_t(g,n)$ and $I_m(g,n)$ are the target intensity and the measured intensity with an image sensor, denoted by the letter 'T' and 'A', respectively. The synthesis of the CGHs for generating the 3D parallel focusing was performed by the summation operation of the CGHs calculated on the respective diffraction plane, $\{\phi_1, \phi_2, \cdots, \phi_g, \cdots, \phi_G\}$. It was simply calculated as $\phi_{sum} = mod(\phi_1 + \phi_2 + \cdots + \phi_G,\ 2\pi)$.

When the CGH is optimized for uniformizing the parallel focusing beams, the reconstruction was estimated with a uniformity criterion $U_I = I_{min}/I_{max}$, where I_{min} and I_{max} are the minimum and the maximum intensities of all the diffraction peaks, respectively. The feedback control was iteratively performed until a satisfactory uniformity was obtained. Actually, the iteration number can be set according to experimental experience, here, we preset 30 times.

Figure 4.5 indicates an implementation of the 3D focus detection module (3D-FDM). In this figure, the explanation for the case of G = 4 is indicated, and the values used in it are corresponding to them used in the experiments we will indicate in chapter 4. The focusing spot intensities at four diffraction planes, are detected with automatically reciprocating motion of the programmable linear stage controlled by a computer. This direct implementation using the mechanical movement has a low repetition, but is suitable for the first implementation because of no detection error derived from the method. The CGH is displayed on the SLM and then the formed 3D diffraction patterns are detected by the CCD image sensor at four focal positions respectively. The detection of the reconstructions on the respective plane, and recalculation of the CGH, which is iteratively performed based

on the rewritable capability of the SLM.

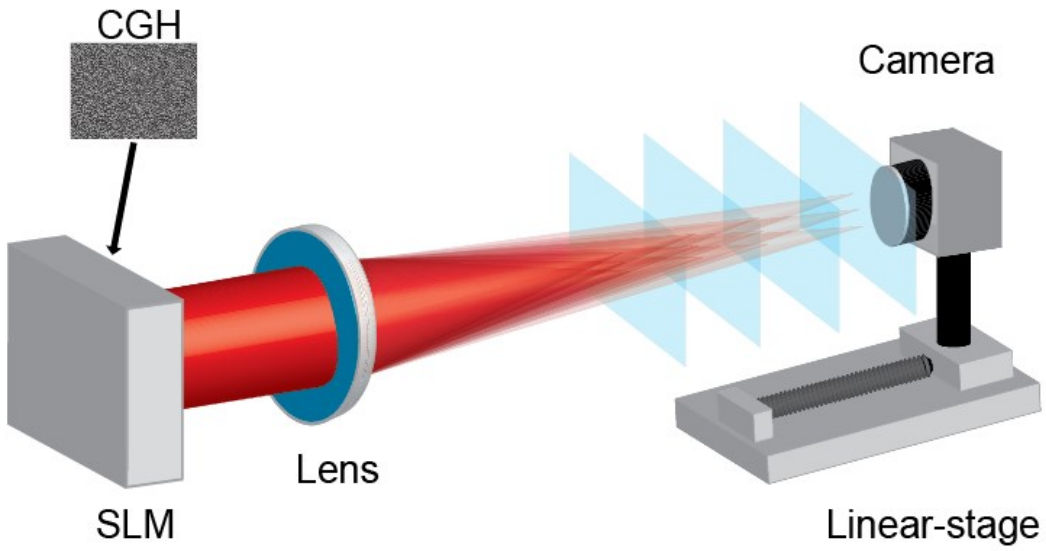

Figure 4.5. 3D focus detection module implemented with a reciprocal movement of a CCD image sensor fixed on the programable linear stage. The CGH generates the parallel focusing on multi diffraction planes along the optical axis.

4.7 Experimental results

The 3D in-system optimization results were obtained by taking use of the optical setup in fig. 4.2.

In order to verify whether the designed CGH containing 3D information can be used for 3D image reconstruction and 3D structure processing in the actual optical system, as shown in fig. 4.6, a verification attempt was conducted. The super-white crown glass was used in this experiment. Figure 4.6 (a) was the designed CGH that contains 3D information of 19 spots; (b) was the simulation image of 19 diffraction spots, the interval between the spots was set to 3 mm; (c) was the observation of the 19 spots by using the laser viewing card at Fourier plane, the focal spot at the far left of the image is furthest from the Fourier

plane and therefore appears to be defocused, while the focal spot at the far right is closest to the Fourier plane and therefore well focused on the plane; (d) was the observation of the ‘snake’ beam was irradiated into a fluorescent liquid, the three lines represent the extension lines of the focal spots distributed along the y axis after irradiating the liquid, and the middle line is the thickest because there were more focal spots in that y coordinate, which means there was more energy; (e) shown the 3D structure processing attempt which was processed inside glass and observed by microscope, 19 spots were successfully processed on different layers of the sample with total energy of 7.79 μJ, and the spacing between the adjacent layers was 3 μm.

Therefore, it was verified that 3D CGH can complete the establishment of 3D optical reconstruction and the processing of 3D structure in the actual optical system.

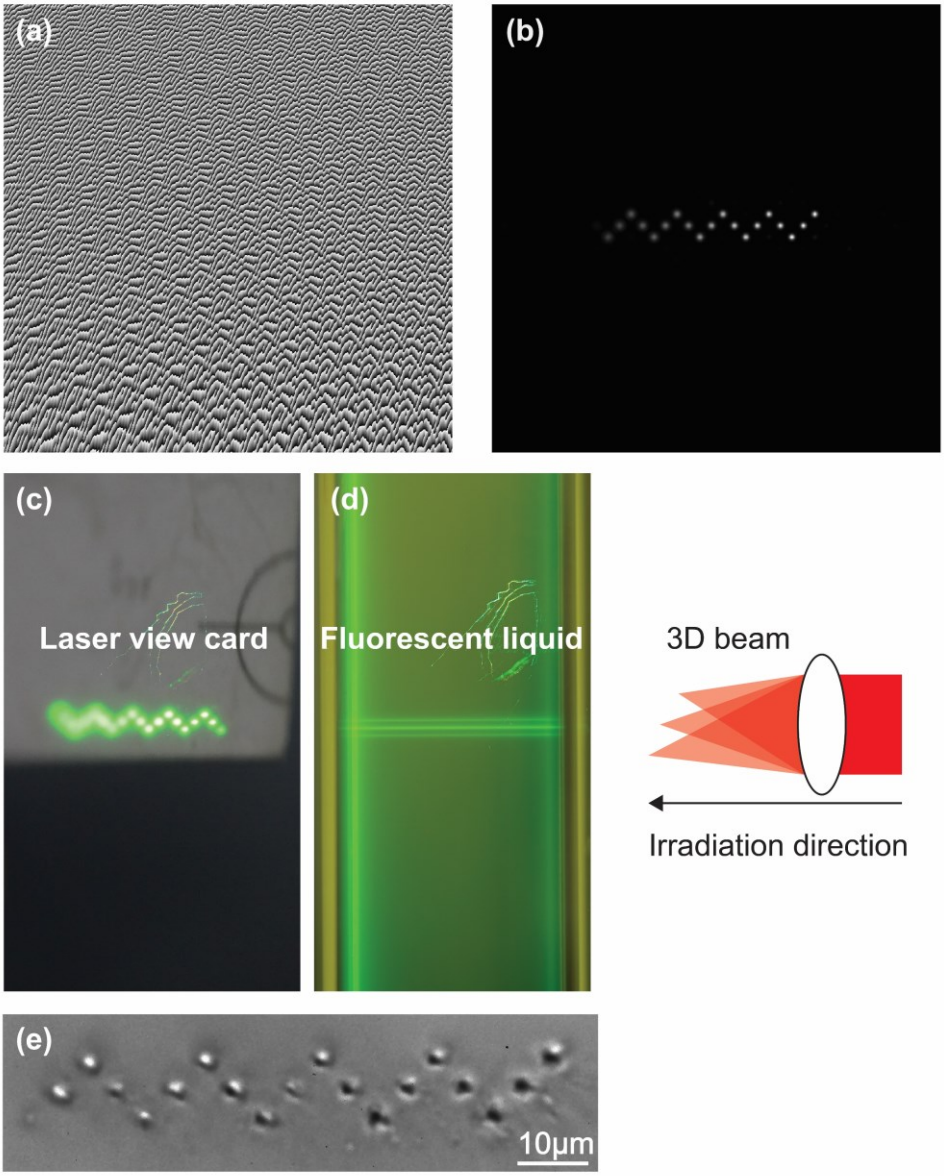

Figure 4.6. Verification of the 3D parallel ‘snake’ beam formation and processing. (a) designed CGH that contains 3D information of 19 spots; (b) simulation image of 19 spots, the interval between the spots was set to 3 mm; (c) observation of the 19 spots by using the laser viewing card at Fourier plane, the focal spot at the far left of the image is furthest from the Fourier plane and therefore appears to be defocused, while the focal spot at the far right is closest to the Fourier plane and therefore well focused on the plane; (d) observation of the ‘snake’ beam was irradiated into a fluorescent liquid, the three lines represent the extension lines of the focal spots distributed along the y axis after irradiating the liquid, and the middle line is the thickest because there were more focal spots in that y coordinate, which means there's more energy; (e) the 3D structure processing attempt which was processed inside glass and observed by microscope, 19 spots were successfully

processed on different layers of the sample, the spacing between the adjacent layers was 3 μm.

Figure 4.7 indicates the identification and calculation sequence of 3D diffraction spots by moving the CCD image sensor to different focal planes using a linear stage according to the method discussed in section 4.4, in this case totally 40 spots at four planes. It is very important to give the diffraction spots order due to the optimization process was to assign different weight values to different light intensity distribution, and these sequence numbers will follow the corresponding diffraction spots until the optimization is complete. (a) the seven spots in the letter 'C' were given numeric numbers from 0 to 6; (b) ten spots in letter ‘O’ were given numeric numbers from 7 to 16; (c) twelve spots in letter ‘R’ were given numeric numbers from 17 to 28; and (d) eleven spots in letter ‘E’ were given numeric numbers from 29 to 39.

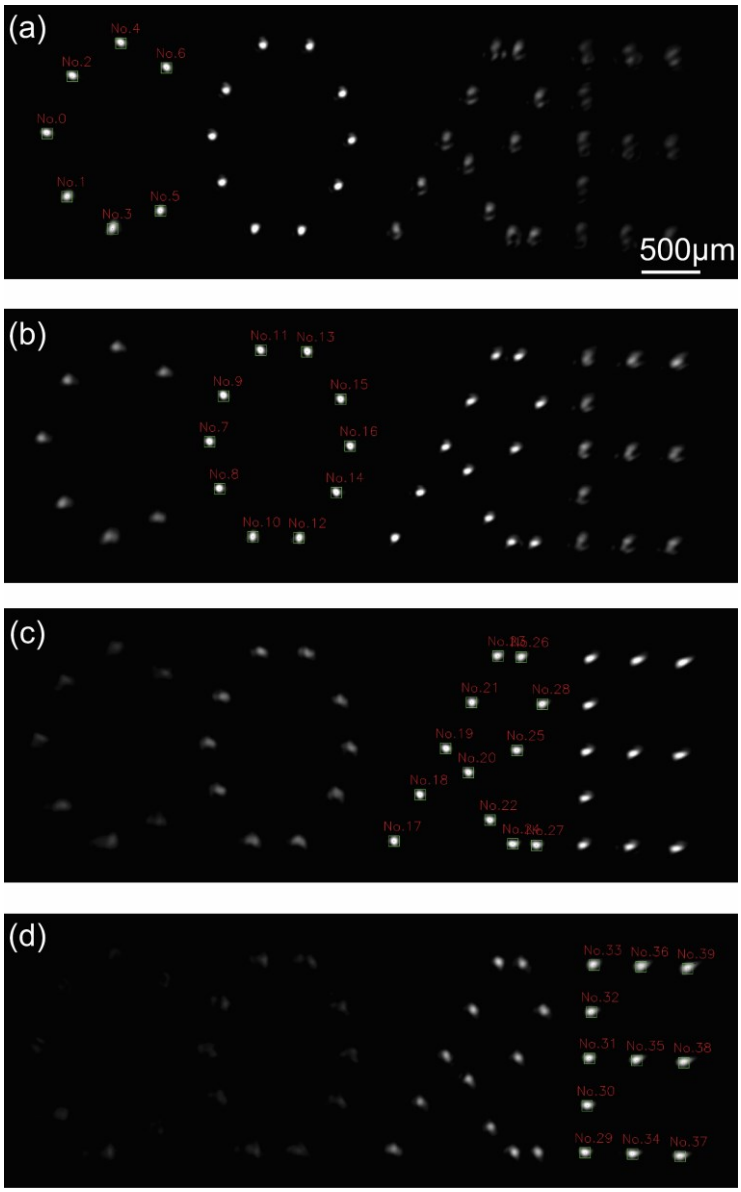

Figure 4.7. Identification and calculation sequence of 3D diffraction spots by moving the CCD image sensor to different focal planes, in this case totally 40 spots in four planes. (a) seven spots in the letter 'C' were given numeric numbers from 0 to 6; (b) ten spots in letter ‘O’ were given numeric numbers from 7 to 16; (c) twelve spots in letter ‘R’ were given numeric numbers from 17 to 28; and (d) eleven spots in letter ‘E’ were given numeric numbers from 29 to 39.

Figure 4.8 shows the experimental optimization results of 40 diffraction spots with feedback control: (a) the optimized optical 3D reconstructions; (b) the intensities of the 40 diffraction spots, and the corresponding uniformity (U) curve. In fig (a), there are three optimization order of 1st, 5th, and 30th iteration that are pointed to the row with black arrows.

And the optimized reconstructions detected by the imager at focal positions of 206 mm, 212 mm, 218 mm, and 224 mm were shown in each order that are pointed to the column with colorful arrows, according to the letter ‘C’, ‘O’, ‘R’, ‘E’. The diameter of the diffraction spots was 76.56 μm on the imager plane. In addition, the diffraction efficiency obtained by dividing the diffracted beam energy by total energy including zero-order was 71.0%. The intensity curves of the 40 diffraction spots represented the ‘CORE’ are shown in red lines, blue lines, green lines, and orange lines, respectively. From the direction of intensity curves, it can be seen that they were very different at the beginning of optimization. However, with the progress of optimization, they were gradually homogenized to a unified value. And the U curve shown in the black dotted line was improved from the initial value of 0.13 to a maximum value of 0.96 within 30 iterations. The total time consumption for the 30 iterations was 471.9 seconds, that is 15.73 seconds for each iteration, which included the moving time of the linear stage (9.29 seconds), the capturing time of the CCD image sensor (0.08 seconds), the response time of the LCOS-SLM (0.26 seconds), the FFT calculation time (4.14 seconds), the image processing operations (0.88 seconds), and some other signal processing operations in the computer (1.08 seconds). If we can use a high-speed stage (e.g., Aerotech, ANT95-50-XY-MP) to replace the stage we are using now, accompany with a high-frame-rate imager (e.g., Imaging Source, DMK33UP1300) and LCOS-SLM (e.g., Meadowlark Optics, HSP1920-500-1200-HSP8), and a high-performance GPU hardware (e.g., GeForce, GTX 1660 SUPERTM OC 6 G), the optimization speeding-up in future work for the quantitative estimation may be controlled within 1 s to satisfy the actual industrial produce needs.

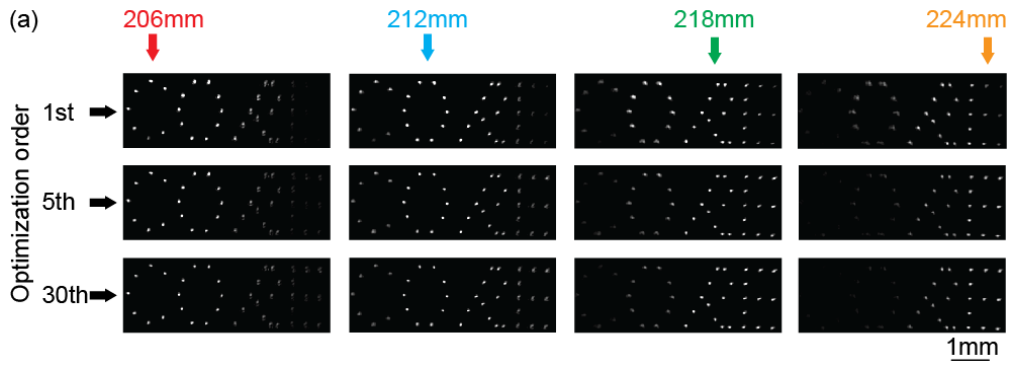

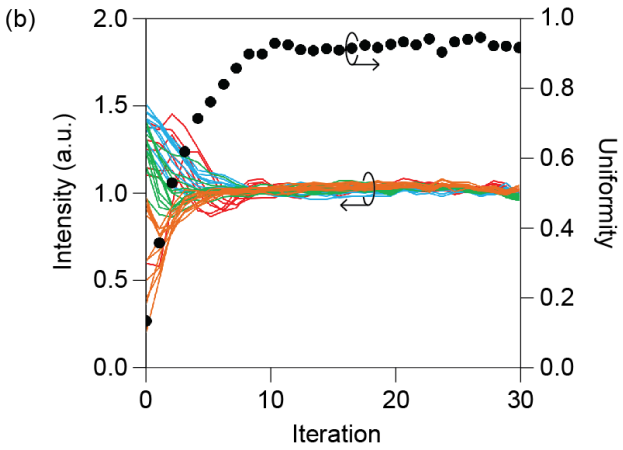

Figure 4.8. The variation of the spot intensity and the uniformity of feedback control for 40 diffraction spots, including the optimized optical reconstructions, the temporal intensities of the 40 diffraction spots and the U curve. Here, the red lines, the blue lines, the green lines and the orange lines represent the intensities of the first focal plane, the second focal plane, the third focal plane and the fourth focal plane, respectively. The U curve shown in the black dotted line indicates the trend of uniformity changes within 30 iterations.

Figure 4.9 shows: (a) 3D holographic laser fabrication of 40 parallel micro-holes irradiated vertically at four different depths along the optical axis direction inside a glass sample while applying feedback control of the CGH of 1st, 5th, and 30th fabrication orders; (b) the enlarged images of the fabricated area for easily recognizing the changes from 1st to 30th fabrication orders. The total pulse energy of the 40 focal spots was 17.82 μJ on the sample (super-white crown glass), and so the average energy of each spot was 0.45 μJ, which was a little higher than the fabrication threshold of 0.30 μJ. Here, the energy setting was according to the measurement results of the processing threshold before the optimization process. The threshold was defined of the minimum total energy just to process 40 micro-holes at the same time inside the glass sample. In this experiment, we set the energy to be slightly higher than the threshold to ensure the energy is enough to allow the 40 holes can be processed. Therefore, the difference in the size of the holes will only result from the uneven distribution of the total energy. This uneven distribution will lead to the size of some holes being less than the average level, or even lower than the threshold that results in it cannot be processed on the sample material, and in contrast, some holes will be processed into larger sizes. It can be seen from the fabrication result

that, as the paralleled focused beams gradually be uniformized, the sizes of the 40 processed micro-holes also tended to become more consistent. The micro-holes shown in the red boxes, the blue boxes, the green boxes, and the orange boxes represent the fabrication areas at the four different depths, respectively. In addition, the spacing between the depth planes was 2.40 μm. The rows in the figure represent the fabrication order according to the 1st, 5th, and 30th iteration order of the CGH optimization, respectively. As can be seen from the 1st order, the greater intensity at the 1st and 2nd depths led to larger micro-holes than at the 4th depth, and there were some cracks surrounding the holes; consequently, some micro-holes at the top-right were not processed at the 4th depth. Then, at the 5th fabrication, the sizes of all the micro-holes became more uniform due to the better uniformity, which was improved from 0.13 to 0.71 because of the reduced beam intensities at the 1st and 2nd depths and the increased beam intensities at the 4th depth. And at the 30th fabrication attempt, the sizes of all the micro-holes were roughly uniformized from the observation of the microscope system, in addition, the shape present clean edges without tiny cracks.

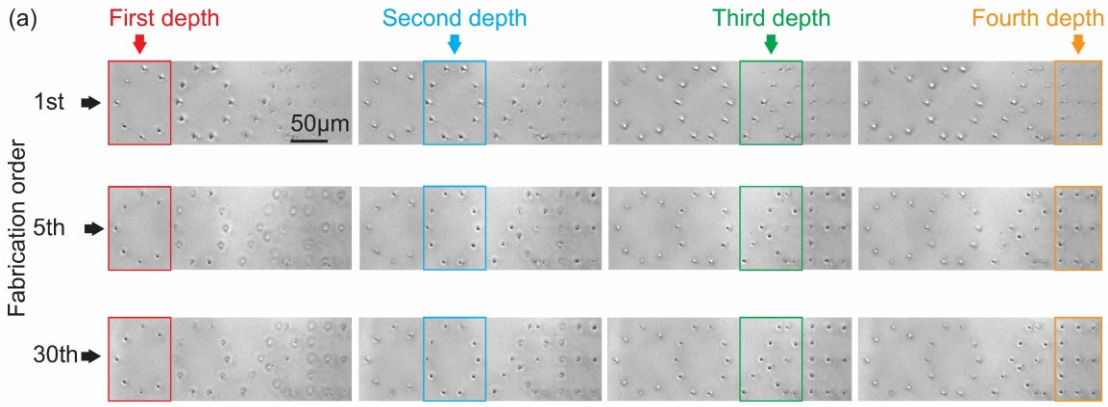

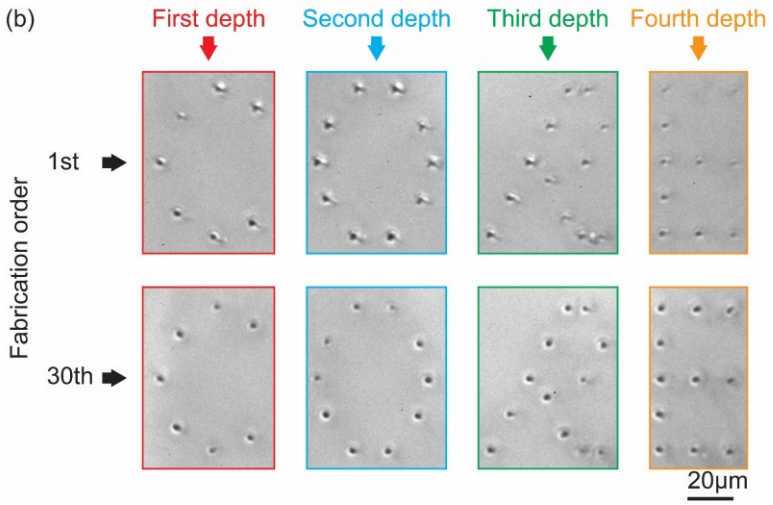

Figure 4.9. 3D holographic processing result: (a) 40 parallel micro-holes were simultaneously irradiated at four different depths inside the glass sample with a single laser shot, while applying feedback control of the 3D parallel focusing; (b) the enlarged images of the fabricated area for easily recognizing the changes from 1st to 30th fabrication orders.

4.8 Summary

In this chapter, based on the method mentioned in 2D case, a more practical 3D CGH is designed and optimized. The key points of the implementation of feedback control for the 3D focusing is described, including the observation method of 3D focusing intensities and a recalculation of the CGH from the observation. In section 4.2, from the perspective of concept and principle, the feasibility of 3D focusing detection and optimization under the combination of computer and optics is explained in detail. This iterative method is not only innovative, but also provides a reliable guarantee for high-quality 3D focusing. In section 4.3, relying on the programmable linear stage and the unified control of the computer, the automatic recognition and detection of 3D focusing are realized. This simple and direct implementation method can avoid the detection and calculation errors of complex systems to a great extent. In section 4.4, the specific steps of automatic light spot information acquisition are illustrated. In addition, for different 3D distributions, the corresponding

feedback control can be realized by adjusting a series of parameters such as computer program, moving distance of the stage, response time of the imager, etc. In section 4.5, based on the AS method, the spectral propagation of different focal planes is realized, and the spectra of these planes are linearly superimposed to obtain the CGH containing 3D information. In section 4.6, according to the WIFT algorithm, after collecting all the 3D focusing information, the light intensities are optimized according to the evaluation function, so as to achieve the ultimate goal of optimizing the CGH. Different from the 2D case, the 3D distribution needs to calculate all the planes of focusing, so the computational cost and iteration time will increase. In section 4.7, the experimental results verify the effectiveness of the feedback control method for the 3D focusing. It includes the optimization of four-layer 3D focusing, which are expressed as letters ‘C’, ‘O’, ‘R’, and ‘E’ respectively, and the uniformity of 40 focusing spots is optimized from 13% to 96%. Moreover, it also can be seen from the comparison of 3D holographic processing results before and after CGH optimization, as strong evidence of the improvement, the possibility of this method for industrial use is proved.

Chapter 5: Application of in-system optimization for 3D holographic grooving

5.1 Introduction

In this chapter, the application of in-system optimization for 3D holographic grooving will be demonstrated. From concept to actual operation, each experiment step is well planned and arranged in detail, and then the advantages and disadvantages of this method will be verified and analyzed from the comparison experiment results. In section 5.2, the concept of 3D holographic laser grooving will be summarized. And the examination about the performance of this application is determined, due to some factors that will have an influence on the grooving, such as the energy allocation or the spatial distribution of the 3D beam. In section 5.3, an optical setup for observing the processing of 3D beams inside the glass sample will be shown. Through the observation, the interaction mechanism between 3D focusing and sample can be intuitively understood, and it also can provide a basis for further research on laser grooving. In section 5.4, in order to verify the advantages of 3D focusing compared with conventional single point focusing in laser grooving, CGHs with different 3D distributions are designed, and they will be evaluated from two aspects of groove depth and width. And we will also explore how to increase the groove depth by using different 3D holographic beams. In section 5.5, the experimental results of 3D holographic laser glass grooving observed with FE-SEM will be displayed, and the characteristics of this application will be analyzed, evaluated, and discussed with the data curves. In section 5.6, a summary of this chapter will be denoted.

5.2 Concept

Figure 5.1 shows the concept of the 3D holographic glass grooving. Based on the technology of holographic laser processing with the CGH that generates 3D focusing, a method is proposed that combines the multi-beam irradiation of the sample and the lateral scanning by a linear stage, the 3D holographic glass grooving can be realized. In this method, the key point is the performance of the irradiation from 3D holographic parallel beams to the inside of the glass sample. We need to first explore what the 3D beams look like after irradiating inside the glass. Then to compare what are the differences with the traditional single-point laser processing, and according to the processing characteristics to carry out the next adjustment, such as increasing the interval between the adjacent 3D spots can expand the processing depth, or distributing different energies to complete the processing according to the different depths.

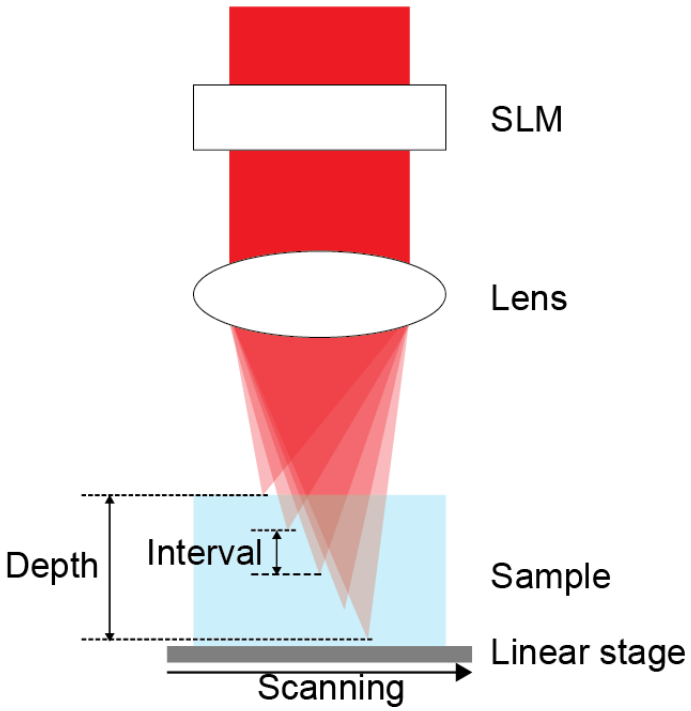

Figure 5.1. Concept of the 3D holographic glass grooving.

5.3 Optical setup

Figure 5.2 shows the setup using for 3D holographic glass inside grooving side observation. A femtosecond laser pulse was emitted from an amplified Ti: sapphire laser source (COHERENT, Micra and Legend Elite), with a center wavelength of 800 nm, a spectral width of 30 nm (full width at half-maximum (FWHM)), a pulse duration of ~50 fs, and a repetition frequency of 1 kHz. A set of a half wave plate (HWP) and a polarized beam splitter (PBS) were used to control the pulse energy. Then the pulse was collimated by a 2 × beam expanding optics composed of a concave lens and a convex lens. The collimated beam had an irradiation on a liquid-crystal-on-silicon SLM (LCOS-SLM; Hamamatsu Photonics, X10468-02) for the spatial light modulation by the pre-designed CGH.

The 3D shaped pattern was reduced by an objective lens 1 (OL1, OPTOSIGMA, ELWD Plan), with a magnification of 50 × and a numerical aperture (NA) of 0.55, inside the glass sample (fused-silica, thickness 26 mm × 5 mm × 1 mm). The glass sample was fixed on a three-axis linear motor stage (Thorlabs, ZFS13B).

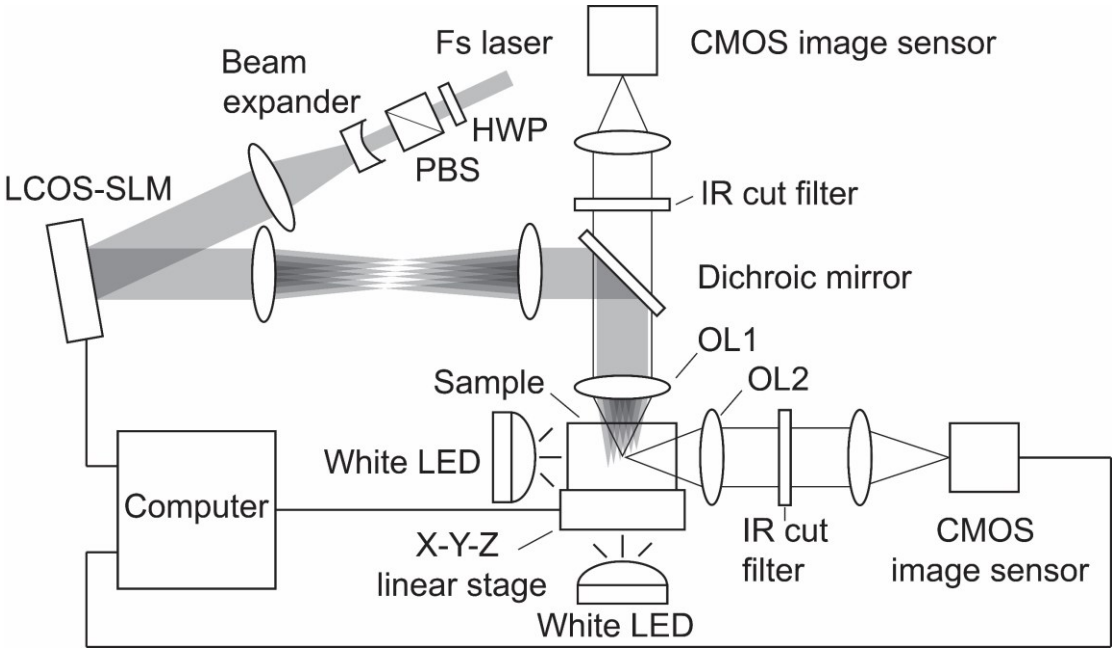

Figure 5.2. Setup of the 3D holographic glass inside grooving side observation.

The 3D holographic glass grooving was monitored from the top and side view with two

microscope systems. One was consisted of a white light emitting diode (LED), the OL1, a dichroic mirror (Thorlabs, DMPS638), an infrared (IR) cut filter, and a complementary metal oxide semiconductor (CMOS) image sensor (IMAGINGSOURCE, DMK33UP2000), with 1920 × 1200 pixels, each pixel has a size of 4.8 μm × 4.8 μm, 10-bit A/D conversion, and a framerate of 129 fps. Another one was consisted of a white LED, an object lens 2 (OL2, MITUTOYO, M Plan Apo) with a magnification of 20 × and a numerical aperture of 0.42, an IR cut filter, and a CMOS image sensor (IMAGINGSOURCE, DMK33UP2000).

The computer was used to control the actions in the system, such as the CGH displaying on the SLM, the linear stage moving, and the image sensor capturing.

5.4 Grooving depth and width investigation with different 3D patterns

In order to verify the advantages of 3D beams over single beam in grooving, it is necessary to quantitatively evaluate the groove depth and width. And the curves of the two data are drawn under different laser intensities. In order to make the comparison data more convincing, we use different three-dimensional patterns for verification, as shown in the fig. 5.3: (a) 1 point grooving on material surface; (b) 3 points in tilt arrange grooving from surface to inside; (c) 5 points in tilt arrange grooving from surface to inside; (d) 10 points in tilt arrange grooving from surface to inside. Here, we take use of the setup shown in fig. 4.2 to complete the holographic grooving. In addition, the position of 1-point grooving is consistent with the position of the point to the glass surface during multi-point processing.

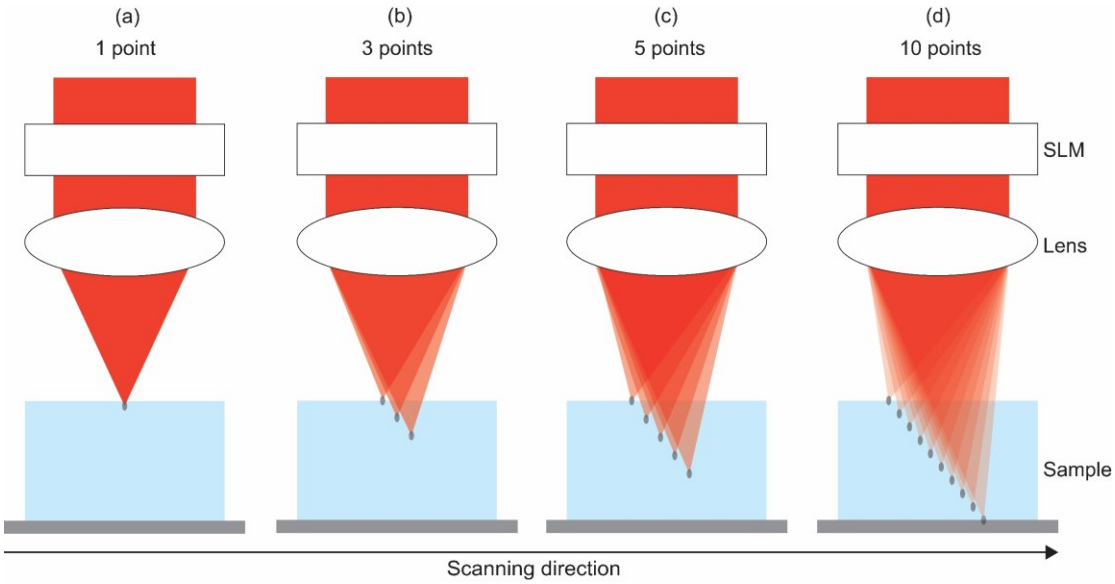

Figure 5.3. Grooving depth and width investigation with four different patterns: (a) 1 point grooving on material surface; (b) 3 points in tilt arrange grooving from surface to inside; (c) 5 points in tilt arrange grooving from surface to inside; (d) 10 points in tilt arrange grooving from surface to inside.

Figure 5.4 shows the scanning properties test of the three-axis linear stage, including the data curves for a period of 3s: (a) time required for velocity to reach the preset value, and (b) time required for acceleration. This test is to verify whether the moving speed of the linear stage has an impact on the grooving, such as pulse energy overlap or accumulation. Here, we preset 10 mm/s as the target value of the speed, because the repetition frequency of the laser used here is 1 kHz, which can ensure that the spacing between each two adjacent pulse processing points is 10 μm. Of course, if we change to a higher frequency laser source, such as 10kHz, it can also ensure that the spacing is 1 μm, that is, the processing points are independent of each other. During acceleration, it takes 39ms for the velocity to reach the default and 21ms for the acceleration to reach the maximum operating power. During deceleration, it takes 21ms for the velocity to decrease from the default to zero, and 9ms for the deceleration to reach the maximum operating power. It can be seen from the data that the velocity change time is 60ms, accounting for only 2% of the overall period 3s, so it has no impact on the overall grooving.

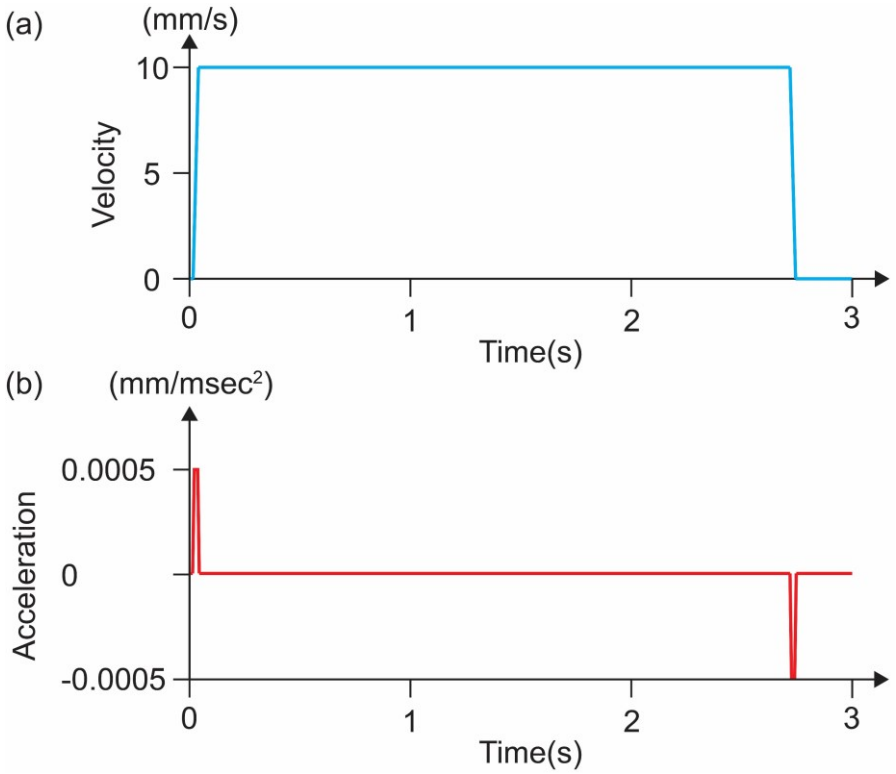

Figure 5.4. Scanning properties test of the linear stage: time consumption of the velocity and acceleration.

Also, the grooving depth can be expanded by adjusting the interval between the 3D points, as shown in fig. 5.5: (a) 10 points are pre-designed in small interval; (b) 10 points are pre-designed in large interval. And they have the same spacing in the transverse distribution.

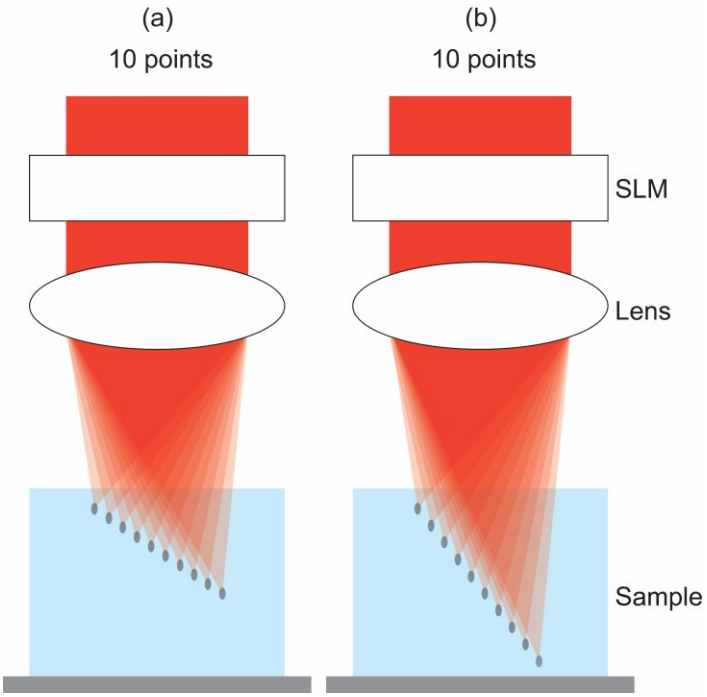

Figure 5.5. Verification of the feasibility for expanding the grooving depth by using 3D patterns in different intervals.

5.5 Experimental results

Micro groove processing

The 3D holographic glass grooving results were obtained by taking use of the optical setup in fig. 4.2.

Figure 5.6 shows the micro grooves processing experimental results with 1-point, 3-points, 5-points, and 10-points beams in the same total energy of 13.75 μJ, and the points was arranged in tile refer to the fig. 5.3. This experiment was completed by using the optical setup shown in fig. 4.2, and the super-white crown glass sample was used. The groove line was processed by scanning the glass sample in a lateral direction with the linear stage at a speed of 10 mm/s.

In order to observe the depth and width of the microgroove, the sample was broken along the direction perpendicular to the groove line with a glass cutter. And the observed

results of the surface and the cross-section were explained in fig. 5.7.

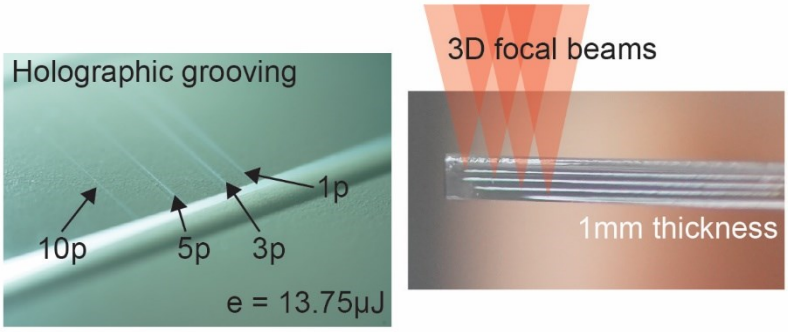

Figure 5.6. Grooves processing with 1-point, 3-points, 5-points, and 10-points beams in the same total energy of 13.75 μJ, and the points was arranged in tile refer to the fig. 5.3. These pictures were captured by using a digital camera (Sony, α 7 III).

Figure 5.7 shows the part of the results with respect to the width and depth of the grooves correspond to the beams shown in fig. 5.3. The surface and cross-section were observed by a field-emission scanning electron microscope (FE-SEM) (Hitachi, S-4500). And we believe that this is the first time to observe from the side under FE-SEM based on holographic three-dimensional grooving technology. In this experiment, the measurement of depth and width was based on the premise that the beams were in the same total energy, and the processing position was from the surface of the glass sample.

It can be intuitively seen from the processing results that both single-point grooving and three-dimensional grooving have in common that the groove depth and width increase with the increase of the pulse energy. And according to the different beam distribution, there is a difference between the initial threshold and the upper threshold of processing energy. The allowable pulse energy range of single-point processing is 0.8 μJ ~ 5.1 μJ, the range of 3-points is 3.5 μJ ~ 16.1 μJ, the range of 5-points is 7.5 μJ ~ 29.8 μJ, and the range of 10-points is 2.3 μJ ~ 45.2 μJ. The initial threshold here refers to the pulse energy that can just be used for grooving on the surface of the glass sample, and the upper threshold refers to the upper limit light intensity that can be applied by the beam when there are obvious cracks around the groove in this experiment.

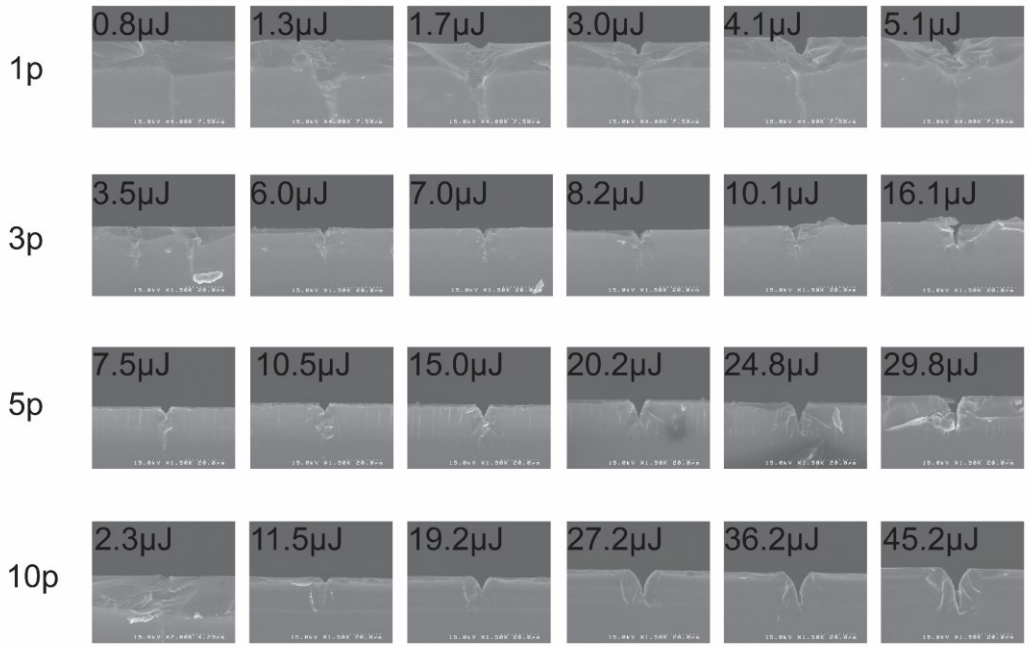

Figure 5.7. Comparison of the results with respect to the width and depth of the grooves correspond to the beams shown in fig. 5.3. The surface and cross-section were observed by a field-emission scanning electron microscope (FE-SEM) (Hitachi, S-4500).

Figure 5.8 shows the curves of the measured data of the grooving: (a) the depth data; (b) the width data, according to the above four different holographic beams. 1-point results are represented by black circle, 3-points results are represented by red triangular, 5-points results are represented by blue diamond, and 10-points results are represented by green square. The summary of the measurement data here are based on the images of the FE-SEM and the corresponding magnification scale.

From the comparison of data curves, it can be verified that they all have the commonness that the depth and width will increase with the increase of energy. In fig. 5.8 (a), the curve of 1-point, 3-points, 5-points, and 10-points described with black circles, red triangular, blue diamond and green square, shown the maximum grooving depth is 3.5 μm, 12.4 μm, 17.0 μm, and 21.8 μm, respectively, within their allowable pulse energy range

talked above. Compared with a single point, 3D beam distribution not only has a larger allowable energy range, but also can realize deeper grooving depends on that range. We note that the general trend of all curves is approximately linear, but the initial processing threshold of 10 points is slightly lower than 3 points and 5 points, which may be because the nonlinear absorption of the material will be more obvious with the increase of the number of 3D beams. In addition, the 5-points grooving depth gradually exceeds the maximum depth of 3-points after the energy value of 20 μJ, and the 10-points grooving depth gradually exceeds the maximum depth of 5-points after the energy value of 30 μJ. From these two results, it can be concluded that due to the existence of aberration, the focused beam energy will decay with the increase of depth. Therefore, it is necessary to compensate the aberration of the focused beam inside the material for holographic laser groove processing.

In fig. 5.8 (b), the maximum grooving width of 1-point, 3-points, 5-points, and 10-points are 6.8 μm, 8.9 μm, 14.3 μm, and 16.1 μm, respectively. It can be seen from the results that the grooving width of 1-point exceeds the grooving width of all of the 3D beams within its allowable energy range, however the grooving depth of 1-point is smaller than the others. This is considered the advantage of the holographic 3D grooving for the high-precision machining, material cutting, and special shape processing, etc. In addition, some of the width curves of the 3D beams are almost overlapped, which show that the width of the grooving not only increases with the increase of energy, but also is related to the spot that first contacts the material surface in the 3D beam distribution.

Therefore, based on the above analysis, the relationship between 3D patterns design for 3D grooving, spots energy allocation, and aberration analysis at different depths inside the material need to be further investigated.

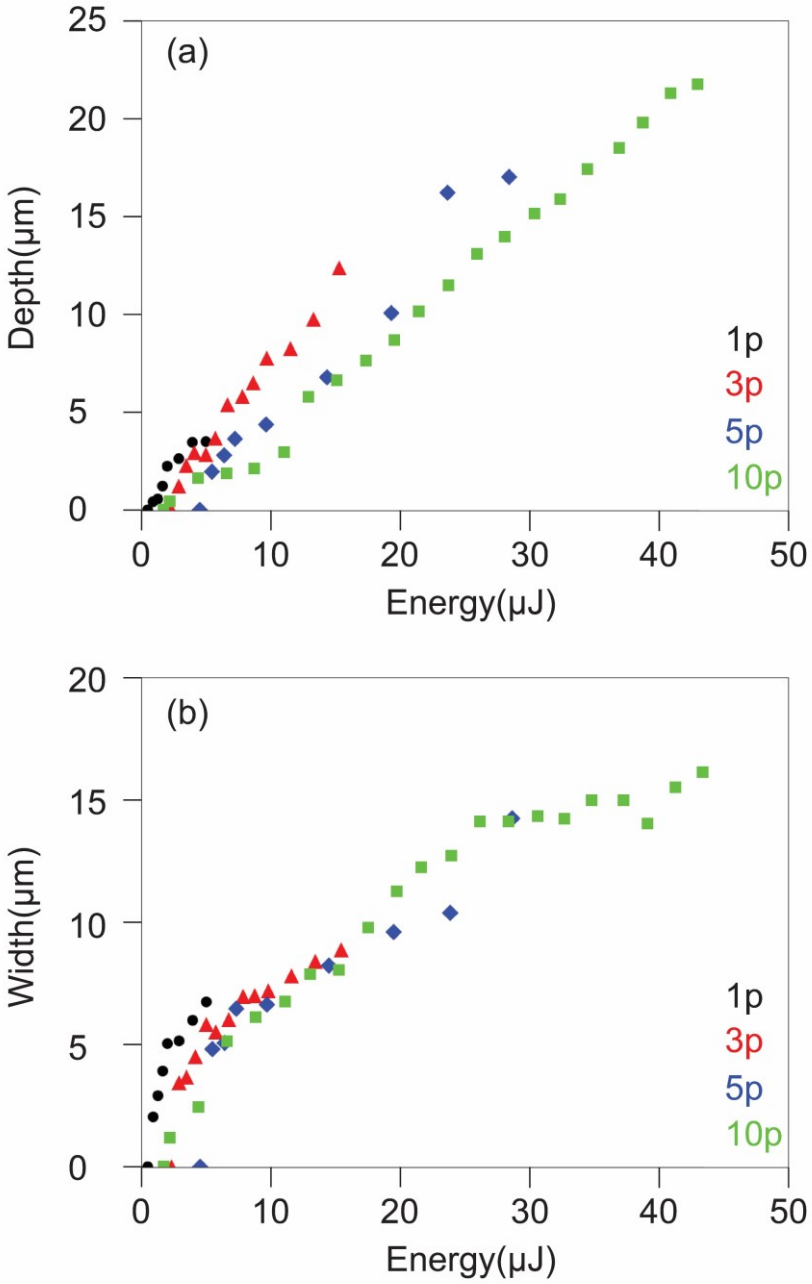

Figure 5.8. The depth and width data of the grooving respectively, according to the above four different holographic beams. 1-point results are represented by black dotted lines, 3-points results are represented by orange triangular lines, 5-points results are represented by gray diamond lines, and 10-points results are represented by yellow square lines.

Side view observation results

These side view observation experimental results were obtained by using the setup

and patterns shown in fig. 5.2. and fig. 5.5.

Figure 5.9 shown the processing depth expansion results by using different 3D patterns with broadening intervals between the adjacent focus. (a) pattern 1, the 3D CGH with spot interval of 6 μm; (b) pattern 2, the 3D CGH with spot interval of 12 μm; (c) single shot inside the glass with the pattern 1; (d) single shot inside the glass with the pattern 2; (e) scanning process result of the pattern 1; (f) scanning process result of the pattern 2.

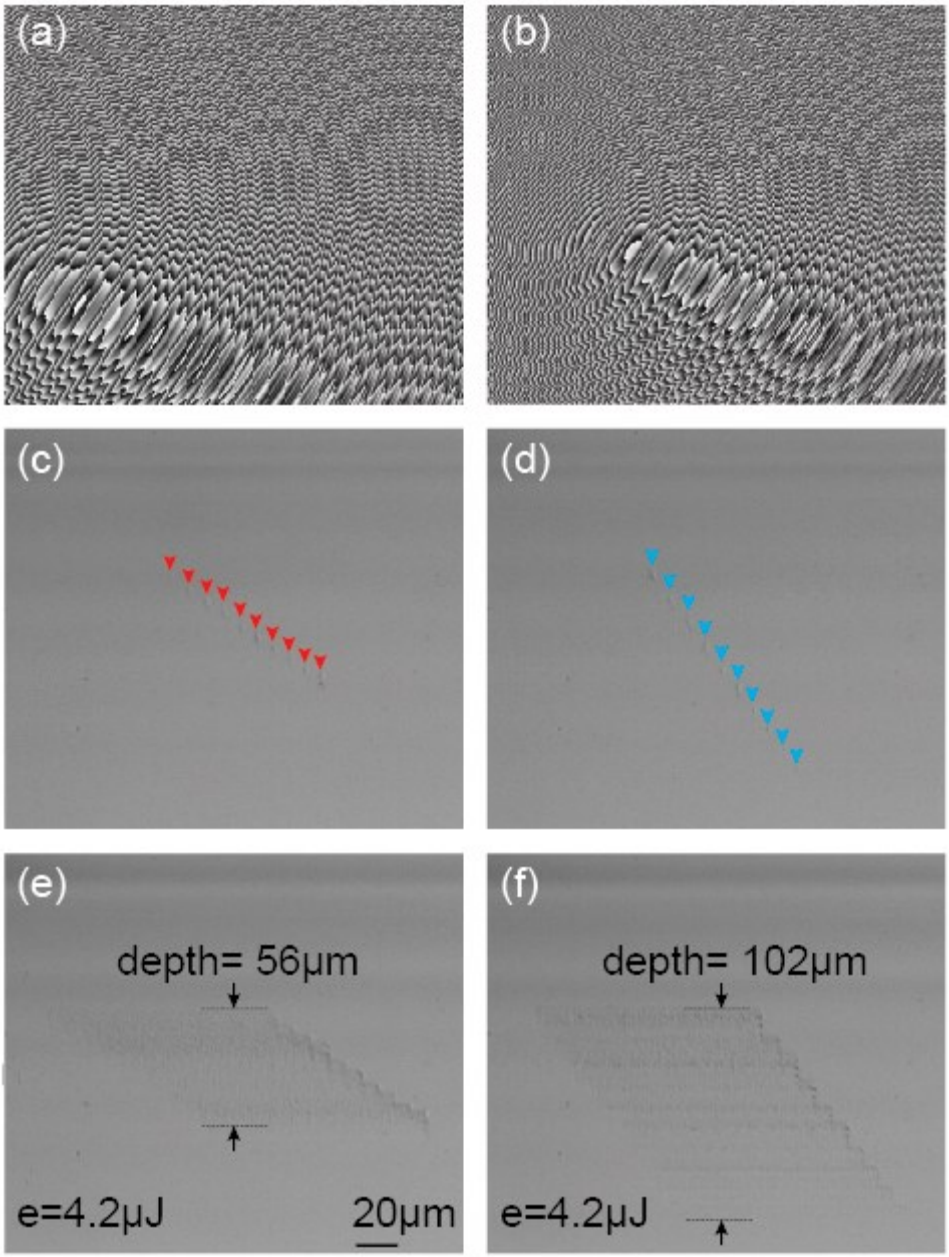

Figure 5.9. Processing depth expansion by using different 3D patterns with broadening intervals between the adjacent focus. (a) pattern 1, the 3D CGH with spot interval of 6 μm; (b) pattern 2, the

3D CGH with spot interval of 12 μm; (c) single shot inside the glass with the pattern 1; (d) single shot inside the glass with the pattern 2; (e) scanning process result of the pattern 1; (f) scanning process result of the pattern 2.

It can be seen from the comparison of the fig. 5.9 (c) and (d) that we can realize the expansion of the grooving depth by adjusting the spacing between the layers in the 3D beams. Here, the red and blue arrows indicate the processing marks when irradiating the interior of the glass with single-shot. Moreover, it can be seen from (e) and (f) that the processing traces after scanning verify the feasibility of the method of groove depth expansion. In addition, the deeper the beam focused into the glass, the shallower the processing trace, which is due to the attenuation of focusing energy due to nonlinear absorption and aberration.

5.6 Summary

In this chapter, an application of 3D holographic glass grooving is proposed. And with the analysis of the experimental results, it is proved that the 3D holographic beams have obvious advantages over the single beam in the laser grooving. Consequently, it shows that the 3D holographic glass grooving method is feasible and will receive widespread attention in the future. In section 5.2, the concept of 3D holographic grooving is well explained, it is based on the method of 3D laser processing we proposed in previous work. And this concept shows the key point is the performance of the laser irradiation phenomenon according to the pulse energy and the 3D distributions. In section 5.3, the side view of the 3D inside glass grooving is realized. From the side observation, the basic phenomenon can be confirmed that the pulse energy will be decay as deeper inside the glass. In section 5.4, different 3D patterns are designed, including 1-point, 3-points, 5-points, and 10-points. They are used to research the advantages of the 3D beam compared to the single-point case. Also, there are two types of patterns of 10-points are designed in this section, they are used to verify the possibility of grooving depth expanding by adjusting the interval between multi-layers. In section 5.5, based on the principle and preparation mentioned above, the experimental results are obtained. From the results, it can be concluded that regardless of single-point or 3D focusing, their grooving depth and width will increase with the increase of energy. However, 3D focusing can achieve a greater energy allowable grooving depth without causing cracks in the surrounding material. Moreover, the grooving width of 3D focusing is generally smaller than that of single-point,

which is conducive to better performance in high-precision machining applications. In addition, the side view results shows that it is possible to expand the grooving depth arbitrary by changing the 3D distribution inside the material. Therefore, this method also provides the possibility of free transformation of grooving depth for many precise applications.

Chapter 6: Conclusion

General discussion

This thesis aims to obtain the high-precision and high-stability holographic femtosecond laser processing, and studies the optimization technology of CGH. Therefore, starting from the optimization technology of the CGH, the research and discussion of the in-system optimization technology are launched.

The first chapter focuses on the background research of holographic femtosecond laser processing. From the existing problems, it analyzes the key factor in the technology, that is, the necessity of the optimization of the CGH, so as to clarify the research theme and launch the theoretical and experimental verification process.

In the second chapter, from the perspective of the development history of the CGH, the origin and development experience of the CGH are discussed. It is clear that the type of the CGH currently used belongs to the phase-only hologram. Under the premise of obtaining a phase modulation mechanism with high diffraction efficiency, obtaining high-quality and high-uniform light intensity distribution is the main target. Various optimization methods have been classified and sorted. And clarified the position and necessity of this research, leading to the theme of this article, namely, the technology of in-system optimization of the CGH.

In the third chapter, it focuses on the implementations of the in-system optimization of the CGH in 2D case, which provides a theoretical basis for the subsequent experimental verification process. In addition, it mainly consists of the calculation methods of the 2D CGH, the evaluation of the uniformity of the optical reconstructions, the stability test of the performance of the method by introducing perturbations. And the experimental results are used as an effective support for the above theoretical methods.

In the fourth chapter, it proposed a method to realize the feedback control of 3D

focusing. This realization is based on the foundation of the 2D case, and combining the AS method. Successfully implemented the automatic observation of the 3D focusing and recalculation of the corresponding CGH from the observation. Whether the optimization results of the optical reconstructions or the micro-holes processing, comparing the effect before and after the optimization, are evidence of the effectiveness of this method.

In the fifth chapter, the application of 3D holographic glass grooving is demonstrated, which is based on the methods of previous work. The experimental results of the grooving verify the feasibility of the application. It allows freeform processing by designing different 3D patterns according to the demand or the material. Also, it can be further applied to many industrial uses like glass cutting, waveguide writing, or other optical processing.

This research, as a frontier subject in the field of laser processing, it has outstanding advantages and a guiding role in the development of new technologies. And can be widely used in the field of precision laser processing to provide higher stability, precision, and flexibility for laser processing systems. Combining the characteristics of high throughput and high light use efficiency, it has laid a stable foundation for new high-precision processing technology.

Prospection

Although this research has obtained good results in the process of theoretical and experimental verification for the improvement of the precision and stability of the holographic laser processing, it still needs further exploration and research in many details.

The mechanism of optimization in the system is based on the terminal information, that is, the distribution of light intensity. The system imperfection analysis and optimization are performed to obtain the optimal CGH for holographic laser processing, and this process is performed synchronously with the laser processing. It can monitor the performance of the processing system in real time and respond quickly to the influence of various environmental factors. In this process, the source of the static and dynamic imperfection

factors of the system has not been explored, because the feedback of terminal information has integrated the defect performance of the overall system.

The aberration compensation is also necessary. Because the in-system optimization in this paper only takes use of the intensity information of the optical reconstructions, but not the information from a workpiece and the structural changes. Therefore, we can adopt the compensation methods for 2D or 3D laser processing inside bulk transparent materials to obtain more accurate machining data and further analyze and operate it [76,77]. The aberrations, especially the spherical aberration, derived from the refractive index mismatch between different propagation media, should be considered priority. And some methods have been proposed for the compensation. For example, adjusting the tube length in the optical tweezers to obtain an opposite spherical aberration [78], calculating an distortion pattern based on the inverse optical ray tracing [44], and making a specific CGH to reduce the chromatic aberration customized for the practical applications [8].

In addition, the spatial dispersion on the Fourier plane should be discussed, for example, in our 3D optimization optical system, we calculated the dispersion of $\Delta r = 0.2\ \mu\mathrm{m}$ by using the equation (3) $\Delta r = F v \Delta\lambda M$ in chapter 1. This result has no impact on the current experiment because the value is only about 11% of the focal spot size of ~1.81 $\mu\mathrm{m}$. However, in the future experiment, if we take use a wider spectral width laser source and a higher resolution LCOS-SLM, the spatial dispersion compensation should be considered [79-81].

Moreover, further exploration in the control of light intensity distribution is needed, such as focusing control, enlargement and reduction of the spot size, specific distribution of energy, switching between the Gaussian beam and the planar beam, and extension of 3D focus coordinates, etc. In addition, the performance of system components requires further analysis, such as exploring the relationship between temperature changes and the response performance of the SLM and the CCD image sensor, the relationship between laser stability and optimal uniformity values, and the relationship between computing process and overall system operations etc. In the in-system optimization process of 2D and 3D CGH, whether the optimization of the hardware and software system can be improved to reduce the time consumption, so as to achieve seamless connection with the

actual processing requirements and provide higher reliability.

In the three-dimensional holographic glass grooving technology, whether it is possible to achieve consistent processing from the surface of the material to the inside through the quantitative research and analysis of the modification performance inside the glass material.

Furthermore, actually, we are also studying a new method for 3D focusing detection. It will be implemented with a superposition of lens term to CGHs. The method we call the holographic division multiplexing method (HDMM). And it will be used for multi-layer foci recognition and optimization only at the Fourier plane, namely, without mechanical moving axially of the imager. The key novelty in this method is multiplex two CGHs to compound modulate the laser beam for easily optimizing the multi-layer foci with a single capture. This method consists of three components: the most important HDMM module, the optics, and the imager. The HDMM module, comprises CGH calculation software and two SLMs. The CGH calculation software is used for optimizing CGH1 and calculating CGH2 respectively. The CGH1 is the target for optimization, which is displayed on the SLM1 and updated in each iteration, containing the desired multi-layer foci information. The CGH2 is a pre-designed grating for parallel modulation, which is displayed on the SLM2, modulates the light beam parallelly. The multi-layer modulated light from SLM1 is then parallelly modulated by SLM2 to a multiplexed modulated light, called HDMM. The optics are customized for multi-layer focusing, and the imager is used to obtain the light intensity profiles at the Fourier plane. By combining with the high-performance GPU, the higher-speed imager, the higher-frequency SLM, and the optimal calculation algorithm, we believe this method can be a high-speed, high-stability, high-precision, and high-practical industrial technology in the future.

References

[1] Y. Hayasaki, T. Sugimoto, A. Takita, and N. Nishida, “Variable holographic femtosecond laser processing by use of a spatial light modulator,” Appl. Phys. Lett. 87, 031101 (2005).

[2] N. Sanner, N. Huot, E. Audouard, C. Larat, J. P. Huignard, and B. Loiseaux, “Programmable focal spot shaping of amplified femtosecond laser pulses,” Opt. Lett. 30, 1479 (2005).

[3] J. Houzet, N. Faure, M. Larochette, A.-C. Brulez, S. Benayoun, and C. Mauclair, “Ultrafast laser spatial beam shaping based on Zernike polynomials for surface processing,” Opt. Express 24, 6542 (2016).

[4] S. Hasegawa, Y. Hayasaki, and N. Nishida, “Holographic femtosecond laser processing with multiplexed phase Fresnel lenses,” Opt. Lett. 31, 1705-1707 (2006).

[5] N. J. Jenness, K. D. Wulff, Matthew S. Johannes, Miles J. Padgett, Daniel G. Cole, and Robert L. Clark, “Three-dimensional parallel holographic micropatterning using a spatial light modulator”, Opt. Express. 16 (20). 15942-15948(2008).

[6] M. Yamaji, H. Kawashima, J. Suzuki, and S. Tanaka, “Three-dimensional micromachining inside a transparent material by single pulse femtosecond laser through a hologram,” Appl. Phys. Lett. 93, 041116 (2008).

[7] M. Sakakura, T. Sawano, Y. Shimotsuma, K. Miura and K. Hirao, “Fabrication of three-dimensional 1 × 4 splitter waveguides inside a glass substrate with spatially

phase modulated laser beam," Opt. Express 18, 12136-12143 (2010).

[8] A. Jesacher and M. J. Booth, "Parallel direct laser writing in three dimensions with spatially dependent aberration correction," Opt. Express 18, 21090-21099 (2010).

[9] "Industrial Laser Systems Market Ends 2020 with a 2% Decrease Demand in Asia Grows in Spite of COVID," Optech Consulting (2021).

[10] B. Gefvert, C. Holton, A. Nogee, J. Hecht, "Annual Laser Market Review & Forecast 2020: Laser markets navigate turbulent times," Laser Focus World (2020).

[11] B.N. Chicbkov, C. Momma, S. Nolte, F. von Alvensleben, A. Tiinnermann, "Femtosecond picosecond and nanosecond laser ablation of solids," Appl. Phys. A 63, 109-115 (1996).

[12] K. Sugioka, and Y. Cheng, "Femtosecond laser three-dimensional micro- and nanofabrication," Appl. Phys. Review. 1, 041303 (2014).

[13] A. Fernandez, T. Fuji, A. Poppe, A. Fürbach, F. Krausz, and A. Apolonski, "Chirped-pulse oscillators: a route to high-power femtosecond pulses without external amplification," Opt. Lett. 29(12), 1366 (2004).

[14] D. Du, X. Liu, G. Korn, J. Squier, G. Mourou, "Laser-induced breakdown by impact ionization in SiO2 with pulse widths from 7 ns to 150 fs," Appl. Phys. Lett. 64, 3071 (1994).

[15] A.C. Tien, S. Backus, H. Kapteyn, M. Murnane, G. Mourou, "Short-Pulse Laser Damage in Transparent Materials as a Function of Pulse Duration," Phys. Rev. Lett. 82, 3883 (1999).

[16] Z. Kuang, W. Perrie, J. Leach, M. Sharp, S. P. Edwardson, M. Padgett, G. Dearden,

K. G. Watkins, “High throughput diffractive multi-beam femtosecond laser processing using a spatial light modulator,” Appl. Surf. Sci. 255, 2284-2289 (2008).

[17] G. Cerullo, R. Osellame, S. Taccheo, M. Marangoni, D. Polli, R. Ramponi, P. Laporta, and S. D. Silvestri, “Femtosecond micromachining of symmetric waveguides at 1.5 mm by astigmatic beam focusing,” Opt. Lett. 27, 1938 (2002).

[18] Y. Cheng, K. Sugioka, K. Midorikawa, M. Masuda, K. Toyoda, M. Kawachi, and K. Shihoyama, “Control of the cross-sectional shape of a hollow microchannel embedded in photostructurable glass by use of a femtosecond laser,” Opt. Lett. 28, 55 (2003).

[19] M. Ams, G. D. Marshall, D. J. Spence, and M. J. Withford, “Slit beam shaping method for femtosecond laser direct-write fabrication of symmetric waveguides in bulk glasses,” Opt. Express. 13, 5676 (2005).

[20] M. Merano, G. Boyer, A. Trisorio, G. Chériaux, and G. Mourou, “Superresolved femtosecond laser ablation,” Opt. Lett. 32, 2239 (2007).

[21] K. Kawamura, T. Ogawa, N. Sarukura, M. Hirano, H. Hosono, “Fabrication of surface relief gratings on transparent dielectric materials by two-beam holographic method using infrared femtosecond laser pulses,” Appl. Phys. B Lasers. Opt. 71, 119 (2000).

[22] L. Wu, Y. Zhong, C. Chan, and K. Wong, “Fabrication of large area two- and three-dimensional polymer photonic crystals using single refracting prism holographic lithography,” Appl. Phys. Lett. 86, 241102 (2005).

[23] M. Lei, B. Yao, and R. A. Rupp, “Structuring by multi-beam interference using

symmetric pyramids," Opt. Express. 14, 5803 (2006).

[24] T. M. Bloomstein, M. F. Marchant, S. Deneault, D. E. Hardy, and M. Rothschild, "22-nm immersion interference lithography," Opt. Express. 14, 6434 (2006).

[25] S. Matsuo, S. Juodkazis, and H. Misawa, "Femtosecond laser microfabrication of periodic structures using a microlens array," Appl. Phys. A Mate. Sci Process. 80, 683 (2005).

[26] J. Kato, N. Takeyasu, and Y. Adachi, "Multiple-spot parallel processing for laser micro/nano-fabrication," Appl. Phys. Lett. 86, 044 (2005).

[27] A. Shishido, I. B. Diviliansky, I. C. Khoo, and T. S. Mayer, "Direct fabrication of two-dimensional titania arrays using interference photolithography," Appl. Phys. Lett. 79, 3332 (2001).

[28] J. K. Wiele and P. Simon, "Fabrication of periodic nanostructures by phase-controlled multiple-beam interference," Appl. Phys. Lett. 83, 4707 (2003).

[29] J. Amako, K. Nagasaka, and N. Kazuhiro, "Chromatic-distortion compensation in splitting and focusing of femtosecond pulses by use of a pair of diffractive optical elements," Opt. Lett. 27, 969 (2002).

[30] G. Vega, J. Lancis, J. Caraquitena, V. T. Company, and P. Andrés, "High spatiotemporal resolution in multifocal processing with femtosecond laser pulses," Opt. Lett. 31, 2631 (2006).

[31] Y. Hayasaki, H. Yamamoto, N. Nishida, "Optical dependence of spatial frequency of formed patterns on focusing deviation in nonlinear optical ring resonator," Opt. Commun. 151, 263 (1998).

[32] Y. Hayasaki, H. Yamamoto, N. Nishida, “Self-scanning of isolated spots in a nonlinear optical system with two-dimensional feedback,” J. Opt. Soc. Am. B. 17, 1211 (2000).

[33] A. A. Maznev, T. F. Crimmins, and K. A. Nelson, “How to make femtosecond pulses overlap,” Opt. Lett. 23, 1378 (1998).

[34] H. Sun, Y. Xu, S. Juodkazis, K. Sun, M. Watanabe, S. Matsuo, H. Misawa, and J. Nishii, “Arbitrary lattice photonic crystals created by multiphoton microfabrication,” Opt. Lett. 26, 325 (2001).

[35] T. Kondo, S. Matsuo, S. Juodkazis, and H. Misawa, “Femtosecond laser interference technique with diffractive beam splitter for fabrication of three-dimensional photonic crystals,” Appl. Phys. Lett. 79, 725 (2001).

[36] Y. Nakata, T. Okada, M. Maeda, “Fabrication of dot matrix, comb, and nanowire structures using laser ablation by interfered femtosecond laser beams,” Appl. Phys. Lett. 81, 4239 (2002).

[37] Li Y, Watanabe W, Yamada K, Shinagawa T, Itoh K, Nishii J, Jiang Y, “Holographic fabrication of multiple layers of grating inside soda-lime glass with femtosecond laser pulses,” Appl. Phys. Lett. 80, 1508 (2002).

[38] K. Venkatakrishnan, N.R. Sivakumar, C.W. Hee, B. Tan, W.L. Liang, G.K. Gan, “Direct fabrication of surface-relief grating by interferometric technique using femtosecond laser,” Appl. Phys. A. Mater. Sci. Process. 77, 959 (2003).

[39] Kuroiwa Y, Takeshima N, Narita Y, Tanaka S, Hirao K, “Arbitrary micropatterning method in femtosecond laser microprocessing using diffractive optical elements,”

Opt. Express. 12, 1908 (2004).

[40] Y. Hayasaki, M. Nishitani, H. Takahashi, H. Yamamoto, A. Takita, D. Suzuki, S. Hasegawa, “Experimental investigation of the closest parallel pulses in holographic femtosecond laser processing,” Appl. Phys. A Mater. Sci. Process. 107, 357 (2012).

[41] S. Hasegawa, Y. Hayasaki, “Holographic femtosecond laser processing with multiplexed phase Fresnel lenses displayed on the liquid crystal spatial light modulator,” Opt. Rev. 14, 208 (2007).

[42] H. Takahashi, S. Hasegawa, and Y. Hayasaki, “Holographic femtosecond laser processing using optimal-rotation-angle method with compensation of spatial frequency response of liquid crystal spatial light modulator,” Appl. Opt. 46, 5917-5923 (2007).

[43] K. Chaen, H. Takahashi, S. Hasegawa, and Y. Hayasaki, “Display method with compensation of the spatial frequency response of a liquid crystal spatial light modulator for holographic femtosecond laser processing,” Opt. Commun. 280, 165-172 (2007).

[44] H. Itoh, N. Matsumoto, and T. Inoue, "Spherical aberration correction suitable for a wavefront controller," Opt. Express 17, 14367-14373 (2009).

[45] F. Zernike, “Phase contrast, a new method for the microscopic observation of transparent objects,” Physica. 9, 686 (1942).

[46] D. Gabor, “A New Microscopic Principle,” Nature. 161, 777 (1948).

[47] T. H. Maiman, “Stimulated optical radiation in ruby,” Nature.187, 493 (1960).

[48] E. N. Leith and J. Upatnieks, “Wavefront Reconstruction with Continuous-Tone

Objects," J. Opt. Soc. Am. 53, 1377 (1963).

[49] A. Kozma and D. L. Kelly, "Spatial Filtering for Detection of Signals Submerged in Noise," Appl. Opt. 4, 387 (1965).

[50] A. W. Lohmann, D. P. Paris, "Binary Fraunhofer Holograms, Generated by Computer," Appl. Opt. 6, 1739 (1967).

[51] Denisyuk, Y. N, "On the Reflection of Optical Properties of an Object in a Wave Field of Light Scattered by it," Doklady Akademi Nauk SSSR, 144, 1275 (1962).

[52] W. H. Lee, "Sampled Fourier Transform Hologram Generated by Computer," Appl. Opt. 9, 639 (1970).

[53] W. H. Lee, "Binary synthetic holograms," Appl. Opt. 13, 1677 (1974).

[54] J. P. Waters, "Holographic image synthesis utilizing theoretical methods," Appl. Phys. Lett. 9, 405 (1966).

[55] L. B. Lesem; P. M. Hirsch; J. A. Jordan, "The Kinoform: A New Wavefront Reconstruction Device," IBM J. Res. Develop. 13, 150 (1969).

[56] H. Dammann, K. Gortler, "High-efficiency in-line multiple imaging by means of multiple phase holograms," Opt. Commun. 3, 312 (1971).

[57] G. Tricoles, "Computer generated holograms: an historical review," Appl. Opt. 26, 4351 (1987).

[58] R. W. Gerchberg, W. O. Saxton, "A practical algorithm for the determination of the phase from image and diffraction plane pictures", Optik. 35, 237 (1972).

[59] M. A. Seldowitz, J. P. Allebach, and D. W. Sweeney, "Synthesis of digital holograms by direct binary search," Appl. Opt. 26, 2788 (1987).

[60] M. S. Kim, M. R. Feldman, and C. C. Guest, “Optimum encoding of binary phase-only filters with a simulated annealing algorithm,” Opt. Lett. 14, 545 (1989).

[61] M. W. Farn, "New iterative algorithm for the design of phase-only gratings," Proc. Soc. Photo-Opt. Instrum. Eng. 1555, 34 (1991).

[62] M. Gale, M. Rossi, H. SchUtz, P. Ehbets, H. P. Herzig, and D. Prongue, "Continous-relief diffractive optical elements for two-dimensional array generation," Appl. Opt. 32, 2526 (1993).

[63] J. Bengtsson, “Kinoform design with an optimal-rotation-angle method,” Appl. Opt. 33, 6879 (1994).

[64] N. Yoshikawa, M. Itoh, and T. Yatagai, “Quantized phase optimization of two-dimensional Fourier kinoforms by a genetic algorithm,” Opt. Lett. 20, 752 (1995).

[65] J. Liesener, M. Reicherter, T. Haist, H.J. Tiziani, “Muti-functional optical tweezers using computer-generated holograms,” Opt. Commun. 185, 77 (2000).

[66] S. Hasegawa, and Y. Hayasaki, “Adaptive optimization of a hologram in holographic femtosecond laser processing system,” Opt. Lett. 34, 22 (2009).

[67] S. Hasegawa, and Y. Hayasaki, “A Second-harmonic optimization of computer-generated hologram,” Opt. Lett. 36, 2943 (2011).

[68] H. Zhang, S. Hasegawa, H. Takahashi, H. Toyoda and Y. Hayasaki, “In-system optimization of a hologram for high-stability parallel laser processing,” Opt. Lett. 45, 3344-3347 (2020).

[69] R. Di Leonardo, F. Ianni, and G. Ruocco, “Computer generation of optimal holograms for optical trap arrays,” Opt. Express. 15, 1913 (2007).

[70] J. W. Cooley and J. W. Tukey, “An algorithm for the machine calculation of complex Fourier series,” Math. Comput. 19, 297 (1965).

[71] H. Zhang, S. Hasegawa, H. Toyoda and Y. Hayasaki, “Three-dimensional holographic parallel focusing with feedback conrol for femtosecond laser processing,” Optics and Lasers in Engineering, Vol. 151, Issue 106884, ISSN 0143-8166 (2022).

[72] J. W. Goodman, "Introduction to Fourier Optics", 2nd ed., McGraw-Hill, New York, (1996).

[73] L. Yu, M. K. Kim, “Wavelength-scanning digital interference holography for tomographic three-dimensional imaging by use of the angular spectrum method,” Opt. Lett. 30, 2092-2094 (2005).

[74] R. Di Leonardo, F. Ianni, and G. Ruocco, “Computer generation of optimal holograms for optical trap arrays,” Opt. Express 15, 1913-1922 (2007).

[75] Y. Zhao, L. Cao, H. Zhang, D. Kong, and G. Jin, “Accurate calculation of computer-generated holograms using angular spectrum layer-oriented method,” Opt. Express. 23, 25440-25449 (2015).

[76] C. Mauclair, A. Mermillod-Blondin, N. Huot, E. Audouard, and R. Stoian, “Ultrafast laser writing of homogeneous longitudinal waveguides in glasses using dynamic wavefront correction,” Opt. Express 16, 5481-8492 (2008).

[77] B. Sun, P. S. Salter, C. Roider, A. Jesacher, J. Strauss, J. Heberle, M. Schmidt, and M. J. Booth, “Four-dimensional light shaping: manipulating ultrafast spatiotemporal foci in space and time,” Light Sci. Appl. 7, 17117 (2018).

[78] S. NaderS. Reihani, Mohammad A. Charsooghi, Hamid R. Khalesifard, and Ramin Golestanian, “Efficient in- depth trapping with an oil-immersion objective lens,” Opt. Lett. 31, 766-768 (2006).

[79] M. Kempe, U. Stamm, B. Wilhelmi, and W. Rudolph, “Spatial and temporal transformation of femtosecond laser pulses by lenses and lens systems,” J. Opt. Soc. Am. B. 9, 1158-1165 (1992).

[80] G. Vega, E. Tajahuerce, M. Fernández-Alonso, V. Climent, J. Lancis, J. Caraquitena, and P. Andrés, “Dispersion-compensated beam-splitting of femtosecond light pulses: wave optics analysis,” Opt. Express. 15, 278 (2007).

[81] S. Hasegawa, and Y. Hayasaki, “Nonlinear sharpening of holographically processed submicrostructures,” Appl. Phys. A. 111, 929-934 (2013).

Published resume

Academic papers

[1] In-system optimization of a hologram for high-stability parallel laser processing
Honghao Zhang, Satoshi Hasegawa, Hidetomo Takahashi, Haruyoshi Toyoda and Yoshio Hayasaki
Optics Letters, Vol. 45, Issue 12, pp. 3344-3347 (2020)

[2] Three-dimensional holographic parallel focusing with feedback control for femtosecond laser processing
Honghao Zhang, Satoshi Hasegawa, Haruyoshi Toyoda and Yoshio Hayasaki
Optics and Lasers in Engineering, Vol. 151, 106884 (2022)

International conference presentations

[1] Honghao Zhang, Satoshi Hasegawa and Yoshio Hayasaki, "In-system optimization of hologram for holographic femtosecond laser processing," SPIE/COS, Photonics Asia, 111880M, Hangzhou, China (November 2019).

[2] Honghao Zhang, Satoshi Hasegawa, Hidetomo Takahashi, Haruyoshi Toyoda and Yoshio Hayasaki, "In-system optimization of hologram for high-stability parallel laser processing," OSA Frontiers in Optics/Laser Science, virtual conference, FM2A.4, America (September 2020).

[3] Honghao Zhang, Satoshi Hasegawa, Haruyoshi Toyoda and Yoshio Hayasaki, "In-system optimization of a computer-generated hologram for three-dimensional reconstruction," OSJ-OSA-OSK Joint Symposia on Optics, virtual conference, 14pEJ4, Japan (October 2020).

[4] Honghao Zhang, Satoshi Hasegawa, Haruyoshi Toyoda and Yoshio Hayasaki, "Hologram optimized in holographic laser processing system," Optical Technology and Measurement for Industrial Applications, virtual conference, OPTM-2-04, Japan (April 2021).

[5] Honghao Zhang, Satoshi Hasegawa, Haruyoshi Toyoda and Yoshio Hayasaki, "Three-dimensional micro-fabrication with optimized holographic reconstructions," 22nd International symposium on Laser Precision Microfabrication, virtual conference, LPM-182, Japan (June 2021).

[6] Fumiya Ishita, Honghao Zhang, Satoshi Hasegawa, Yoshio Hayasaki, "Fabrication of Diffraction Grating using Holographic Parallel Focused Beams with Long Focal Depth," 22nd International

symposium on Laser Precision Microfabrication, virtual conference, LPM-165, Japan (June 2021).

[7] Honghao Zhang, Satoshi Hasegawa, Haruyoshi Toyoda, and Yoshio Hayasaki, “Three-dimensional holographic laser reconstruction and processing with optimized computer-generated hologram,” SPIE/COS, Photonics Asia, Invited 118980I, on demand, Nantong, Jiangsu, China (October 2021).

Domestic conference presentations

[1] 張　弘昊，千葉 泰誠，熊谷 幸汰，早崎芳夫, “フェムト秒レーザー誘起マイクロバブルの自然消滅による描きかえ可能なボリュームディスプレイ,” Optics & Photonics Japan 2018,ポスター　31aP13, 東京 (2018 年 11 月).

[2] 張　弘昊，長谷川 智士，高橋　秀知，豊田 晴義，早崎 芳夫, “計算機ホログラムのインシステム最適化,” Optics & Photonics Japan 2019, 5pE3, 大阪 (2019 年 12 月).

[3] 張　弘昊，長谷川 智士，早崎 芳夫, “In-system optimization of a computer-generated hologram for holographic femtosecond laser processing,” レーザー学会学術講演会第 40 回年次大会, H05-22a-XII-05, 仙台 (2020 年 1 月).

[4] 張　弘昊，長谷川 智士，早崎 芳夫, “Holographic laser processing using in-system optimization of hologram,” International workshop on optics, biology, and related technologies 2021 (IWOB2021), 宇都宮大学 ONLINE　(2021 年 2 月).

[5] 張　弘昊，長谷川 智士，豊田 晴義，早崎 芳夫, “システム内最適化されたホログラムを用いた単一ショットで３次元レーザー加工,” 応用物理春季学術講演会第 68 回, 18p-Z32-4, online (2021 年 3 月).

[6] 石田典也，張　弘昊，長谷川智士，早崎芳夫, "ホログラフィックフェムト秒レーザー加工を用いた体積型回折格子の作製,” 応用物理秋季学術講演会第 82 回, 10a-N321-9, online (2021 年 9 月).

[7] 石田典也，張　弘昊，長谷川智士，早崎芳夫, "ホログラフィックフェムト秒レーザー加工を用いた並列長焦点ビームによる体積型回折格子の作製,” Optics & Photonics Japan 2021, 29pB2, online (2021 年 10 月).

Awards

[1] **張　弘昊**, 長谷川 智士，豊田 晴義，早崎 芳夫, “In-system optimization of a computer-generated hologram for three-dimensional reconstruction,” OSJ-OSA-OSK Joint Symposia on Optics, Best Student Paper Prize, 14pEJ4, Japan (2020. 11.17).

[2] **張　弘昊**, 令和２年度宇都宮大学学生表彰, (2021. 3. 16).